THESIS FOR THE DEGREE OF DOCTOR OF PHILOSOPHY

Integration of Surface Acoustic Wave and Microfluidic Technologies for Liquid-Phase Sensing Applications

KIRYL KUSTANOVICH

Department of Chemistry and Chemical Engineering

CHALMERS UNIVERSITY OF TECHNOLOGY

Gothenburg, Sweden 2019

Integration of Surface Acoustic Wave and Microfluidic Technologies for Liquid-Phase Sensing Applications

KIRYL KUSTANOVICH
ISBN 978-91-7905-116-7

© KIRYL KUSTANOVICH, 2019

Doktorsavhandlingar vid Chalmers tekniska högskola
Ny serie nr 4583
ISSN # 0346-718X

Department of Chemistry and Chemical Engineering
Chalmers University of Technology
SE-412 96 Gothenburg
Sweden
Telephone + 46 (0)31-772 1000

Cover:

1) Photograph of the fabricated surface acoustic resonance (SAR) in-liquid sensor; 2) 3D representation of the SAR sensor; 3) optical microscope image of the SAR sensor; 4) FEM model of the sensor loaded with water; 5) fluorescence imaging of multilamellar vesicles deposited on the sensor surface.

Printed by Chalmers Reproservice
Gothenburg, Sweden 2019

Integration of Surface Acoustic Wave and Microfluidic Technologies for Liquid-Phase Sensing Applications

KIRYL KUSTANOVICH
Department of Chemistry and Chemical Engineering
Chalmers University of Technology

Abstract

This thesis discusses a new concept for construction of a novel SAW in-liquid sensor employing surface acoustic wave resonance (SAR) in a one-port configuration. In this concept, the reflective gratings of a one-port SAW resonator are employed as mass loading-sensing elements, while the SAW transducer is protected from the measurement environment, reducing power losses significantly.

Microfluidic technologies have developed during the last decades into versatile platforms for miniaturized analytical devices. The devices are small, low cost, capable of multi-step automation resulting in fast turnaround, and allow reducing the amount of reagent and sample consumption, while maintaining a precise control over the environment. In this context, small, cheap and efficient sensors capable of in-liquid operation within microfluidic devices are in a great demand. The introduction of acoustic wave technology onto lab-on-a-chip platforms provides sensing capability that meets these criteria, and allows for an extended set of functions to be implemented, e.g., fast fluidic actuation, contact-free particle manipulation, sorting, and others.

A resonant SAW sensor topology embedded in a polydimethylsiloxane (PDMS) microfluidic analyte delivery system was fabricated and characterized. Designs with the best performance were identified, and initial measurements in a liquid environment are discussed. In comparison to a delay-line topology, the proposed one-port resonant configuration features improved sensitivity, while offering better electrical performance and smaller size, which allows for wafer-scale fabrication and facilitates integration. Following optimization, sensing performance was evaluated by means of different assays, and multiparametric sensing was demonstrated by sharing of sensor components for simultaneous SAR sensing and electrochemical impedance spectroscopy in different frequency bands.

This technological advancement may open pathways to new analytical instrumentation. The small sensor footprint, low energy consumption, and simple two-wire readout facilitate the integration in hand-held “lab on a chip” assay devices, the construction of sensing arrays for parallel sample processing, and the implementation of wireless data transfer schemes.

Keywords: ***Surface Acoustic Wave****;* ***Resonator; Sensor; Microfluidics; SH-SAW; Impedance Spectroscopy; IDE; PDMS;*** ***$LiNbO_3$***

List of Publications

Appended papers

This thesis is based on the work presented in the following papers:

I. **K. Kustanovich**, V. Yantchev and A. Jesorka, "*Design and characterization of surface acoustic wave resonance (SAR) system for in-liquid sensing*," 2017 Joint Conference of the European Frequency and Time Forum and IEEE International Frequency Control Symposium (EFTF/IFCS), Besancon, 2017, pp. 652-655.
doi: 10.1109/FCS.2017.8088992

II. **K. Kustanovich**, V. Yantchev, V. Kirejev, GDM Jeffries, T. Lobovkina and A. Jesorka, "*A high-performance lab-on-a-chip liquid sensor employing surface acoustic wave resonance*," 2017 Journal of Micromechanics and Microengineering, Volume 27, Number 11, pp. 114002.
doi: 10.1088/1361-6439/aa8f21

III. **K. Kustanovich**, V. Yantchev A. Olivefors, B. Ali Doosti, T. Lobovkina and A. Jesorka, "*A high-performance lab-on-a-chip liquid sensor employing surface acoustic wave resonance: part II*," 2019 Journal of Micromechanics and Microengineering, Volume 29, Number 2, pp. 024001.
doi: 10.1088/1361-6439/aaf411

IV. **K. Kustanovich**, V. Yantchev, B. Ali Doosti, I. Gözen and A. Jesorka, "*A Microfluidics-integrated Impedance/Surface Acoustic Resonance Tandem Sensor*," (*submitted manuscript*)

V. A. A. Kim, **K. Kustanovich**, D. Baratian, A. Ainla, M. Shaali, G. D. M. Jeffries, and A. Jesorka, "*SU-8 free-standing microfluidic probes*," 2017 Biomicrofluidics, Volume 11, Number 1, pp. 014112.
doi: 10.1063/1.4975026

Other Papers and Publications

The following papers and publications are not appended to the thesis, either due to contents overlapping of that of appended papers, or due to contents not related to the thesis.

[a] – Pedersen, R.H., **K. Kustanovich**, and N. Gadegaard, “*Single-step 3D nanolithography using plasma polymerized hexane films”,* Microelectronic Engineering, 2012. 98: p. 167-170.

[b] – Gozen, I., et al., “*Thermal Migration of Molecular Lipid Films as Contactless Fabrication Strategy for Lipid Nanotube Networks” (vol 13, pg 3822, 2013).* Lab on a Chip, 2013. 13(24): p. 4892-4892.

[c] – G. Jeffries, A. Kim, **K. Kustanovich**, A. Jesorka, *“Open Volume Microlfuidc Probes”*, Compendium of In Vivo Monitoring in Real-Time Molecular Neuroscience: Volume 2: Microdialysis and Sensing of Neural Tissues, 2017, p. 291

[d] – Sepehri, S., et al., *“Volume-amplified magnetic bioassay integrated with microfluidic sample handling and high-TC SQUID magnetic readout”*, APL Bioengineering, 2018. 2(1): 016102.

[e] – Jõemetsa, S., et al., *"Molecular lipid films on microengineering materials",* (*submitted manuscript*)

[f] – Orwick Rydmark, M., et al., *"Styrene maleic acid polymer induces pores in biomembranes",* (*submitted manuscript*)

[g] – Ali Doosti, B., et al., *"Formation of artificial intracellular vesicles",* (*manuscript in preparation*)

[h] – Jesorka, A., **Kustanovich, K**., Yantchev, V., *"A surface acoustic wave resonant sensor",* Patent SE 1750678-3

Contribution Report

Paper I

Design and Characterization of Surface Acoustic Wave Resonance (SAR) System for In-liquid Sensing

I have contributed by designing various IDT and reflector topologies that can effectively suppress spurious modes. Test chips were fabricated and characterized. Experimental validation of the sensor performance was conducted in-liquid. Manuscript writing.

Paper II

A High-performance Lab-on-a-chip Liquid Sensor Employing Surface Acoustic Wave Resonance

I have contributed by creating the design of the device, its fabrication and characterization. A new fabrication process was developed and optimized. Experimental validation of the sensor performance in-liquid and with supported lipid bilayers was performed. Manuscript writing.

Paper III

A High-performance Lab-on-a-chip Liquid Sensor Employing Surface Acoustic Wave Resonance: Part II

I have contributed by creating the improved design of the device, its fabrication and characterization. I have also developed a software that controls, logs and analyses data obtained from the VNA. Further experimental validation of the sensor performance in-liquid and with supported lipid bilayers was performed. Manuscript writing.

Paper IV

A Microfluidics-integrated Impedance/Surface Acoustic Resonance Tandem Sensor

I have contributed by creating the design of the device, its fabrication and characterization. Experimental validation and data analysis. Manuscript writing.

Paper V

SU-8 free-standing microfluidic probes

I have contributed by creating the design of the microdialysis probes, their fabrication and characterization. Improving and investigating limits of the fabrication process, common failure mechanisms identification and analysis. Manuscript writing.

Contents

Abstract I

List of Publications III

Contribution Report VII

1 Introduction.....1

2 Background.....3

2.1 Elastic Waves in Solids 4

2.2 Plane Waves in Piezoelectric Solids.....5

2.3 Surface Acosutic Waves 8

2.4 Saw Devices. 11

2.4.1 Excitation and Detection of SAWs 11

2.4.2 SAW Resonators 13

2.4.3 SAW Resonator Characterization..... 15

2.5 Microfluidics..... 26

2.5.1 Fluid Flow Inside a Microfluidic Channel 26

2.5.2 Mass Transport and Diffusion..... 28

3 Analytical Techniques.....31

3.1 Sensors 31

3.1.1 Electro-Acoustic Sensors..... 32

3.1.2 Surface Acoustic Wave Sensors 35

3.1.3 Perfomance Characterisitics of the Surface Acosutic Wave Resonator as a Sensor. 37

3.2 Electrical and Electrochemical Methods 46

3.2.1 Equivalent Circuit Modelling..... 49

3.3 Optical Detection Methods 52

3.3.1 Fluorescence Microscopy 53

4 Surface Acoustic Wave Resonance (SAR) Liquid-Phase Sensor 55

4.1 The SAR Concept 55

4.2 Resonator Optimization 60

4.3 Sensor Characterization 68

4.4 Biochemical Sensing 70

4.4.1 Sensing of SLB Transformations.. 73

4.5 Integration of SAR Sensor with Electrochemical Impedance Spectroscopy...........................75

4.5.1 Multiparametric Sensing of SLB Transformations 77

5 Device Fabrication...83

5.1 Pattern Transfer, Thin Film Deposition, Etching and Bonding Processes 83

5.2 Lithography 87

5.3 Bonding 90

5.4 Materials 92

5.5 Fabrication of SAR-integrated microfluidic devices 95

5.6 Interfacing Considerations 98

6 Conclusions and Future Outlook...103

7 Summary of Appended Papers...107

Acknowledgment...109

Bibliography..111

1 INTRODUCTION

In recent years, *surface acoustic wave* (SAW) technologies have been gaining more and more attention in the microfluidics community [1]. The majority of SAW devices are currently used in the telecommunication industry for *radio frequency* (RF) filtering and signal processing applications [2]. At the moment, the field of surface acoustic wave devices enters its third stage of development. The first generation comprised quartz-based SAW devices [3], and the second progressed to high-coupling leaky SAWs on $LiNbO_3$ and $LiTaO_3$ [4, 5]. The latest development, which is now being commercialized, is based upon high performance devices fabricated on *hetero-acoustic layer* (HAL) substrates [6-12]. These substrates allow for a greater confinement of the SH-SAWs near the surface, for robust temperature compensation, and provide the high electromechanical couplings necessary for sensors with large dynamic range. The new SAW substrates have strong potential for commercialization, enabled by the fabrication technologies established by the RF filter industry [13].

For the past 20 years, significant efforts in the field of microfluidics-integrated sensing technology focused on the development of highly sensitive, label-free, real-time devices based on the thin-film electroacoustic technology [14], with only limited practical success. A wide range of thin film piezoelectric transducers has been developed, studied, and their potential demonstrated. However, much of the practical developments are remaining in their early stages and their true potential has yet to be demonstrated. Thickness-excited quasi-shear film bulk acoustic resonators (shear-FBARs) have shown the best performance so far [15, 16]. This is currently the only device type that has reached the stage of commercial prototypes [17, 18]. Thin-film S0-Lamb waves and their equivalent extensional plate modes show promise too [19-21], since they also rely on the technology originally developed for commercial RF filter manufacturing. However, practical considerations comprising process uniformity, device fragility, and strong local pressure sensitivity, are limiting these approaches.

Recent research has already demonstrated that SAW technology provides an effective means for controlling, sensing and actuating particles and fluids in lab-on-a-chip devices [1, 22-25]. The advantages of SAW-based microfluidic devices are their simplicity, compactness, low cost, high biocompatibility due to the contact-free manipulation and sensing, versatility of functionalities coupled with convenient on-chip integration, ability to be mass produced, and energy efficiency. Thus, this platform concept has generated increasing attention, and much effort has been put forward to bring the technology to a commercial state.

Current topics of interest in this area are integration (planar technology vs. 3D channels, open volume [26] and droplet technologies [27]), unconventional materials in microfluidics, fabrication and process compatibility, spurious responses and damping of the devices, arising from the liquid environment [28], as well as from the microfluidic chip

geometries and materials [29]. Furthermore, the development of robust sensing and suitable signal processing approaches, and the identification and implementation of suitable assays, are important.

The aim of the work presented in this thesis was to construct a high-performance one-port SAW sensor for in-liquid operation, utilizing state-of-the-art resonator technology developed for the RF filter industry. Main subjects of the research work were design, modeling, fabrication, and testing of the new sensors, integration with microfluidic device technology, and additional sensing concepts.

This thesis is divided into background sections, where the origin of surface acoustic waves is discussed, followed by the introduction of SAW device design and characterization principles. Mechanisms of sensing in selected analytical techniques are briefly described in a corresponding chapter. The concept for a new resonant one-port microfluidics-integrated sensor is then presented, supplemented with device characterization and sensing performance data. The thesis is concluded with a section on the fabrication methods.

2 BACKGROUND

First described by Lord Rayleigh in 1885 [30], a *surface acoustic wave* is a form of mechanical wave motion propagating along the surface of a solid material. The surface acoustic wave is confined near the surface, exhibiting an energy decay into the bulk of about one wavelength. This wave belongs to the family of guided acoustic modes (*Fig. 1*).

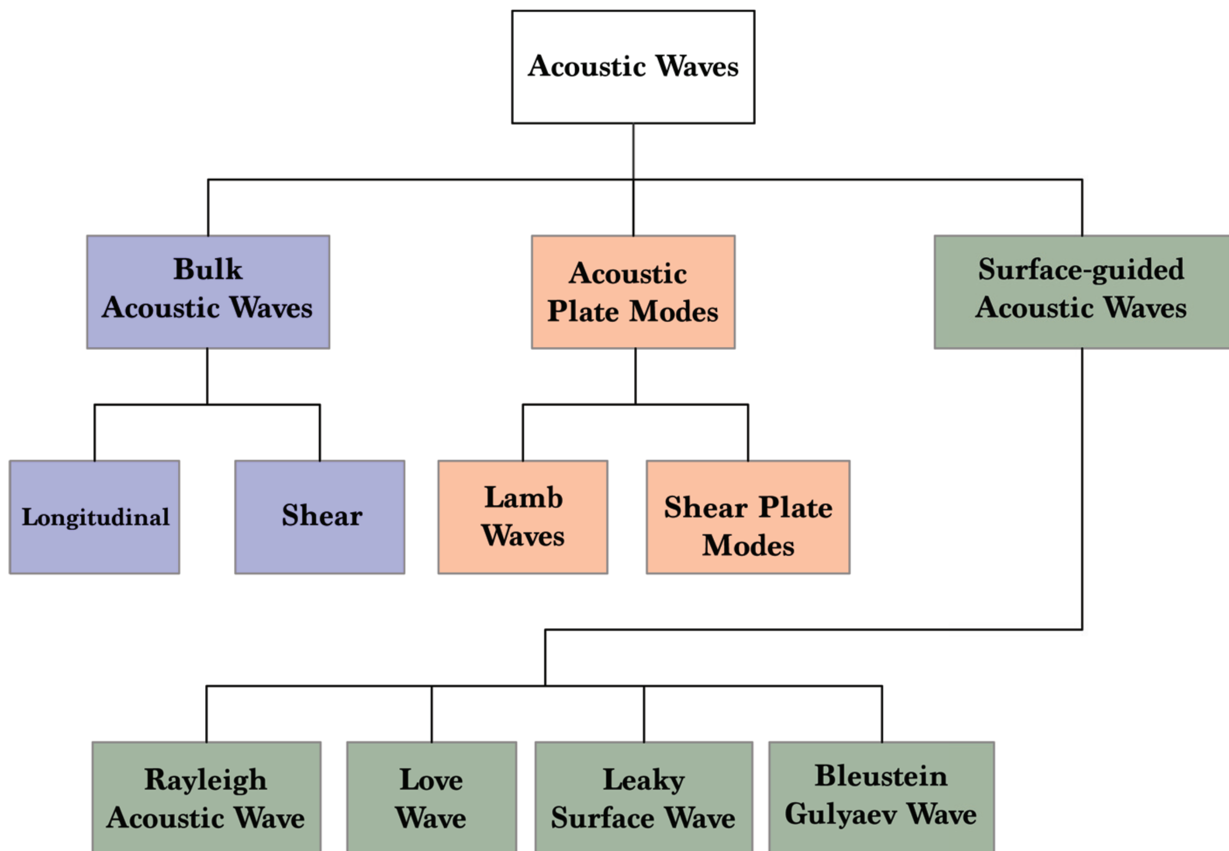

Figure 1. Classification of acoustic waves. Bulk acoustic waves are depicted in blue; plate modes are in red and surface-guided waves are colored in green.

These modes are inherently related. For example, the surface acoustic waves evolve from plate modes at the boundary of infinitely thick plates. Moreover, the majority of plate modes originate from bulk wave resonances in the dimension perpendicular to the plate surface.

2.1 ELASTIC WAVES IN SOLIDS

Bulk acoustic waves (**BAW**s) are elastic waves that propagate in solids. They are generally categorized into two groups: *longitudinal waves* (*L-type* or pressure waves), and *transverse waves* (*S-type* or shear waves) [31]. Due to the differences in stiffness constants of the material, which depend on its crystal axis orientation, these waves have different *phase velocities*. The displacement direction of longitudinal and shear waves, or *polarization, implies that* the *longitudinal wave* is parallel to the propagation direction, while the *shear wave* is perpendicular to it.

While propagating, elastic waves suffer attenuation of their amplitude. There are three main mechanisms that cause this effect [32]:

1. *Losses due to the scattering of the wave propagating through inhomogeneous media* (temperature independent; dominant for polycrystalline solids (AlN, ZnO thin films));
2. *Losses due to the scattering of the wave through thermal lattice vibrations* (temperature dependent);
3. *Temperature variation within the solid due to the change in its volume compensated by an energy transportation through thermal diffusion to neutralize the difference* (longitudinal waves only).

For each specified propagation direction, three independent acoustic waves exist. For most propagation directions in anisotropic solids, these waves do not exist in their pure form, but appear in a more general form as a *quasi-longitudinal* and two *quasi-shear waves*. In general, quasi-longitudinal waves have a higher velocity than any shear wave, while its polarization is predominantly oriented along the wave vector. The quasi-shear waves exhibit polarizations orthogonal to the *quasi-longitudinal* polarization. The quasi-shear waves are further classified as *fast-shear* and *slow-shear* waves, which have different phase velocities, and are orthogonal to each-other's polarizations.

It is common to use the polarization relative to the substrate surface for the discussion of surface acoustic waves, so that shear plane waves are referred to as *shear-vertical* (SV) when polarized perpendicularly to the surface, and *shear-horizontal* (SH) when parallel to it (*Fig. 2*) [33].

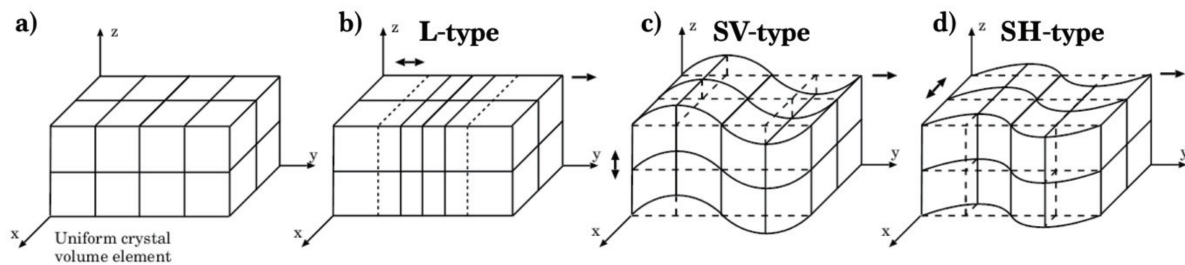

Figure 2. Various types of bulk plane acoustic waves. Black arrows indicate the direction of displacement. **a)** depicts a uniform crystal volume element; **b)** longitudinal wave; **c)** wave with shear-vertical polarization; **d)** wave with shear-horizontal polarization. [33]

2.2 Plane Waves in Piezoelectric Solids

All acoustic wave devices rely on piezoelectric materials to generate the acoustic wave [34]. Piezoelectricity is the appearance of electrical charges in a certain type of solids when they are subjected to mechanical stress. This phenomenon is a reversible process, i.e., application of an electrical field will result in a mechanical strain. Upon application of the tensile stress, dipole moments displace, resulting in a net polarization. In case of a compressive stress, the displacement causes net polarization with opposite sign. The generated polarization depends on the amplitude of applied stress, as well as its direction. In other words, piezoelectricity is a linear coupling between electricity and elasticity. It was discovered in 1880 by French physicists Pierre and Paul-Jacques Curie [35]. The term itself was introduced by Wilhelm Hankel, a German physicist, in 1881 and consists of two ancient Greek words meaning appearance of electricity resulting from pressure [36]. Only in 1921, when American physicist and electrical engineer Walter Cady introduced the first crystal oscillator based on a quartz resonator, this important class of materials got more public recognition [37].

To possess piezoelectricity, the crystallographic structure of the material must have a certain asymmetry. In other words, materials with piezoelectric effect have an anisotropic crystal structure. Dielectric, elastic, and piezoelectric properties critically depend on the direction of polarization and propagation with respect to the crystal orientation [38]. The origin of piezoelectricity can be better understood by analyzing a simplified 1D mechanical model of an ion crystal (*Fig. 3*).

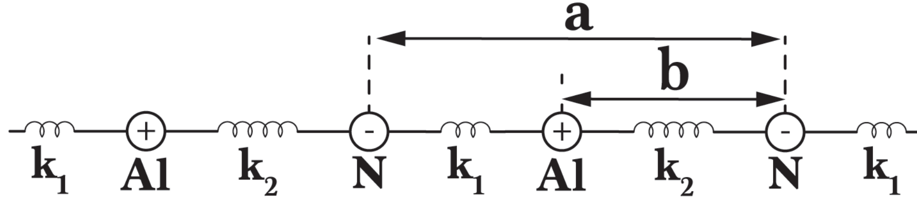

Figure 3. Schematic diagram of a simplified mechanical model of the AlN ion crystal.

Here, an AlN (aluminum nitride) crystal cell is used as an example due to its relative structural simplicity. It has a hexagonal crystal system where Al and N entities are arranged successively as planes of atoms, perpendicular to the axis of symmetry. It can be viewed as a chain of negative (N) and positive ions (Al) (—Al-N—AlN—Al-N—) connected by springs (*Fig. 3*). It is important to note that the neighboring atoms inside the chain are not symmetrical with respect to each other, i.e., there is no center of inversion. This implies that the spring on each side of an atom has a different rigidity (elastic constant). The fundamental definition of the *electric dipole moment P* shows that the piezoelectric medium has some polarization:

$$P = \frac{q}{2}(a - 2b) \neq 0 \tag{2.1}$$

where point charges *–q* and *+q* denoted as *q* are charges of two point particles separated by the distance between either charge and the center of the dipole $\frac{a-2b}{2}$. When a uniform electric field is applied, cations and anions start to move in opposite directions inducing a net deformation. When an external force is applied, the ions exhibit different displacements due to the presence of both *high*- and *low*- stiffness ionic bonds, which in turn determine a change in the net dipole moment.

In case when the crystal has a center of symmetry, no electric polarization occurs. for example, a Si crystal is cubic and covalent rather than ionic and non-centrosymmetric, thus it does not possess any piezoelectricity.

The mechanical equation of motion (*Eq. 2.2a*) represents the second Newton's law applied to dynamic solid deformation and can be described in terms of displacement u_i and electric potential Φ (*Eq.* 2.5), while the Poisson's equation for electric displacement **D** gives (*Eq.* 2.2b) [34]:

$$\rho \frac{\partial^2 u_i}{\partial t^2} = \sum_{j=1}^{3} \frac{\partial T_{ij}}{\partial X_j}, i = 1, 2, 3 \quad (2.2a)$$

$$\nabla \cdot \vec{D} = \rho_f \quad (2.2b)$$

where X is a set of coordinate axes, ρ is the density of a piezoelectric solid, and ρ_f is the free charge density. Since the material is an insulator (no free charges), $\nabla \cdot \vec{D} = 0$. The *stress tensor* $\mathbf{T_{ij}}$ depends on the *electric field* **E** (*Eq. 2.3a*) and the *piezoelectric tensor* e_{kij}, while the electric displacement $\mathbf{D_i}$ is determined by the electric field E and the *permittivity tensor* ε_{ij}^{S} (*Eq. 2.3b*):

$$T_{ij} = \sum_{k}\sum_{l} c_{ijkl}^{E} S_{kl} - \sum_{k} e_{kij} E_k \; ; \; i, j, k, l = 1, 2, 3 \quad (2.3a)$$

$$D_i = \sum_{j}\sum_{k} e_{ijk} S_{jk} + \sum_{j} \varepsilon_{ij}^{S} E_j \; ; \; i, j, k, l = 1, 2, 3 \quad (2.3b)$$

where c_{ijkl}^{E} is the *stiffness tensor* for constant electric field. S_{jkl} is the *strain tensor*:

$$S_{jkl} = \frac{1}{2}\left[\frac{\partial u_i}{\partial X_{jk}} + \frac{\partial u_{jk}}{\partial X_i}\right] \quad (2.4)$$

and the *electric field* E_{jk}:

$$E_{jk} = -\frac{\partial \Phi}{\partial X_{jk}} \quad (2.5)$$

The *Christoffel equation* is the equation of motion, Fourier-transformed over space and time, describing the plane wave solutions. It describes the propagation velocity and particle-

displacement direction (wave polarization) for each plane wave component. Green has shown in 1839 that three wave modes could exist in a general anisotropic medium [39]. In 1877, Christoffel described the variation in the velocity of wave fronts in anisotropic media with polarizations normal to each other [40]. The mathematical formula he developed allows to compute the *phase velocity* using plane wave analysis. It has a form of an eigenvalue-eigenvector problem for the phase velocity and particle-displacements, respectively:

$$\Gamma_{ij} v_n = \rho \left(\frac{\omega}{k}\right)^2 v_n \tag{2.6}$$

where ρ is the density of homogeneous medium, ω is the angular frequency. $\Gamma_{ij} = C_{ijkl} n_j n_l$ is the Christoffel matrix, while the *stiffness matrix* $[C_{ijkl}]$ gives the elastic constants. Derivative matrix $[n_j n_l]$ defines the propagation direction of a plane-wave under consideration and is a function of a wavenumber vector k. v_n is the particle-velocity vector with three mutually orthogonal solutions (one quasi-longitudinal and two quasi-shear modes). For each polarization, the phase velocity is $V'_{Wave} = \sqrt{\frac{\tilde{c}}{\rho}}$, where $\tilde{c}$ is the piezoelectrically stiffened effective elastic constant. In the particular case of omitted piezoelectricity (non-piezoelectric solids), the phase velocity is $V_{Wave} = \frac{\omega}{k} = \sqrt{\frac{c}{\rho}}$, where c is the effective elastic constant.

The *effective piezoelectric coupling* constant can be derived by using the values for stiffened and non-stiffened velocities:

$$\boldsymbol{K^2} = \frac{(V'_{Wave})^2 - (V_{Wave})^2}{(V_{Wave})^2} \tag{2.7}$$

2.3 Surface Acoustic Waves

BAWs consisting either of SV- or L-type components cannot freely propagate in parallel to the surface near it. Unlike SH waves, neither of these plane waves alone are sufficient to satisfy the zero normal stress boundary condition at the surface [41]. Thus, both L- and SV-type components close to the surface couple with each other and can result in a surface-guided eigenmode, the *Rayleigh-type* surface acoustic wave (**RSAW**). RSAWs have two components of displacement forming an ellipse within the *sagittal plane* (a plane

perpendicular to the surface, and parallel to the direction of propagation). Due to the slower phase velocity of RSAW, as compared to SV-type BAW, most of the energy is concentrated close to the surface.

On the other hand, the SH-type component can satisfy the stress-free boundary condition, and propagates along the surface and into the bulk (*surface skimming bulk waves* (SSBW)) [42]. It means that upon excitation the plane (bulk) wave with transverse polarization, perpendicular to the propagation direction and parallel to the surface, will propagate in the direction exactly parallel to the surface of an *isotropic elastic body*, while suffering from diffraction spread of the beam in to the bulk of the substrate. SH-type SAW, emanating from the SH-BAW, may exist in piezoelectric substrates, providing that the boundary conditions on the surface cause a slowing down effect [32]. Thus, a wave with a velocity slightly smaller than the velocity of the SH-BAW will be supported. According to Snell´s law, this wave cannot couple energy to the faster SH-BAWs in the substrate, and thus remains confined to the surface. Some materials that possess a specific crystallographic symmetry have a pure SH-type SAW propagation mode accompanied by Φ. This kind of wave is known as *Bleustein-Gulyaev* (BG) wave [43, 44]. Here the slowing down effect is caused by the abrupt break of piezoelectricity and dielectric permittivity at the surface. Near the surface, the intensity of the electric field decreases. Thus, the near-surface region appears “slower” than the region in the depth of the half-space and allows to localize the wave. The reduction of velocity is a measure of how strong the piezoelectricity (*electromechanical coupling*) is near the surface. The guiding mechanism of SH-type SAW that relies on the electromechanical coupling K^2 allows to effectively concentrate wave energy at the surface, as the increase in SAW piezoelectricity intensifies the effects of the electrical boundary condition. It is worth noting that metallization present on the surface of a piezoelectric material concentrates the propagation of SH-type SAWs much closer to it, as compared to a free surface, due to the electrical short-circuiting effect which practically cancels the piezoelectricity at the surface [34].

SH-type SAWs can also appear in layered materials with low shear wave velocity. This mode is referred to as *Love* wave [45, 46]. Along with that, periodic surface roughness, for example a grating on the propagation surface, also allows to generate SH-SAWs, the *surface transverse waves* (STW) [47]. In all of the above cases, the energy confinement to the surface is caused by a slowing-down effect near the surface.

More generally, Rayleigh-type and SH-type SAWs propagate as a “quasi” RSAW and SH-SAW due to the anisotropic nature of piezoelectric materials, because both SH and Φ components generally couple with the L and SV components. As a result, these waves can possess three mechanical components and Φ [32]. In case when the velocity of a slow-shear SH-type BAW is smaller than that of a “quasi” RSAW, the SH-component no longer concentrates its energy close to the surface. The SH-type wave will still propagate while accompanied by a weak-amplitude slow shear bulk wave radiation into the substrate. Such

"leakage" of energy will result in attenuation of the wave. Strictly speaking, a *leaky* acoustic wave is not a surface wave [48], due to a partial bulk component that grows as a function of material depth. In a similar way, the "quasi" SH-type SAW with a velocity greater than the velocity of an SV-type BAW becomes leaky. There is also a situation when the SAW is not leaky, even when the velocity conditions are satisfied. BG waves are an example, where the components are completely decoupled due to the symmetry in the substrate's crystal orientation. The leaky SAW is treated as *non-leaky* when coupling with the slow-shear component is negligible, resulting in a low propagation loss. This loss critically depends on boundary conditions that define the mechanism of components coupling at the surface. It is worth noting that leaky waves have the strongest coupling coefficient, along with a relatively high velocity that is important for high frequency applications [5]. Thick Au metallization allows for a leaky SAW to be converted to a non-leaky SAW due to the decrease in the velocity of the wave propagating through it [49].

Other examples of wave propagation modes include *Lamb* modes (wave propagation in plates with polarization in sagittal plane) [50], *shear plate* modes (SH-type waves that propagate in plates) [51], *Stoneley* waves can propagate along the interface between a solid and a liquid, or two solids [52].

Some important features that define the properties of surface acoustic waves on piezoelectric substrates are [32]:

1. ***SAW velocity***, a constant relating the frequency ω and magnitude of the wave-vector **k**;
2. ***Piezoelectric coupling constant K^2***, a numerical measure of conversion efficiency between electrical and acoustic energy in a piezoelectric material. In SAWs, K^2 is defined in the same way as for the plane bulk waves. Here, it is related to the relative velocity shift of SAWs propagating under electrically free and metallized surfaces, respectively:

$$\boldsymbol{K^2} = \frac{2(V_f - V_m)}{V_f} \tag{2.8}$$

where V_f and V_m are SAW velocities on free and metallized surfaces, of a piezoelectric material;

3. ***Temperature stability***, important for a continuous performance within the defined specification over a course of time when the material is exposed to various environmental variations;

4. ***Beam steering***, occurs when the direction and speed of the power flow do not coincide with the direction and speed of the wave vector. The propagation speed of power flow, or *group velocity,* defines a technological requirement of how precisely piezoelectric crystals have to be grown and cut, along with how accurately the elements that excite acoustic waves have to be aligned with the orientation of a substrate;
5. ***Material-related losses***, due to the thermal lattice vibrations, surface roughness, leakage into air, etc. Generally, shear waves possess lower propagation loss when compared to the longitudinally polarized waves. Also, materials with larger electromechanical coupling tend to show higher propagation losses (i.e. they appear softer);
6. ***Permittivity***, determines the capacitive impedance of the excitation metallization that is often designed to be around 50 Ω in order to get a perfect matching with the peripheral electronics;
7. ***Propagation losses***, often SAW energy can scatter into bulk modes through the diffraction or surface perturbation. It is also possible for bulk modes to be generated directly at the surface. These effects lead to spurious responses that have to be suppressed in practical device design.

Among the commonly used substrate materials are $LiNbO_3$, $LiTaO_3$, Quartz, thin films of ZnO and AlN, and some others. Single-rotated cut angle substrates are usually specified by the rotation angle from one of the crystal axes e.g. 128˚ YX-$LiNbO_3$ (128˚-rotated Y-cut X-propagation $LiNbO_3$) the crystal is cut at the plane rotated 128˚ from the Y-plane about the X-axis.

2.4 SAW DEVICES

2.4.1 EXCITATION AND DETECTION OF SAWS

SAWs can be excited and detected efficiently by using an *interdigital transducer* (**IDT**) placed on a piezoelectric substrate, as discovered by White and Voltmer in 1965 (*Fig. 5*) [53]. The IDT consists of a series of interleaved metal film electrodes deposited on a substrate. In this way, the acoustic energy is confined at the surface of a device in the range of its acoustic wavelength regardless of the substrate thickness. Thus, the wave gets very sensitive towards any change on the surface e.g. mass loading, change of viscosity and conductivity. This is of a

great importance as very fine IDTs can be mass-produced easily using standard microfabrication techniques, facilitated greatly by rapid advances in the microelectronics and *MEMS* (Micro Electro Mechanical Systems) industries [54]. Upon application of a sinusoidal voltage *V* of frequency *f* to the IDT, an electric field will be formed that causes a strain pattern through the piezoelectric effect with periodicity equal to 2*d*, where *d*, the grating pitch, is the distance between the centers of the electrodes. The *width of the electrodes* in IDT is usually equal to the width of *inter-electrode gap* allowing for maximum conversion efficiency of electrical signal into mechanical and vice versa. Although surface acoustic waves excited from each period may be weak, they add up and grow. Mechanical and electrical impedance discontinuity, due to the short-circuiting by the conductivity of a metallic film, present at each electrode's edge, causes SAW reflections. Additionally, charges induced in metal strips regenerate the SAW [34]. This *electric regeneration* is equivalent to reflection. However, the nature of these reflections depends on the exact electrical connection among the strips. IDT characteristics are defined by the *geometry of a finger per period*, the *number of finger-pairs*, and the *substrate material*. To tune the impedance of an IDT, one can adjust its *aperture.* Many variations of IDT geometries are possible, resulting in a wide variety of possible devices.

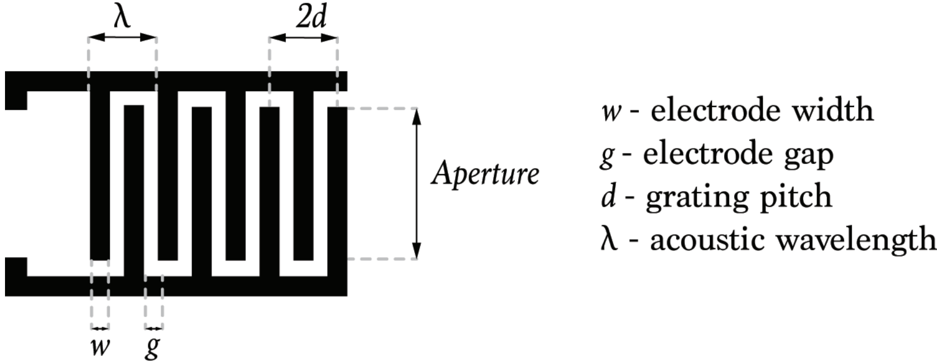

Figure 5. Schematic diagram of an IDT.

The operation frequency of a SAW component typically ranges from 10 MHz to several GHz. When 2*d (*defined through frequency *f)* is close to the surface acoustic wave wavelength, the surface wave is launched in two opposite directions away from the transducer. This causes a corresponding electric field in the output transducer (*Fig. 6*), and thus, the voltage at the impedance Z_L. The magnitude of the output signal is a function of the ratio between the signal's wavelength and 2*d*. When 2*d* is equal to the wavelength, the output voltage is at maximum. The frequency that corresponds to this condition is the *center* or *synchronous frequency* of the device. When the frequency shifts from the center frequency, the magnitude of the output voltage decays.

The SAW velocity depends on the substrate material and is about 10^5 times lower than that of an electromagnetic wave. In case when the electrodes are equally spaced as shown in *figure 5,* the phase characteristic is a linear function of frequency, i.e., the time delay is constant in the given frequency range. Therefore, SAW *delay lines (transversal filters)* can be constructed (*Fig. 6*) [55]. The phase characteristic of a delay line is a function of the distance between IDTs, while the amplitude of the wave is proportional to the number of electrodes and their length.

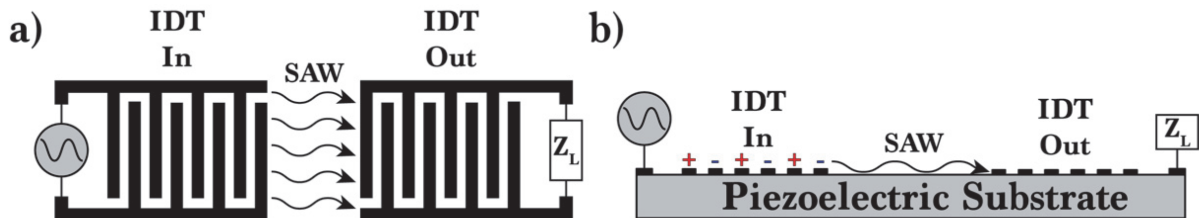

Figure 6*.* Excitation and detection of a surface acoustic wave using a pair of IDTs (delay line configuration). The input IDT launches the wave, while the output IDT receives it. **a)** top view; **b)** side view.

2.4.2 SAW Resonators

Another class of SAW devices comprises the SAW *resonators*. A one-port SAW resonator (*Fig. 7a*) consists of an IDT that is used for both input and output transductions, and an array of reflective gratings located on both sides of the transducer. When the input electrical signal is applied, a mechanical wave is generated in a piezoelectric substrate that travels from both sides of an IDT towards the reflective array. The reflected wave then travels back to the IDT and gets converted into an electric signal, respectively. These correspond to contributions from elasticity and inertia. C_0 is the static capacitance of the IDT, while R_m is the motional resistance corresponding to damping effects.

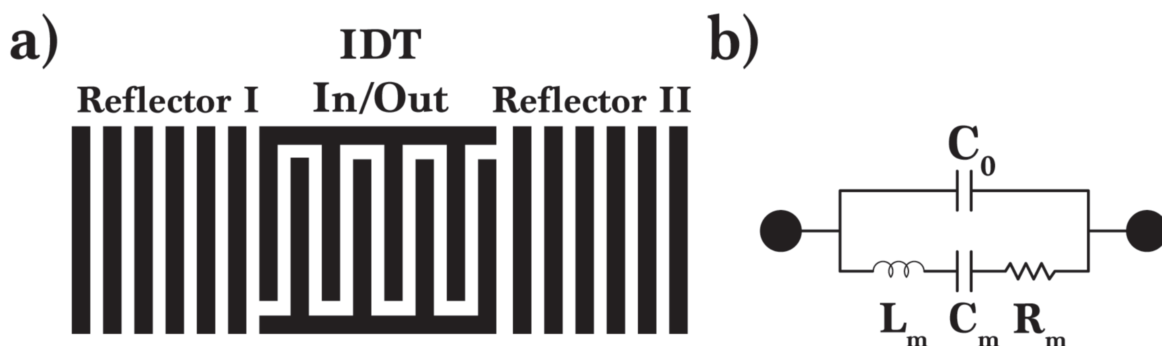

Figure 7*.* **a)** Schematic representation of a one-port SAW resonator. **b)** Its equivalent electrical circuit.

Similarly, in a two-port SAW resonator (*Fig. 8*), a pair of reflectors is added at the outer side of both the input and the output transducers. The transfer admittance of the device becomes very large at resonance when the IDT and reflector resonances are matched. This leads to a narrow, but very low-loss passband.

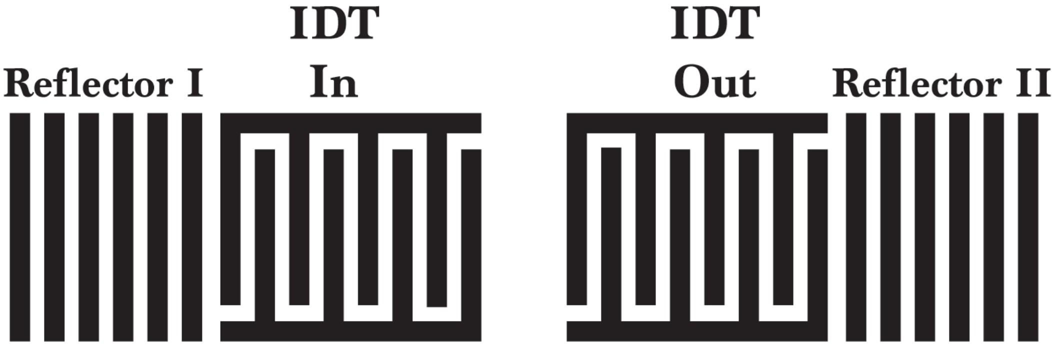

Figure 8. Schematic representation of a two-port SAW resonator.

Figure 9 shows some typical reflector arrangements. (a) depicts an *open-circuit* (**OC**) grating with each strip being electrically isolated. (b) shows a grating that is connected electrically in parallel (*short-circuit* or **SC**), and (c) shows a combination of both, which is referred to as *positive and negative reflection* (**PNR**) type grating. It offers the highest reflection coefficient among the three [32].

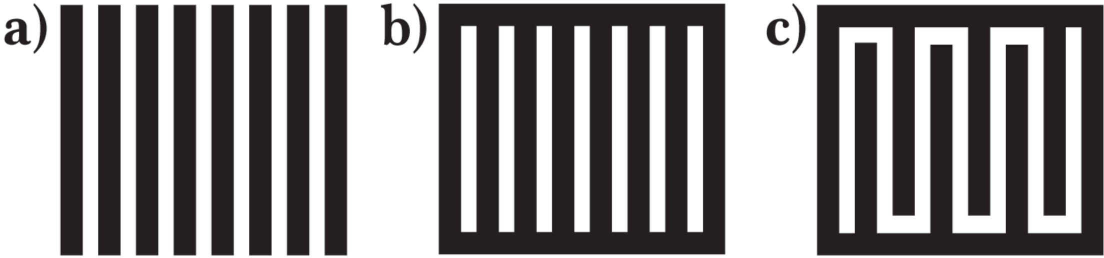

Figure 9. Schematic representation of various metallic gratings: **a)** open circuit; **b)** short circuit; **c)** positive and negative reflection type gratings.

2.4.3 SAW Resonator Characterization

Figure 10 shows typical electrical resonance characteristics of a one-port SAW resonator. Antiresonance frequency f_a exists just above the resonance frequency f_r, where the *conductance* **G** (1/R) is at maximum [32].

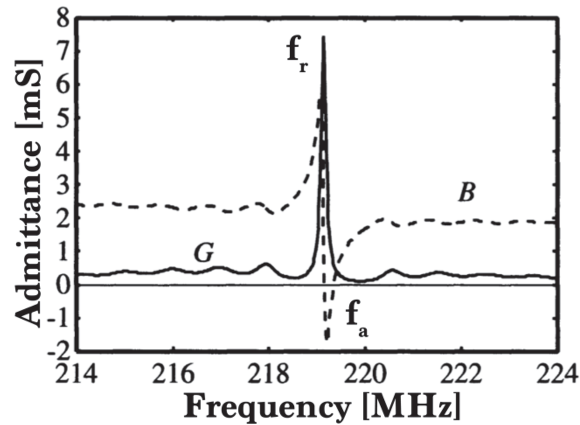

Figure 10. Electrical resonance characteristics of a one-port SAW resonator. *B* is the *susceptance*, and *G* is the *conductance* [32].

From the equivalent circuit model (*Fig. 7b*):

$$f_r = \frac{1}{\sqrt{L_m C_m}} \text{ and } f_a = \frac{1}{\sqrt{\frac{L_m C_m C_0}{C_m + C_0}}} \tag{2.9}$$

The capacitance ratio γ is often used a measure of the resonator performance:

$$\gamma = \frac{C_0}{C_m} = \frac{1}{(\frac{f_a}{f_r})^2 - 1} \tag{2.10}$$

The *quality factor* **Q** is a dimensionless parameter that describes how underdamped the resonator is. It is defined as the ratio of the stored energy to the dissipated energy in a half cycle. Q at the resonance frequency is Q_r (*resonance Q*) and expressed as:

$$Q_r = \frac{\omega_r L_m}{R_m} = \frac{1}{f_r C_m R_m} \tag{2.11}$$

Admittance **Y** describes how easily a circuit will allow current to flow in it. It can be expressed using the equation below, where *conductance* G is the real part of admittance, whereas *susceptance* B is imaginary:

$$Y \propto \frac{j}{1 + (\frac{j\omega}{f_r})^2 + \frac{j}{Q}} \tag{2.12}$$

There is a number of ways to estimate Q. For example, it can be calculated from the inverse of the fractional width between frequencies where the conductance G becomes the half height of its peak ($|Y|$ $reduces\ to$ $\frac{1}{\sqrt{2}}$ of its peak). Other methods rely on estimation of the *group delay* (τ_{gd}), which is the time constant of the impulse response.

Frequency of operation f, *effective electromechanical coupling coefficient* k_{eff}^2 and *quality factor* Q are the parameters used for characterizing the performance of acoustic resonators. They determine two descriptive *figures of merit* (FOM): the products $k_{eff}^2 \times Q$ and $f \times Q$. Series and parallel resonant frequencies, as well as k_{eff}^2 can be defined through the Mason's one-dimensional model for a *free resonator* (piezoelectric plate with both sides metallized). Even though this model is idealized, it can be still used to describe real SAW devices.

Electromechanical Coupling Coefficient

In Mason's one-dimensional model, the *resonant cavity* acts similarly to an acoustic transmission line [56]. Two stress-free boundary planes are attached to the piezoelectric slab at $z_1 = d/2$ and $z_2 = -d/2$ where an acoustic wave motion propagating along the vertical z-axis is induced *(Fig. 11)*. Each plane has a thickness of $d = z_1 - z_2$. The electric field applied externally will coincide with the direction of wave propagation, also known as *thickness excitation* (TE). The case when the applied electric field is perpendicular to the direction of wave propagation is referred to as *lateral field excitation* (LFE). In case of surface acoustic waves, these excitation regimes are referred to as *in-line field excitation* when the electric field is parallel to the

propagation vector and *crossed-field excitation,* when the applied electric field is normal to the acoustic propagation vector [57]. As a result of this excitation, two waves will propagate in opposite directions inside the slab from each boundary. The constructive interference of these two counters- propagating waves defines the resonant behavior of the resonator.

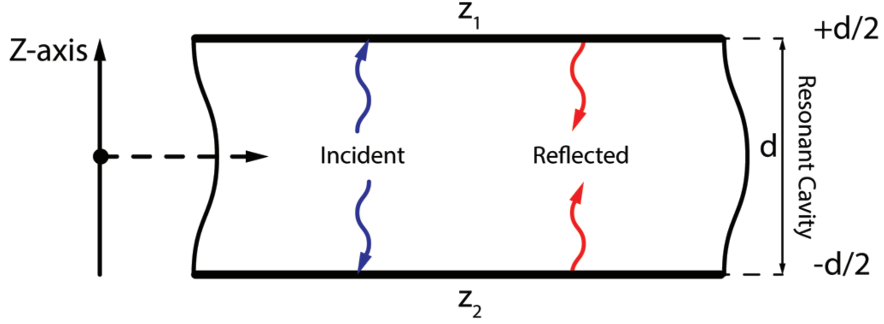

Figure 11. Schematic representation of excited waves inside a resonant cavity.

Thus, the solution to the system is a superposition of plane waves travelling in forward and backward directions:

$$u = (ae^{-jkz} + be^{jkz})e^{j\omega t} \tag{2.13}$$

where *u* is a particle displacement, $\omega = 2\pi f$ is the angular frequency, $k = \omega/V_{Wave}$ is a wave number, and V_{Wave} is the velocity of the acoustic wave. The particles displacement at each boundary then becomes:

$$u_1 = (ae^{-jkd/2} + be^{jkd/2})e^{j\omega t} \tag{2.14}$$
$$u_2 = (ae^{jkd/2} + be^{-jkd/2})e^{j\omega t} \tag{2.15}$$

To define the electrical impedance of the resonator, piezoelectric constitutive equations for the stress and electrical displacement written in one-dimensional form are used:

$$T_3 = c_{33}^E S_3 - e_{33} E_3 \tag{2.16}$$
$$D_3 = \varepsilon_{33}^S E_3 + e_{33} S_3 \tag{2.17}$$

where T_3 is the mechanical stress, S_3 is the mechanical strain, E_3 is the electric field and D_3 is the electric displacement in z-direction, while c_{33}^{E}, e_{33} and ε_{33}^{S} are material-defined values for stiffness, piezoelectricity and dielectric constants, respectively. Equation 2.16 is valid when the electric field is constant. At the same time, the electric displacement $\vec{D}$ should fulfill the Poisson's equation $\nabla \cdot \vec{D} = \rho_f$, where ρ_f is free charge volume density. However, there are no free bulk charges in dielectrics. This makes $\nabla \cdot \vec{D} = 0$, resulting in constant electric displacement rather than an electric field. Furthermore, in case when only electro-acoustic waves are considered, the electric displacement becomes zero since the polarizations caused by the elastic strain and the electric field cancel each other [33]. Thus, the relation between mechanical stress and strain induced by the acoustic wave can be described as following:

$$T_3 = \left[c_{33}^{E} + \frac{(e_{33})^2}{\varepsilon_{33}}\right] S_3 = c_{33}^{D} S_3 \tag{2.18}$$

where $c_{33}^{D}$is the stiffened elastic modulus:

$$c_{33}^{D} = c_{33}^{E}\left[1 + \frac{(e_{33})^2}{c_{33}^{E}\varepsilon_{33}}\right] \tag{2.19}$$

The value of c_{33}^{D} determines the acoustic wave velocity stiffened by the presence of piezoelectricity [33]:

$$V'_{wave} = \sqrt{\frac{c_{33}^{D}}{\rho}} \tag{2.20}$$

where ρ is the density of the medium. Term $\frac{(e_{33})^2}{c_{33}^{E}\varepsilon_{33}}$ in equation 2.19 is a *piezoelectric coupling constant* $\mathbf{K^2}$.

Since there is no external mechanical loading at the boundary planes, the total stress is zero. Thus, by combining equations 2.14, 2.15 and the equation 2.16 for the stress (which equals to zero at both surfaces), and adding the external electric field, one can obtain the relation between the mechanical and electrical components of the field [33]:

$$\omega \frac{Z}{\sin(kd)}(u_1 - u_2) - \omega Z \tan\left(k\frac{d}{2}\right)u_1 + \frac{I(\frac{e_{33}}{\varepsilon_{33}^S})}{j\omega} = 0 \tag{2.21}$$

$$\omega \frac{Z}{\sin(kd)}(u_1 - u_2) + \omega Z \tan\left(k\frac{d}{2}\right)u_2 + \frac{I(\frac{e_{33}}{\varepsilon_{33}^S})}{j\omega} = 0 \tag{2.22}$$

where A is the resonator area, $I = j\omega A D_3$ is the displacement current, $Z = A\sqrt{c_{33}^D \rho}$ is the acoustic impedance.

The total electric field consists of two components: *external* (from the applied voltage) and *internal* (from the strain-induced electric field). The electric displacement generated by the acoustic wave is zero:

$$E_3 = \frac{D_{33}^{ext}}{\varepsilon_{33}^S} - \frac{e_{33}}{\varepsilon_{33}^S}\frac{\partial u}{\partial z} \tag{2.23}$$

By substituting equation 2.23 into the voltage equation $V = \int_{z_1}^{z_2} E_{33} dz$, one can define the analytic expression for the current:

$$I = j\omega C_0 V - j\omega(\frac{e_{33}}{\varepsilon_{33}^S})C_0[u_1 - u_2] \tag{2.24}$$

where $C_0 = \frac{\varepsilon_{33}^S A}{d}$ is the static capacitance of the plate.

By combining equations 2.23 and 2.24, one can obtain the expression for the electrical impedance of the resonator:

$$Z_{in} = \frac{V}{I} = \frac{1}{j\omega C_0}\left[1 - k_t^2 \frac{\tan(\frac{kd}{2})}{\frac{kd}{2}}\right] \tag{2.25}$$

where $k_t^2 = \frac{e_{33}^2}{c_{33}^D \varepsilon_{33}^S}$ is the *intrinsic electromechanical coupling coefficient*, which is a measure of how efficiently electrical energy is being transformed into mechanical energy of the elastic deformation. Theoretic calculation of k_t^2 can be done using the following equation:

$$k_t^2 = \frac{(V'_{Wave})^2 - (V_{Wave})^2}{(V_{Wave})^2} \tag{2.26}$$

where V_{Wave} is the acoustic wave velocity on a non-stiffened surface.

The frequency at which impedance becomes zero (infinite admittance) is the *resonance frequency* f_r, while the frequency at which the impedance becomes infinite (zero admittance) is the *antiresonance frequency* f_a (*Fig. 10*). These are also known as series and parallel resonances, respectively. Impedance can be expressed using the following expression [58]:

$$\frac{\tan(\frac{kd}{2})}{\frac{kd}{2}} = \sum_{N=1}^{\infty} \frac{8}{(N\pi)^2 - (kd)^2} \tag{2.27}$$

where *N=1, 3, 5, 7*, … represents the harmonics of the operation. The poles of this function (infinite impedance) occur at $\frac{kd}{2} = \frac{N\pi}{2}$. The relationship between the wave number and frequency is $k = 2\pi f / V'_{Wave}$. This gives the antiresonance frequency:

$$f_a = \frac{V'_{Wave} N}{2d} \tag{2.28}$$

At resonance $Z_{in} = 0$ and according to the equation 2.25, this gives $k_t^2 \frac{\tan(\frac{kd}{2})}{\frac{kd}{2}} = 1$. From equation 2.27, the resonant frequency of the Nth pole is:

$$f_r^{(N)} = \frac{V'_{Wave}}{2\pi d} \sqrt{(N\pi)^2 - 8k_t^2} \tag{2.29}$$

This allows to express the electromechanical coupling in terms of relative separation between both frequencies of the fundamental harmonic:

$$\frac{f_a - f_r}{f_a} \approx \frac{1}{2}\frac{f_a^2 - f_r^2}{f_a^2} = \frac{k_t^2}{\pi^2} \tag{2.30}$$

or

$$k_t^2 \approx \frac{\pi^2}{4}\frac{f_a - f_r}{f_a} \tag{2.31}$$

However, in real devices the impedance and admittance are not infinite. For that reason, the resonance is defined around the frequency with minimum impedance (maximum admittance) and the phase crosses zero with a negative slope. Antiresonance occurs when the impedance is at maximum (admittance is at minimum) and the phase crosses zero with a positive slope (*Fig. 10*).

Equation 2.31 can be used for the calculation of *effective electromechanical coupling coefficient* by measuring the resonant and antiresonant frequencies of a real resonator:

$$k_{eff}^2 = \frac{\pi^2}{4}\frac{f_a - f_r}{f_a} \tag{2.32}$$

Quality Factor of a Resonator

The quality factor ***Q*** is one of the most important parameters characterizing resonator performance, and it can be defined as the ratio between the stored and dissipated energy per wave cycle:

$$Q = \omega \frac{Energy\ stored}{Power\ dissipated\ per\ one\ cycle} \tag{2.33}$$

In other words, it is a measure of a relative loss of energy in the resonator that originates from acoustic, electric and dielectric losses. The quality factor in real devices is usually extracted from the slope of the impedance (or admittance) phase curves Φ_Z (Φ_Y) at resonance and antiresonance [59]:

$$Q_{r,a} = \frac{f_{r,a}}{2}\left|\frac{d\Phi_z}{df}\right|_{f_{r,a}} \tag{2.34}$$

Expression 2.34 can be used as an implicit indicator of resonance and antiresonance frequencies [60]: the series resonance is at the maximum Q near minimum impedance, while the parallel resonance is defined as the condition of maximum Q near maximum impedance.

The quality factor deteriorates when the resonator is connected to an external periphery. For that reason, when various resonator technologies are compared, it is important to be able to accurately determine the *unloaded quality factor*. Based on the theorem derived by Bode [61], Rich Ruby has developed an algorithm for obtaining *unloaded Q* of any real resonator from the measured scattering parameters (S_{11} reflection coefficients, see section *Electrical Characterization*) [62]:

$$Q_B = \omega \cdot \tau_{gd} \frac{|\Gamma|}{1 - |\Gamma|^2} \tag{2.35}$$

where $\tau_{gd} = -\frac{d\varphi}{d\omega}$ is the measured *group delay*, φ and Γ are phase and magnitude of the reflection coefficient, respectively. Equation 2.35 allows to determine the dependence of Q_B on frequency.

Electrical Characterization

For the analysis of SAW devices, a network analyzer can be employed to measure scattering coefficients. One- or two-port SAW circuits are connected to it with a transmission line typically having an impedance of 50 Ω. *Figure 12b* shows schematic representation of a linear two-port circuit, where the signal a_i is incident to it, while b_i is reflected. Both a_i and b_i

are normalized, so that the power corresponds to their square i.e. 0 dBm of power correspond to $|a_i|^2$ of 1 mW.

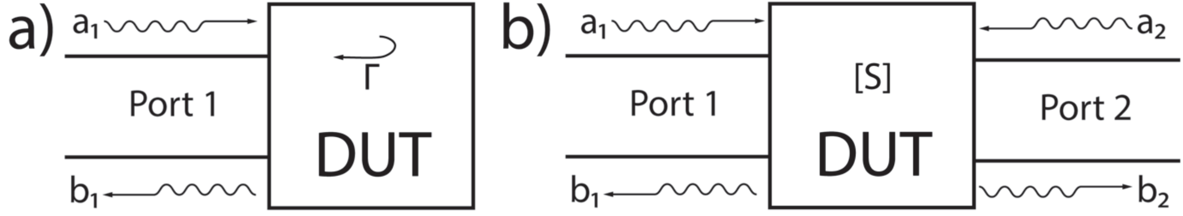

Figure 12. Incident and reflected signals from a liner **a)** one-port device under test (DUT); **b)** two-port DUT.

linear combination of a_i can be used to express b_i, where the matrix element S_{ij} is the *scattering coefficient* (or S-parameter) [63]:

$$\begin{pmatrix} b_1 \\ b_2 \end{pmatrix} = \begin{pmatrix} S_{11} & S_{12} \\ S_{21} & S_{22} \end{pmatrix} \begin{pmatrix} a_1 \\ a_2 \end{pmatrix}$$

The S-parameter for a one-port network is given by a simple 1 x 1 matrix. The device characteristics remain unchanged when the input and output ports are swapped due to the reciprocity. This means that $S_{12} = S_{21}$. When the circuit is *symmetrical* (ports are equivalent), the relation $S_{11} = S_{22}$ holds. Matrix components S_{11} and S_{22} are often referred to as the *reflection coefficient* and denoted as "Γ". Matrix components S_{12} and S_{21} are often referred to as the *transmission coefficient* and denoted as "T". Additionally, $-20\log|S_{11}|$ and $-20\log|S_{22}|$ are *return losses*, while $-20\log|S_{12}|$ and $-20\log|S_{21}|$ are *insertion losses*.

For one-port *device under test* (DUT) (*Fig. 12a*) that is connected to the transmission line of a specific impedance $R_0 = G_0^{-1}$, reflection coefficient Γ is given by [32]:

$$\Gamma_0 = \frac{G_0 - Y}{G_0 + Y} = \frac{Z - R_0}{Z + R_0} \tag{2.36}$$

The general definition of admittance $Y = G + jB$ allows to obtain the following equation:

$$|\Gamma|^2 = \left|\frac{G - G_0 + jB}{G + G_0 + jB}\right|^2 = 1 - \frac{4GG_0}{(G + G_0)^2 + B^2} \quad (2.37)$$

Assuming that $G_0 \gg G, |B|$:

$$-20\log|\Gamma| \cong {}^{40G}/_{G_0} \quad (2.38)$$

This implies that the radiation conductance of the connected IDT is in direct relation with the frequency response of the return loss. *Figure 13* shows the reflection coefficient response (S_{11}) of an IDT schematically [32]:

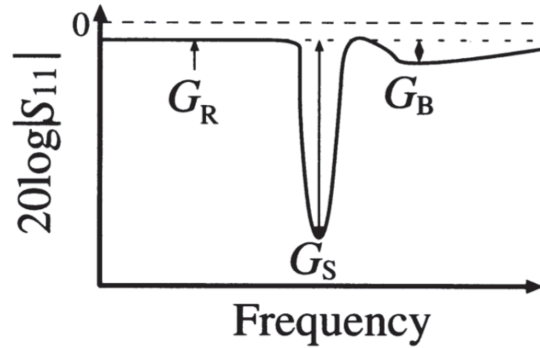

Figure 13. Return loss properties of the DUT. $\mathbf{G_R}$ is related to electrode resistivity and almost independent of frequency. $\mathbf{G_S}$ is due to the SAW radiation and exhibits a strong peak. $\mathbf{G_B}$ has a cut-off because of BAW radiation [32] (see section on *Spurious Responses*).

The plot for Γ_0 on the complex plane as a function of frequency draws a contour within a unit circle (*Smith chart, Fig. 14 [32])*. The curve for Γ is obtained from the clockwise rotation of the curve for Γ_0. IDTs are capacitive, and $Y \propto j\omega$ at off-resonance, so that $\Gamma = 0$ at $\omega = 1$. As ω increases, Γ rotates clockwise. At $\omega \rightarrow \infty$, $\Gamma = -1$. Γ approaches the center of the circle at non-zero conductance, while at resonance its contour is a circle. From the Smith chart, one can see the mode of operation of a resonator (inductive or capacitive). While the point where the semi-circle contour crosses the horizontal line is where the admittance is a real number. The curly loops indicate spurious modes in the resonator response.

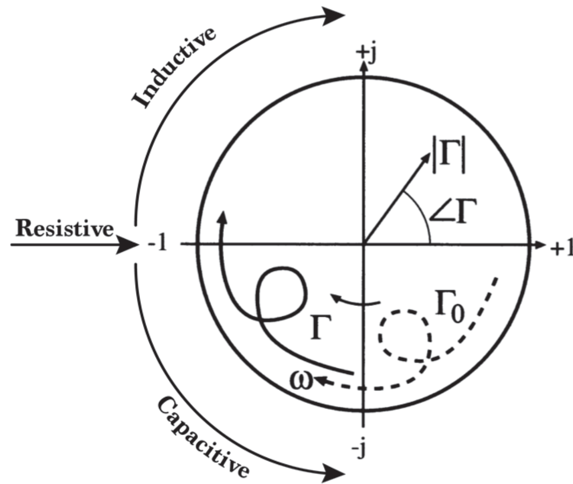

Figure 14. Smith chart (admittance chart) showing scattering coefficients in complex plane [32].

Spurious Responses

SAWs propagating back and forth in a resonant cavity cause unwanted dissipation of their energy through diffraction, which affects the resonator performance. To evade this problem, *energy trapping for the transverse direction, i.e.,* total reflection at the boundary between the gratings and side-stripes that connect them together, is used to guide the acoustic energy in a transverse direction. However, higher-order resonances can appear when the trapping is strong. These resonances are *inharmonic spurious responses* (or *higher order transverse mode resonances*) near the main resonance.

Usually IDTs also radiate bulk acoustic waves that propagate at frequencies higher than the SAW excitation frequency [32]. Since the BAWs are not efficiently reflected by the reflectors, the spurious BAW response is not significant in resonators. However, because the energy leak due to the BAW radiation still results in a reduction of the resonance Q, it should be considered when high performance device is required [64].

Spurious responses can cause an undesirable jump in the oscillation frequency, or ripples in the passband, along with undesirable peaks in the rejection band. Suppression of spurious modes can be achieved by a number of techniques that include apodization, aperture/overlap lengths variations and some other [Paper I].

2.5 MICROFLUIDICS

Microfluidics studies the manipulation of fluids and their behavior in sub-millimeter-sized systems at low Reynolds numbers [65]. Typical volume of solutions ranges from 10^{-9} to 10^{-18} liters. Among the advantages of microfluidics are:

- Reduced amount of samples required;
- Improved analysis and detection speeds;
- Compactness;
- Cost reduction;
- Range of "*micro* domain effects" (laminar flow, electrowetting, etc.).

Like all microsystems, microfluidic devices are affected by scaling laws. It means that when scaling down a system to the microscale, the volume forces become less dominant, while surface forces gain more significance [66]. An example of consequences of down-scaling are laminar flow phenomena with steady parallel flow patterns of fluids in contrast to the macroscale turbulent flow. While on the macroscale turbulence causes rapid convective mixing of liquids, on a microscale mixing is a comparatively slow diffusion driven process.

Microfluidics has a wide range of applications, most notably ink-jet printing, with a steady increase in life sciences and analytical chemistry. It is actively being used in biology due to the similar dimensions of cells and microfluidic channels. Most commonly, microfluidic devices are used for analytical purposes (diagnostics, sensing, sample processing), but also in chemical synthesis, although this application is often limited by the achievable throughput. Analytical applications also benefit from microfluidics due to the possibility to perform entire analyses within one highly integrated system [22, 27, 67].

2.5.1 FLUID FLOW INSIDE A MICROFLUIDIC CHANNEL

The motion of fluids can generally be described by the Navier-Stokes equation, which also applies to microfluidic systems. It arises from Newton’s second law applied to fluid motion. By assuming that the stress induced on a liquid is the sum of viscous force and a pressure gradient, an equation describing incompressible flow of fluid of a constant viscosity can be obtained [66]:

$$\rho(\frac{\partial \boldsymbol{v}}{\partial t} + \boldsymbol{v} \cdot \nabla \boldsymbol{v}) = \rho \boldsymbol{g} - \nabla P + \mu \nabla^2 \boldsymbol{v} \tag{2.39}$$

where $\boldsymbol{\rho}$ is the density, **P** is pressure, μ is the fluid viscosity and $\boldsymbol{g}$ is a gravitational acceleration. Here, term $\mu \nabla^2 \boldsymbol{v}$ accounts for viscous forces and $\rho(\frac{\partial \boldsymbol{v}}{\partial t} + \boldsymbol{v} \cdot \nabla \boldsymbol{v})$ represents inertia. Re-writing the Navier-Stokes equation in a dimensionless form, where "**~**" denotes dimensionless analogues of the originals:

$$\underbrace{\frac{\rho v L}{\mu}}_{Re}(\frac{\partial \tilde{v}}{\partial \tilde{t}} + \tilde{v} \cdot \tilde{\nabla} \tilde{v}) = -\nabla \tilde{P} + \mu \tilde{\nabla}^2 \tilde{v} \tag{2.40}$$

reveals a single scaling parameter, the Reynolds number (*Re)*, which represents the relationship between inertia and viscous forces:

$$Re = \frac{L \rho v}{\mu} \tag{2.41}$$

where L is the characteristic length, ρ is the density, v is the velocity and μ is the dynamic viscosity of the fluid. In case of $Re \gg 1$, inertia dominates, resulting in turbulent *flow*. If $Re \ll 1$, the viscous and pressure terms start to dominate, and the flow is considered to be *laminar (Fig.15)*. Such a flow is characteristic for microfluidic systems due to the small length scale of their channels and the slow flow rate.

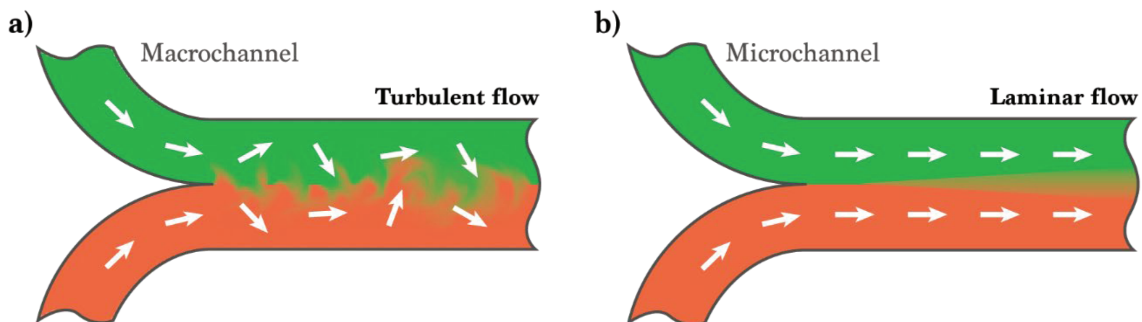

Figure 15*.* **a)** Turbulent and **b)** Laminar flow modes.

Due to the fact that microfluidic systems operate at low *Re,* inertia and $\boldsymbol{g}$ can be neglected. The equation then can be rearranged as follows (*Stokes' equation*):

$$\nabla P = \mu \nabla^2 \boldsymbol{v} \tag{2.42}$$

Stokes' equation can be solved analytically for a number of channel geometries by applying boundary conditions. Flow of liquid inside a microfluidic channel is typically subject to no-slip boundary conditions, meaning that the velocity field is zero at the wall and maximum at the center, giving a parabolic velocity profile. Such a motion can be achieved by applying a pressure difference between the two ends of the channel. The resulting flow fields can be integrated over the cross section to get an expression for the total flow rate. The equations 2.43 and 2.44 allow to calculate the flow rate *Q* in rectangular and square channels, respectively [66]:

$$Q = \Delta p \frac{h^3 w}{12 \mu L} [1 - 0.63 \frac{h}{w}] \tag{2.43}$$

and

$$Q = \frac{\Delta p w^4}{28.4 \mu L} \tag{2.44}$$

where Δp is the drop of applied pressure, w is a channel's width, h is a channel's height, L is the total length and μ is the fluid viscosity.

2.5.2 Mass Transport and Diffusion

Diffusion is one of the transport modes, and can be described as the unavoidable, random motion of particles along a concentration gradient, which results in a net flux of material from the regions of high concentration to the regions of low concentration. For pure diffusion to occur, the velocity field of the fluid should be zero. However, when the velocity field is non-zero the motion of molecules is also partly due to convection, since they are being

carried by the fluid. The change in concentration over time in such a system can be described using the *convection-diffusion* equation [66]:

$$\frac{\partial c}{\partial t} = -\vec{v} \cdot \nabla c + D\nabla^2 c \qquad (2.45)$$

where the left and right parts represent change of concentration over time ($\frac{\partial c}{\partial t}$) and its relation to convective flow transport ($-\vec{v} \cdot \nabla c$), and diffusion ($D\nabla^2 c$). Converting this equation to a dimensionless form will show that it depends on two scaling parameters *St* and *Pe*. *St*, the *Strouhal* number, describes unsteadiness, while *Pe*, the *Peclet number*, describes the ratio between the convective and diffusive mass transports. The following equation is used to obtain *Pe*:

$$Pe = \frac{lv}{D} \qquad (2.46)$$

where l is the characteristic length, v is the velocity and D is the diffusion coefficient. *Pe* can be further related to *Re*:

$$Pe = \frac{\mu}{D\rho} \cdot Re \qquad (2.47)$$

where $\frac{\mu}{D\rho}$ constitutes the ratio between the rates of viscous diffusion and mass diffusivity. The dimensionless numbers are useful in the engineering context to easily characterize and compare the performance of microfluidic devices.

3 ANALYTICAL TECHNIQUES

3.1 SENSORS

A sensor, in broad terms, is a device that detects events or changes in its environment and converts the information by means of a transducer into a signal that can be (typically electronically) processed. As there are countless instances of measurement applications, a large variety of different sensor types exists. Sensors as analytical devices can be generally characterized by figures of merit, which include [68]:

1. ***Sensitivity*** is often defined in terms of the relationship between input and output signal. In other words, it is the ratio of its response to the magnitude of a quantity being measured (*measurand or analyte*). For example, high sensitivity refers to a small change in temperature that generates a large output voltage in a temperature sensor;
2. ***Bandwidth (span)*** defines the range of input signals that can be converted to output signals by the device. In some cases, signals outside this range will cause unacceptably large inaccuracy or simply not operate at all;
3. ***Accuracy*** is the maximum expected error that can occur between the actual and ideal output signals;
4. ***Hysteresis*** is a material related property that results in deviation of output values relatively to the input stimulus cycling. In other words, it is the width of the expected output deviation errors in terms of measured quantity;
5. ***Non-/Linearity*** is the maximum deviation from the functional relationship between input and output signal over the specified dynamic range;
6. ***Noise*** is a signal added to the useful output signal through the device operation itself;
7. ***Limit of detection*** is the lowest detectable concentration change of a measurand in the presence of noise;
8. ***Resolution*** is the lowest detectable incremental change of an input parameter that can be still identified in the output signal;
9. ***Dynamic range (frequency response)*** is defined by finite response times to an instantaneous change in input signal;

10. ***Selectivity*** is the ability of a sensor to discriminate between the analyte of interest and possible interferences. In chemical and biological measurements this characteristic in most cases is achieved by means of analyte-specific surface coatings [69];
11. ***Reversibility*** is the ability of a sensor to recover after exposure to an analyte (i.e. return to its original background/baseline condition).

3.1.1 Electro-Acoustic Sensors

The acoustic-wave sensor creates a mechanical wave by applying an oscillating electric field that propagates through a piezoelectric substrate. The wave is altered according to the properties of its physical, chemical or biological environment, and then gets converted back into an electric charge, allowing for characterization of the alterations by electrical quantities measurable at the ports (*Fig. 16*) [70, 71]. Physical alterations, such as torque, or acceleration, directly influence the transducer substrate properties, whereas biological or chemical alterations, for example affinity reactions, or the adsorption of analyte molecules, typically require an analyte-specific recognition element coupled to the transducer.

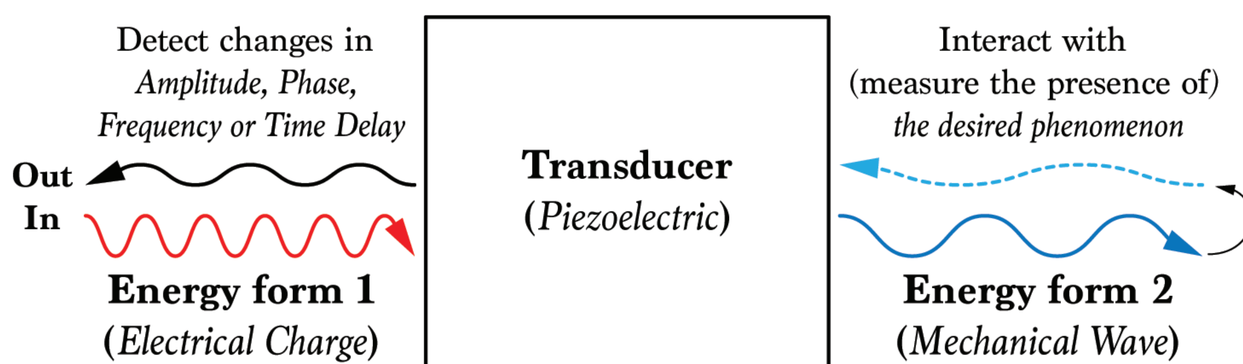

Figure 16. Schematic representation of a principle behind the self-generating (*active*) transducer- the piezoelectric sensor. An *active* sensor does not require an auxiliary energy source to operate.

The term "acoustic-wave sensor" can be used to describe a number of significantly different devices. Even though their operation principle relies on the same physical phenomena, fundamental mechanism of sensing might be very different [68]. Three classes of acoustic-wave sensors can be distinguished where:

1. the acoustic waves are used to define the domain of the measured quantity (accelerometers, microphones etc.);
2. the acoustic waves are being sent and received in order to sense the properties of surrounding medium and its discontinuities;
3. the acoustic and electro-acoustic field characteristics of the wave itself are used to measure properties of the surrounding medium. These can be used to sense wide range of physical quantities such as applied stress, force, pressure, temperature, density and viscosity, added surface mass, as they essentially behave like acoustic waveguides with a configurable responsivity.

For the majority of analytical applications in the life sciences, acoustic-wave sensors have to be immersed in aqueous liquids (buffer solutions) in order to deliver the analyte to the sensing surface. This results in a severe attenuation of the wave due to displacement components perpendicular to the surface when the SAW device utilizes the RSAW propagation mode [51, 68]. As a result, compression waves are generated, which radiate into the liquid and cause damping. Therefore, initially a lot of research activity on acoustic wave biosensors was focused on the use of other wave modes such as BAW operating in *thickness shear mode* (TSM). BAW devices typically consist of a piezoelectric material and two electrodes parallel to each other on each of its sides. The most commonly used BAW sensor is known, and well-established, as quartz crystal microbalance (QCM) (*Fig. 17a)* [72-75]. These devices rely on bulk crystalline substrates and typically operate in the range of 1 to 50 MHz. This frequency determines the maximum sensitivity of the sensor. This type of devices has an advantage that the signal electrode is located on the back side of the device away from the sensing front side, which is immersed into liquid. Thus, it is protected from the conductive effects of aqueous medium. However, it is known that at higher frequencies the mass sensitivity increases [76]. This is a limitation of a QCM approach as it requires further thinning of a substrate and as a result the device becomes too thin and fragile for the practical use. At the same time, device attenuation mechanisms become more dominant, as scattering factors become comparable in dimension to the acoustic wavelength. An increase in operational frequency, described by the relation between wave speed and wavelength as shown below, leads to an increase of scattering losses [77]:

$$f_0 = \frac{v}{\lambda} \tag{3.1}$$

where v is the wave speed in a piezoelectric material, λ is an acoustic wavelength, and f_0 is the resonance frequency of the device.

On the other hand, thinning the substrate will allow for the generation of acoustic waves with an additional shear propagation mode. Acoustic plate modes (APM) can be used to construct such a device [68]. APM implies that the acoustic energy is trapped by multiple reflections between the two surfaces of a substrate. Employing horizontal shear waves allows to reduce the device attenuation in water. Several APMs are usually excited simultaneously, while the frequency separation between them is often limited. This might result in a *mode hopping* i.e. shift of oscillation frequency from one mode to another. To overcome this limitation, much thinner Lamb wave devices (in the range of their acoustic wavelength) with symmetric acoustic modes can be used (*Fig. 17c)* [78, 79]. These devices will operate only at their main resonance frequency, allowing for precise measurements of mass loadings deposited on the surface [80-84]. Even though Lamb waves are surface excited, they travel through the bulk of a piezoelectric membrane, and both surfaces undergo displacement. The electrodes (IDTs) of the Lamb wave resonator are located only on one side of the membrane, and are therefore separated from the fluid medium, so that the effect of liquid conductivity or gas corrosion is minimized. Usually the Lamb wave velocity is lower than the compressional velocity of sound in liquids. As a result, the compression waves are not coupled in liquids, resulting in less attenuation of acoustic energy.

Thin-film bulk acoustic wave resonators (FBARs) (*Fig. 17b)* operate at a very high frequency (up to several GHz) and utilize thin piezoelectric films such as AlN squeezed between two electrodes [16, 85, 86]. FBARs are not only more sensitive than QCM, but also much smaller. The main difference between the FBAR and the QCM is that in case of the FBAR the piezoelectric substrate, deposited by a physical vapor deposition process, is much thinner than that of a bulk-cut piezoelectric crystal such in case of a QCM. However, the main disadvantage of these devices (as well as of a Lamb wave resonator) is their increased fabrication complexity.

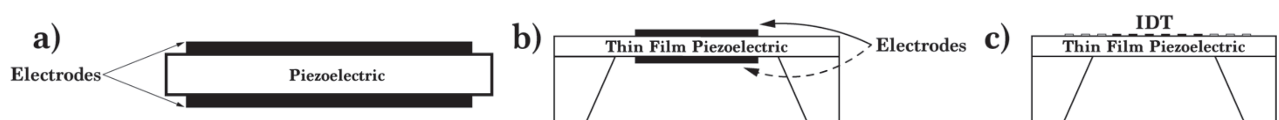

Figure 17. Various types of electro-acoustic devices used for mass sensing: **a)** QCM; **b)** FBAR; **c)** Lamb wave resonator.

3.1.2 Surface Acoustic Wave Sensors

Since around 1970, SAW-based components have been developed for various military applications (pulse compression radars, oscillators) and bandpass filters for regular TVs and radios. In 1979, the first article on a SAW-based gas sensor was published by Wohltjen and Dessy [87]. In the 1980s, the rise of mobile radio technologies resulted in a dramatic increase in demand for SAW devices and in particular SAW-based RF filters. As a result, the electro-acoustic device market has become one of the biggest and fastest-growing MEMS (micro electro mechanical systems) markets [34]. While being dominated mainly by filters, many other SAW-based devices have emerged in the past thirty years. These find their applications in measurements of various chemical and physical properties of an object under investigation, as well is in biosensing, and identification tags [88, 89]. SAW-based sensors are robust and compact, have high sensitivity and stability, while maintaining the manufacturing cost low. They provide fast real-time response and are generally compatible with the majority of CMOS and MEMS processes, which provide the ability to integrate read-out electronics or another microsystem directly into the device. Being a passive component (operates with any signal above the noise level, i.e., there is no threshold voltage), SAW devices can also operate wirelessly, enabling remote interrogation of a sensor in harsh environments.

SAW-based liquid sensors typically have a sensitivity higher than that of a QCM. This can be attributed to the fact that the sensitivity scales with frequency. When the SAW sensor utilizes Rayleigh waves for its operation, upon liquid contact it will experience strong attenuation of acoustic energy [90]. For that reason, SH-SAWs that are non-surface normal are often used (Love wave [91-94], leaky surface wave [95-97], etc.).

There are two common types of SAW device topologies being used for sensing. Both measure the variation of SAW propagation characteristics (velocity and attenuation) upon interaction with the analyte.

The first one includes SAW resonators (1- and 2-port configurations [88, 90, 95-98]). In resonant devices, one can measure the mass of an adsorbed analyte by monitoring the corresponding resonant frequency shift. The frequency shift of a SAW sensor can be described as follows [99]:

$$\Delta f = -k f_0^2 h \rho \tag{3.2}$$

where h and ρ are the thickness and density of the adsorbed layer, f_0 is the resonance frequency of the device, k is a constant related to the substrate and device properties.

The resonance frequency of a SAW resonant sensor has a linear relation to the mass loading:

$$\frac{\Delta f}{f_0} = -k\frac{h}{\lambda}\rho v \tag{3.3}$$

where $\frac{\Delta f}{f_0}$ is the relative frequency shift, $\frac{h}{\lambda}$ is the layer thickness to wavelength ratio and v is the velocity of the SAW. Here, the amplitude and phase characteristics are obtained from the dispersive reflection of the wave from metal strip gratings on both sides of the IDT.

In other kinds of measurements using surface acoustic waves, one can detect the time needed for the wave to travel from one IDT to another, using a delay line topology [100]. In wireless devices, the round-trip time is measured. The phase characteristic here is a linear function of frequency, meaning that the phase shift is constant in the specified frequency range. Upon application of heat, pressure, compression or stretching the substrate length and its elastic constants change. These changes lead to velocity, and thus to phase shift variations, which result in a proportional shift of resonant frequency, attenuation and time delay of the wave. Time delay τ of a SAW delay line topology is the ratio of acoustic length L and SAW velocity v. L is the distance between the outer electrode fingers of both receiving and emitting transducers. L and v are affected by temperature change, mechanical stress or a mass loading. The time delay can be described using:

$$\frac{d\tau}{\tau} = \left(\frac{1}{L}\frac{\partial L}{\partial y} - \frac{1}{v}\frac{\partial v}{\partial y}\right) dy = \gamma_y dy \tag{3.4}$$

where γ_y is the delay sensitivity with respect to y and depends on the piezoelectric substrate crystal properties. Disadvantages of SAW delay lines, when used as sensors, are their relatively large size needed for the generation of a specified time delay. This leads to large insertion losses associated with the attenuation of the wave travelling between the two IDTs, even without any perturbation in-between them. Electronic signal processing is required in order to read out the output signal from the delay-line sensor due to low level of acoustic response [92]. The poor response can be improved by changing the delay-line topology to a two-port resonant configuration [88, 95, 98]. With a careful selection of the wave propagation mode (choice of the substrate, metallization thickness/material, IDT and reflectors design) one can reduce losses to a minimum. Since the electrical signal is still supplied and received at two different ports, while the wave is travelling between the two transducers, integration and

miniaturization of the device is affected. On the other hand, one-port SAW resonators are small and offer some advantages over the two-port devices, namely reduced size and ease of integration, while maintaining low losses and strong resonance characteristics. However, the analyte in solution has to be deposited directly over the surface of the device and IDT in particular, resulting in damping [96, 97]. This disadvantage limits the use of one-port SAW resonators as a liquid-phase sensor.

3.1.3 Performance Characteristics of the Surface Acoustic Wave Resonator as a Sensor

This section describes some of the important parameters that define the performance of a sensor: *sensitivity* (**S**), *resolution* (**R**) and *limit of detection* (**LOD**).

All acoustic wave resonators are sensitive to various perturbations in their physical parameters, caused by different biasing conditions: mass loading, acceleration, ambient pressure, temperature drift, etc. When an acoustic wave resonator is used as a sensor, any perturbation along the path of the wave will result in a change of the resonance frequency Δf. This frequency change defines the sensitivity of a sensor [68]:

$$S = \frac{\Delta f}{\Delta M} \tag{3.5}$$

where M is any physical quantity being measured (mass, pressure, temperature), while ΔM is the measure of its variation. The sensitivity scales with frequency (*Eq. 3.5*). Often normalized expression for the sensitivity is used:

$$S_n = \frac{\Delta f}{f_0} \frac{1}{\Delta M} \tag{3.6}$$

Generally speaking, sensitivity of a sensor increases with frequency, which along with other benefits of frequency scaling (such as device size reduction) are of a high interest in the field of miniaturized analytical systems. However, operation at higher frequencies results in increased losses and hence in increased phase noise. As a result, only moderate increase of the overall resolution can be expected.

High performance sensing also requires high frequency stability. When sensor operates in oscillator configuration, frequency stability is affected by *temperature drift*, *long-term frequency drift* (or *aging*) and *short-term instability*. Sub-chapters below discuss the short-term frequency stability of an oscillator [101] and its effect on sensor performance (resolution and limit of detection), as well as the effect of temperature on device frequency.

Noise in Frequency and Time Domain

An ideal oscillator produces a sinusoidal wave at the output [102]. However, even devices with a high Q suffer from fluctuations in the amplitude and phase. To describe the instantaneous output voltage of an oscillator, a sinus function with modulated phase and amplitude can be used:

$$V(t) = [V_0 + a(t)] \sin(2\pi f_0 t + \varphi(t)) \tag{3.7}$$

where V_0 is the peak amplitude, f_0 is the central frequency, t is time, $a(t)$ and $\varphi(t)$ are the time-dependent random fluctuations in amplitude and phase, respectively. Since frequency is a time derivative of the phase, the term $\varphi(t)$ can be used to describe the random frequency or phase fluctuations. Then, the frequency at any given t can be expressed as following:

$$f(t) = f_0 + \Delta f(t) \tag{3.8}$$

where deviation from the central frequency is given by:

$$\Delta f(t) = \frac{1}{2\pi} \frac{\partial \varphi(t)}{\partial t} \tag{3.9}$$

Phase noise performance of an oscillator can be described in the *frequency* or *time* domain using various terms. In the frequency-domain, the *power spectral density* of the phase fluctuations $S\varphi(f_m)$ *or* the *single sideband* (SSB) phase noise density $\mathcal{L}(f_m)$ are used to measure the frequency instability. In the time-domain, the *Allan variance* $\sigma_y^2(\tau)$ or its square root *Allan deviation* $\sigma_y(\tau)$ are used.

In an ideal oscillator, the signal power spectral density (measured in Watts per 1 Hz of bandwidth) represents a single frequency spectral line. Furthermore, random fluctuation in phase noise result in continuous spectral sidebands above and below the nominal frequency f_0. These sidebands decay rapidly with increasing frequency offset f_m (*Fig. 18*):

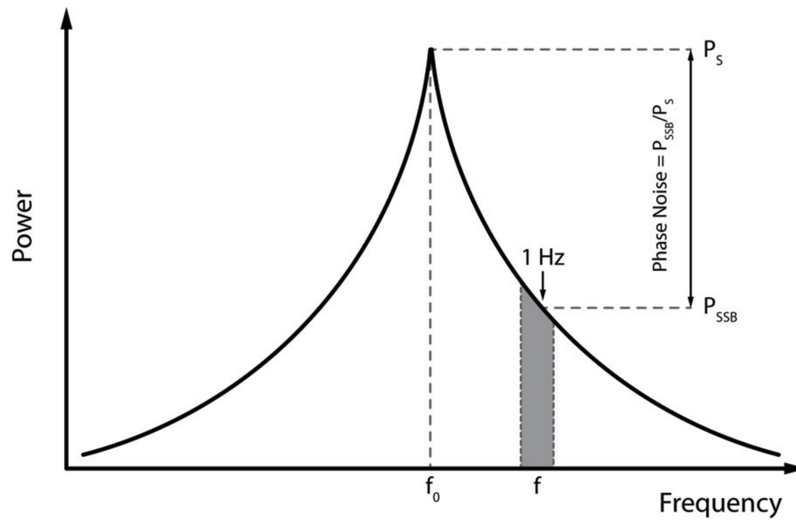

Figure 18. Spectral power distribution.

Single sideband noise density can be defined as the power spectral density measured above the nominal frequency. The SSB noise density $\mathcal{L}(f_m) = \frac{S\varphi(f_m)}{2}$ is measured in dBc/Hz (decibels below the carrier in 1 Hz bandwidth) and can be expressed as:

$$\mathcal{L}(f_m) = \frac{Power\ density\ in\ a\ single\ 1\ Hz\ sideband}{Total\ signal\ power}$$

All oscillator circuits consist of various passive and active components (e.g. resonators, amplifiers etc.) that contribute to the phase and frequency fluctuations. For that reason, the phase noise of the amplifier itself has to be considered. The spectral power density of the phase fluctuations $S\varphi(f_m)$ of an amplifier with a large enough offset f_m can be expressed as following:

$$S\varphi(f_m) = \frac{FkT}{P_s} \tag{3.10}$$

where F is thermal noise factor of the amplifier, k is Boltzman's constant, T is temperature in K and P_s is power of a signal. It is worth noting that the equation 3.10 does not depend on frequency. At $T = 290\ K$, $kT = 4 \cdot 10^{-21} J$, the above equation expressed in dB determines the *thermal noise floor* (*TNF*) of the amplifier [103]:

$$TNF = -174(dBm) + F(dB) - P_s \tag{3.11}$$

A power law can be used for describing the noise of an oscillator:

$$S\varphi(f_m) \propto f_m^{\alpha} \tag{3.12}$$

where $\alpha = -4, -3, -2, -1, 0$. The TNF corresponds to condition when $\alpha = 0$. Graphic representation of phase fluctuations versus frequency is shown in figure 19.

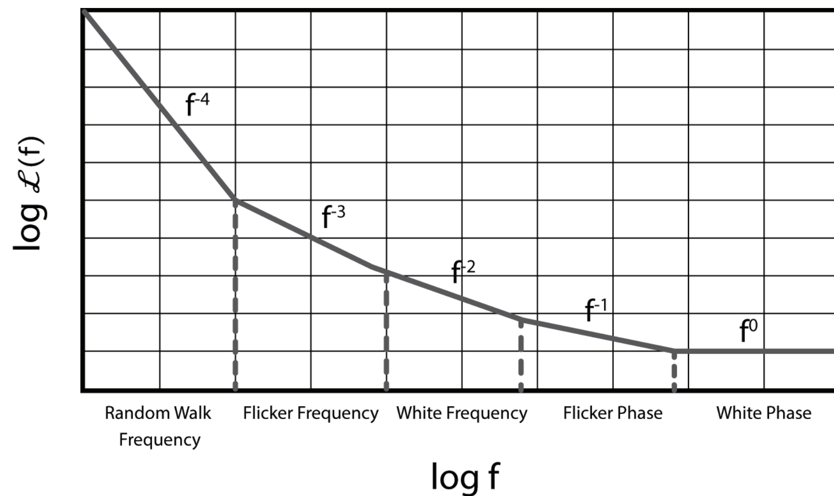

Figure 19. The spectral power density as a function of frequency offset.

According to Leeson, the SSB phase noise density $\mathcal{L}(f_m)$ of an oscillator can be defined as follows [104]:

$$\mathcal{L}(f_m) = 10\log\left[\frac{1}{2}\left(\left(\frac{f_0}{2Q_{lf_m}}\right)^2 + 1\right)\left(\frac{f_c}{f_m} + 1\right)\left(\frac{FkT}{P_s}\right)\right] \quad (3.13)$$

Equation 3.13 describes the distribution of noise power density away from the main signal (*Fig. 19*). Each term in the equation has its own origin. For example, *TNF* (*white phase noise)* exists mainly due to the presence of an amplifier (*Eq.* 3.10). One way to minimize this noise is to increase the signal power. The resonator itself contributes with *white* and *flicker frequency noise* terms. The effect of frequency fluctuations of a resonator can be minimized by increasing its *Q-factor*.

Allan Deviation

The standard for frequency stability definition in time domain is described statistically in terms of two-sample deviation also known as Allan deviation. The instantaneous fractional frequency deviation is defined as following:

$$y(t) = \frac{\Delta f(t)}{f_0} \quad (3.14)$$

Since measurement instruments do not provide instantaneous frequency values, but rather values averaged over time τ starting from t_i:

$$\overline{y_i(\tau)} = \frac{1}{\tau}\int_{t_i}^{t_i+\tau} y(t)dt \quad (3.15)$$

where τ is the averaging time and $i = 1, \dots, N$ is a set of N measurements (sampled values). Based on the definition derived by Allan [105], the IEEE has suggested a more standardized approach for measuring the Allan deviation [102]:

$$\sigma_y(\tau) = \sqrt{\frac{1}{2}\langle(\overline{y_{l+1}} - \overline{y_l})^2\rangle} \tag{3.16}$$

where $\langle(\overline{y_{l+1}} - \overline{y_l})^2\rangle$ denotes the infinite time averaging. However, in real world the infinite time averaging is not possible. For that reason, it is replaced with ordinary averaging over the number of measurements N:

$$\sigma_y(\tau) \cong \sqrt{\frac{1}{2(N-1)}\sum_{i=1}^{N-1}(\overline{y_{l+1}} - \overline{y_l})^2} \tag{3.17}$$

Phase noise in time domain can be also described as a power law:

$$\sigma_y(\tau) \propto \tau^{\beta} \tag{3.18}$$

where $\beta = -1, -\frac{1}{2}, 0, \frac{1}{2}$. Graphical representation of Allan deviation is a plot of $\sigma_y(\tau)$ as a function of the averaging time τ (*Fig. 20*):

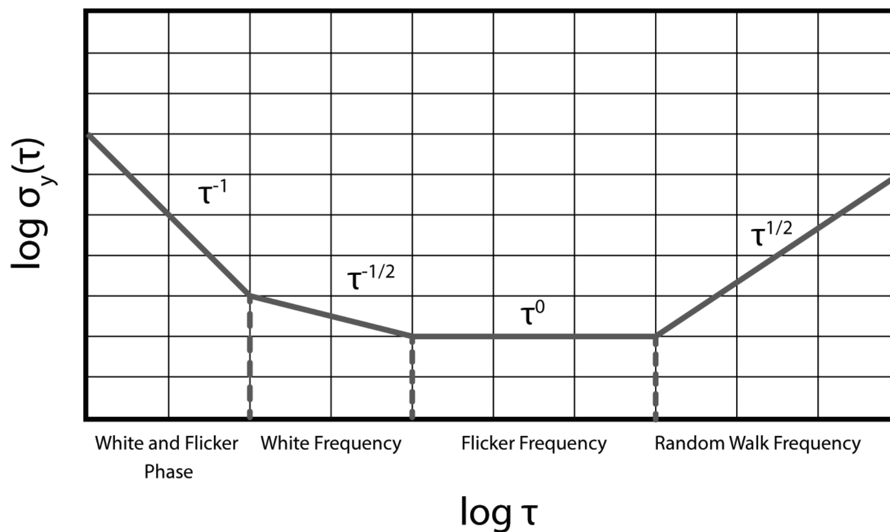

Figure 20. Allan deviation $\sigma_y(\tau)$ versus averaging time τ.

Below a certain minimum sampling interval, the noise level is independent of the averaging time. The smallest achievable value $\sigma_y(\tau)_{min}$ then has the same definition as a standard deviation σ_{std} and determines the noise floor of the oscillator. Typically, this sampling interval corresponds to averaging times between 0.1 s and 10 s and contains noise that cannot be eliminated by averaging. When the sampling time is increased above τ^0, the Allan deviation starts to increase as well, due to the random walk noise related to the environment around the oscillator (temperature, mechanical vibrations, etc.) More information about different phase noise sources can be found in [106].

Influence of Noise on Sensor Performance

Limit of detection is defined as a variation of normalized minimum detectable frequency Δf_{min} and expressed as 3 × *Allan deviation*:

$$\frac{\Delta f_{min}}{f_0} = 3\sigma_y(\tau)_{min} \tag{3.19}$$

Thus, the he smallest change in the input parameter ΔM that can be still resolved is the ratio between *LOD* and the *normalized sensitivity* (*Eq.* 3.6) [77]:

$$R = \frac{3\sigma_y(\tau)_{min}}{S_n} \tag{3.20}$$

The empirical relationship between the *smallest amount of noise* $\sigma_y(\tau)_{min}$ generated by an oscillator and the *quality factor* of a resonator is [107]:

$$\sigma_y(\tau)_{min} = \frac{10^{-7}}{Q} \tag{3.21}$$

The resolution increases as the quality factor of a resonator increases. The authors of the same article [107] also note that the maximum achievable *quality factor* is inversely

proportional to the frequency. For a given material, crystal cut, and mode of operation the following is valid:

$$Q_{max} \cdot f_0 = Const \tag{3.22}$$

Therefore, the minimum noise linearly increases with frequency:

$$\sigma_y(\tau)_{min} = Const \cdot f_0 \tag{3.23}$$

In practical measurements, it is important that the level of a useful signal is above the noise floor. One can describe such relation by the *signal-to-noise ratio* (SNR). SNR is a measure of the minimum amount of change in the measured physical quantity that can be detected in the output signal (change in frequency). The signal-to-noise ratio is determined by:

$$SNR = \frac{\Delta f}{\Delta f_{min}} = \frac{\Delta f}{f_0 3\sigma_y(\tau)_{min}} \propto \frac{\Delta f}{f_0^2} \tag{3.24}$$

where the *change in frequency* represents the signal, and the noise floor is determined by 3 × *Allan deviation*.

Equation 3.24 shows that sensor resolution deteriorates with frequency scaling as a linear function of absolute sensitivity versus frequency. In case of mass sensing, the SNR remains unaffected by frequency scaling effects, since the absolute sensitivity Δf scales with f_0^2 [108]. However, in viscosity sensing the absolute sensitivity scales with $f_0^{1.5}$ [73], which determines an inverse frequency scaling of the SNR as $f_0^{-0.5}$.

On the other hand, this simple model suggests that the frequency scaling itself can hardly bring any sufficient improvement in sensor performance. The benefits of frequency scaling are mostly related to the possibility of making a device smaller, which allows to integrate high-performance small form-factor devices into compact sensor arrays. Furthermore, there are device architectures that allow to improve the product $f \cdot Q$ and relative sensitivity with frequency scaling beyond the presented simplified model, owing to advances in engineering design and technology.

The design of high-resolution sensors is a tradeoff between sensitivity and noise levels. In this context, the *lateral energy confinement* reflector topology of a resonator proposed in

this thesis [Paper III] can offer significantly increased sensitivities as compared to the widely explored SAW approaches, while maintaining similar noise levels.

Thermal Stability

Variations in temperature of the environment, as well as operation at a high input power are affecting the device temperature. The frequency stability as a function of temperature is described in terms of the *temperature coefficient of frequency* (**TCF**). However, unlike the phase noise, which causes random fluctuations of frequency over time, the temperature variation causes a frequency drift, which is constant for a given crystal cut and technology. Temperature-stabilized resonators can be constructed when the TCF values are known. The dependence of the resonant frequency f_r on temperature can be represented as a power-law series of the temperature variation [73]:

$$\frac{f_r(T) - f_r(T_0)}{f_r(T_0)} = \sum_{n=1}^{3} TCF^n \cdot (T - T_0)^n \tag{3.25}$$

where T is the temperature variable, and T_0 is a reference temperature. TCF^n is the 1st, 2nd and 3rd order temperature coefficient of frequency:

$$TCF^n = \frac{1}{n!\, f_r(T_0)} \left(\frac{\partial^n f_r}{\partial T^n}\right)_{T=T_0} \tag{3.26}$$

The temperature drift of a resonator is related to changes in stiffness coefficients as a function of temperature, but also to the thermal expansion that affects both the dimensions of a resonator and the density of a material [109]. Most materials become “softer” upon exposure to elevated temperatures resulting in decrease of the acoustic wave velocity (*negative first order TCF*), while other become “stiffer” and the velocity increases with increasing the temperature (*positive first order TCF*).

There are some practical solutions to the issues related to temperature drift. Temperature-compensated devices can be constructed either by using material crystal cuts with zero first order TCF (e.g. ST-cut quartz,), or by combining materials with TCF opposite in sign (e.g. $LiNbO_3$ has a negative TCF, while SiO_2 positive) [110]. Novel heteroacoustic layer

substrates are also promising candidates for the construction of high-performance zero TCF resonators [12].

3.2 Electrical and Electrochemical Methods

Electrochemical detection methods aim to study reactions taking place at the interface of a solid conductor and an electrolyte and relate observed processes and changes quantitatively.

Impedance spectroscopy (IS), or electrochemical impedance spectroscopy (EIS), is a technique that aims to characterize systems based on their dielectric properties. It is a powerful tool for analyzing the electrical impedance of a system by detecting changes at its surface or in the bulk. The term "spectroscopy" refers to the fact that the impedance is determined at different frequencies rather than just one. It has been used extensively in studies of corrosion mechanisms [111, 112], various membranes transport properties [113], battery optimization [114, 115] and others. In terms of biosensing, it is particularly suitable for the detection of binding events at the surface of the transducer, as well as to characterize the modification of the surface with biorecognition elements themselves [116, 117]. Impedance spectroscopy does not require modification of biomolecules with fluorescent dyes, enzymes, redox or radioactive labels, essentially making this technique label-free. For example, if cells adhere and proliferate on the electrode, its effective surface area is reduced resulting in an increased impedance. This is often referred to as impedance sensing. It can be used to monitor cell concentration, growth, and their physiological state; or more generally for investigations of their number, viability and various metabolic activities [118]. A cell can be modelled as an electrical circuit (equivalent electrical circuit), due to the fact that cell membrane is relatively electrically insulating, while the cell interior usually maintains reasonable ion concentrations, allowing for conductivity and permittivity measurements. These electrical properties depend on the actual physiological state of a cell, i.e., each cell element such as cytoplasm, membrane, medium surrounding it, so it will act as a resistor or a capacitor with values depending on various factors. The equivalent electrical circuit can be used to curve fit the data obtained experimentally to explain the characteristics of the impedance detection system.

In the majority of EIS experiments, a fixed sinusoidal AC voltage is applied by a potentiostat across cell containing multiple electrodes in a solution of electrolyte. These electrodes act as a signaling element and a recording interface at the same time. The AC voltage $V(t)$ is a function of time and frequency and can be mathematically expressed in the trigonometric form:

$$V(t) = V_0 \cdot \sin(\omega t) \tag{3.27}$$

where t is the time, V_0 is the voltage amplitude, $\omega = 2\pi f$ is the angular frequency, and f is the AC frequency of the excitation signal. The resulting current has a sinusoidal form of the same frequency as the excitation voltage (*Fig. 21*):

$$I(t) = I_0 \cdot \sin(\omega t + \varphi) \tag{3.28}$$

where $\varphi = \varphi_V - \varphi_I$ is the phase shift, I_0 is the response signal amplitude.

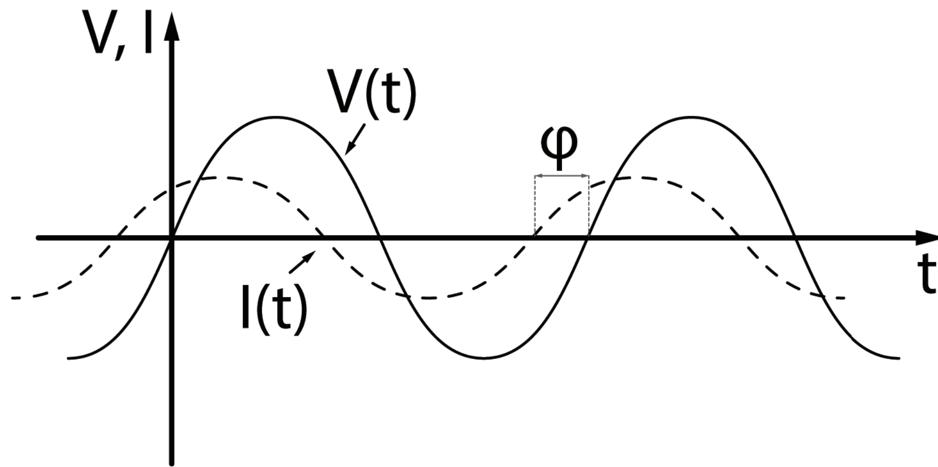

Figure 21. A sinusoidal excitation potential and its current response in an AC system.

Analogous to Ohm‘s law, impedance is described as the ratio of the complex voltage (*Eq.* 3.27) and the complex current (*Eq.* 3.28):

$$Z = \frac{V(t)}{I(t)} = \frac{V_0 \cdot \sin(\omega t)}{I_0 \cdot \sin(\omega t + \varphi)} = Z_0 \cdot \frac{\sin(\omega t)}{\sin(\omega t + \varphi)} \tag{3.29}$$

where Z_0 or $|Z|$ is the magnitude of impedance.

Like resistance, it describes the opposition of an object to the flow of electric current. Technically, the resistance is the impedance with zero phase angle, which obeys Ohm’s law

and describes DC circuits, since the current is not alternating. In AC circuits, the phase angle is not equal to zero, as capacitive and/or inductive effects are present at almost all frequencies. According to Euler's relationship:

$$e^{j\varphi} = \cos\varphi + j\sin\varphi \tag{3.30}$$

Equation 3.30 allows to express impedance (*Eq.* 3.29) as a complex function:

$$Z = \frac{V_0 \cdot e^{j\omega t}}{I_0 \cdot e^{j(\omega t - \varphi)}} = Z_0 e^{j\varphi} = Z_0(\cos\varphi + j\sin\varphi) \tag{3.31}$$

The expression above has real and imaginary parts:

$$Z_{Re} = Z_0 \cos\varphi \tag{3.32}$$

and

$$Z_{Im} = Z_0 \sin\varphi \tag{3.33}$$

All frequency-independent resistances in the electrical circuit are in the real part of the impedance and behave as an ideal resistor *R*. The real part represents energy losses in the system. The imaginary part of the impedance is expressed by the reactance *X* and contains capacitive and inductive components of the electrical circuit. These components are frequency dependent and influence the permeability of the current. The imaginary part represents energy stored within the system (*Fig. 22*).

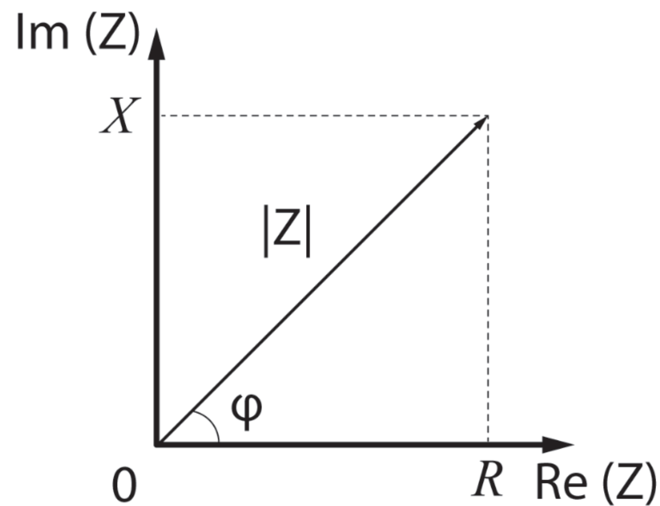

Figure 22. A graphical representation of the complex impedance plane.

Thus, real and imaginary parts can be converted to magnitude and phase:

$$|Z| = \sqrt{{Z_{Re}}^2 + {Z_{Im}}^2} = \sqrt{R^2 + X^2} \tag{3.34}$$

and

$$\varphi = \tan^{-1}\frac{Z_{Im}}{Z_{Re}} = \tan^{-1}\frac{X}{R} \tag{3.35}$$

In the Bode-plot, $|Z|$ and φ are displayed as functions of frequency (*Fig. 23b*), while in the Nyquist diagram the imaginary part is plotted as a function of the real part (*Fig. 23a*).

3.2.1 Equivalent Circuit Modelling

The current flow in an AC circuit is determined by three basic passive circuit components: ideal (Ohm's) resistor, capacitor and inductor. Let's first consider an electrical circuit consisting only of an ideal resistor and free of any capacitive or inductive influences. When a sine wave voltage is applied across an ideal resistor, the resulting current is also a sine

wave in phase with the voltage ($\varphi = 0°$) and no time lag. Thus, the impedance is resistive and has no imaginary component at all AC frequencies (on a Bode magnitude plot it is just a horizontal straight line (slope equals 0):

$$Z_R = Z_{Re} + jZ_{Im} = R + j0 = R \tag{3.36}$$

Another common element in an AC circuit is the capacitor. When a sine-wave voltage is applied to an ideal capacitor, the output is a cosine-wave current that is -90° out-of-phase with the voltage. For a capacitor, the current is proportional to the voltage change over time:

$$I(t) = \frac{dQ(t)}{dt} = C\frac{dV(t)}{dt} = -\omega \cdot C \cdot V(t) \tag{3.37}$$

where $Q(t)$ is the rate of flow of a charge and C is the capacitance. By introducing equation 3.37 into equation 3.29:

$$Z_C = Z_{Re} + jZ_{Im} = 0 + jX = j\left[-\frac{1}{\omega C}\right] = \frac{1}{j\omega C} \tag{3.38}$$

The impedance of a capacitor varies with the inverse of the frequency. Ideal capacitors only have an imaginary component, without any resistance contribution to the impedance. Because of that, the Bode magnitude plot for a pure capacitor is s a straight line along the negative reactance-axis with a slope of -1, and the Bode phase-angle plot is a horizontal line at -90°.

The third basic passive element in AC circuits is an inductor. However, it plays a minor role in equivalent circuits used for describing the electrical properties of biological systems and will not be considered further.

In real EIS studies, non-ideal circuit elements are often required to model the impedance characteristics of a system due to the dielectric inhomogeneities of an analyte or roughness of electrodes. A *constant phase element* (CPE) can be used for that purpose. Despite the fact that CPE is not a resistor, capacitor or inductor, it can sometimes be viewed as a non-ideal capacitor (e.g. when used to model double layers that show non-ideal capacitive behavior). The empirical contribution of the CPE to the impedance is given by:

$$Z_{CPE} = \frac{1}{A \cdot (j\omega)^n} \tag{3.39}$$

where A and $n = [0,1]$ are frequency independent parameters. When the exponent n is equal to 1, the CPE is a perfect capacitor. When it is equal to 0, the CPE is an ideal resistor. For any given value of $= [0,1]$, the CPE exhibits mixed electrical properties of a resistor and a capacitor with dominating capacitance for $n > 0.5$ and dominating resistance for $n < 0.5$. When $n = 0.5$, CPE becomes a Warburg element and accounts for current flow limited by the ionic diffusion. The Warburg element produces a distinctive 45° tail in the low-frequency region of the Nyquist plot. The phase angle o f a CPE is constant, and is given by:

$$\varphi = -n\frac{\pi}{2} \tag{3.40}$$

In real systems containing an imperfect layer of material, typical values for n are usually between 0.5 and 1.

Each biological system can be represented by an *equivalent electrical circuit model* by simply treating it as a combination of individual electrical components with defined impedances. Once an adequate equivalent circuit is created, the total theoretical impedance of the model is expressed mathematically with a transfer function by integrating the impedance contributions of all individual circuit elements. Following that, the impedance data obtained experimentally is fitted with the transfer function to deduce the parameters of all individual circuit elements. The electrical response of each element is then correlated with specific physical/chemical properties or phenomena of a structural component of the system under investigation.

Complexity and inhomogeneity of biological systems makes them difficult to be accurately represent with an electrical model that accounts for the electrical properties of a sample in all detail. Therefore, simplified equivalent electrical circuits for each individual case have to be designed that are specific towards the information one wants to obtain. For example, the complex electrode-electrolyte interface can be represented by a very simple electrical model: the combination of a resistor and a capacitor in series, while the impedance of a cell membrane can be modelled by the same two circuit elements, but connected in parallel (*Fig. 23a*).

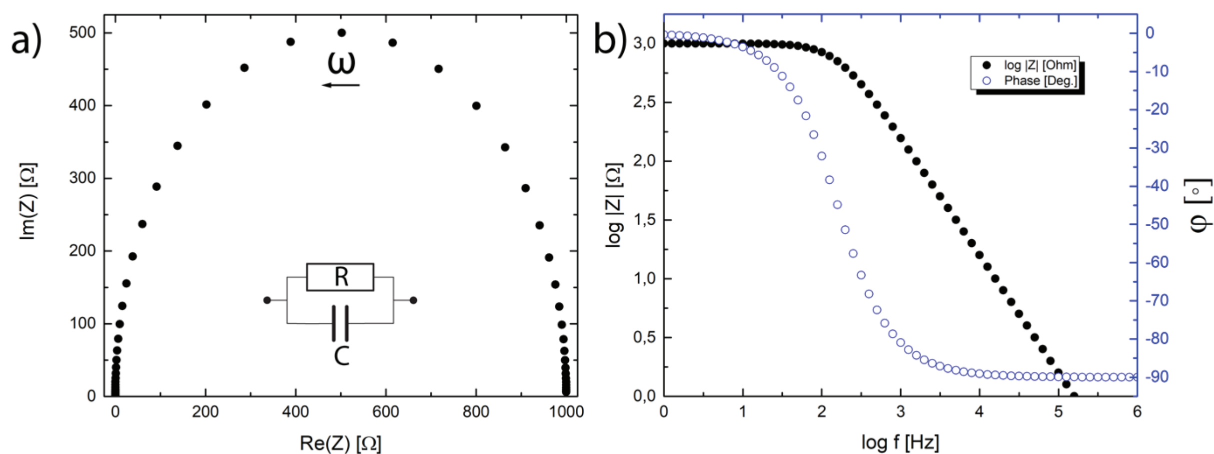

Figure 23. An impedance response of a simple RC circuit (R=1kΩ, C=1μF, frequency range from 1 Hz to 1 MHz) on the **a)** Nyquist diagram; **b)** Bode plot.

3.3 Optical Detection Methods

The assay used in this thesis for characterizing the sensor was validated by means of an optical technique, employing the absorption and re-emission of visible light under a microscope (fluorescence microscopy).

Interactions between light and matter can be evaluated by optical spectroscopy, an analytical technique where changes of the wavelength and intensity of electromagnetic radiation of a certain incident wavelength and intensity can be measured and quantified [119]. Electromagnetic (EM) radiation interacting with matter can get *absorbed* (e.g. UV/Vis absorption spectroscopy, IR and Raman spectroscopy), *emitted* (e.g. fluorescence, chemiluminescence, phosphorescence etc.), *scattered (photon correlation spectroscopy),* or *induce chemical changes* (photochemistry). The precise mode of interaction mainly depends on the energy of EM radiation (gamma-rays, x-rays, ultraviolet, visible, infrared, microwave and radio).

The use of optical spectroscopy for detection and quantification of surface immobilized biological objects is not always an optimal solution in the context of miniaturized integrated devices. This is due to the dependency on a stable light path, lensing, filtering, and focusing mechanisms that are necessary for implementation of optical detector resulting in extra cost and complexity. Additionally, optical detection typically requires focused radiation, leading to a limited detection area available per measurement; moderate selectivity often requires separation, or labeling, before the measurement.

Absorption spectroscopy is one of the most common techniques, as many materials absorb *electromagnetic* (EM) radiation in the UV and visible range, where probe light can be generated and detected easily. Absorption of a photon changes the energy of a molecule from a ground to an excited state. As a result, a molecule can emit light at a different wavelength in order to decrease the energy of the system. The total energy of a molecule is the sum of electronic, vibrational, spin orientation and translational energies. The exact absorption and deactivation mechanisms differ in each case. However, it always involves the absorption of a certain amount of energy. For example, valence electrons are excited in UV/Vis spectroscopy; in x-ray spectroscopy, more energetic x-rays excite core electrons; gamma-rays that are used in Mössbauer spectroscopy induce nuclear transitions. At lower energies, radio frequencies (RF) operating in MHz range are used to change the nuclear spin in nuclear magnetic resonance (NMR), microwaves (GHz range) are used in electron spin resonance (ESR) and involve electron spin, while in microwave spectroscopy the molecular rotations are probed. Infrared radiation (THz domain) excites molecular vibrations in IR and Raman spectroscopies.

3.3.1 Fluorescence Microscopy

Light microscopes have a great advantage of being fast, non-destructive, and *in-situ* (being able to perform the experiment on a sample while it is still located in its native environment). Typically, samples that are being analyzed do not have to be modified (e.g. coated with a conductor as in case of *scanning electron microscopy*. On the other hand, optical microscopes have a diffraction limited resolution, suffer from shadowing effects, interference, secondary reflections, lens distortions, and others.

In the life sciences, *fluorescence* microscopy is one of the most important analytical techniques. It is based on *luminescence* (both phosphoresce and fluorescence), arising from either naturally luminescent specimen, or from samples specifically tagged with an appropriate dye molecule. The samples are labeled with dyes that emit light in the visible range of the EM spectrum when exposed to the shorter-wavelength *ultraviolet* (UV) or visible radiation (*Stokes' shift*). The fluorescence microscope magnifies labeled regions, while at the same time providing excitation light, and separating it from the light emitted by the targeted species, using special filters and a dichroic mirror. This mirror is responsible for reflecting light shorter than the specified wavelength, while allowing the light with a longer wavelength to pass. Thus, the observer sees only the light emitted from the fluorescent dye, rather than the scattered excitation light. Intensity of the emitted light is typically measured with an electronic sensor, e.g. photomultiplier or a CCD camera. In order to prevent *photobleaching* of the fluorophore label, one has to carefully choose the excitation light intensity and duration, and exclude or remove oxygen from the sample.

4 Surface Acoustic Wave Resonance (SAR) Liquid-phase Sensor

4.1 The SAR Concept

A main requirement for an acoustic in-liquid gravimetric sensor operation is to retain its functionality when immersed in aqueous solution. This limits the choice of waves to modes with shear transverse polarization [51]. Additionally, there is a desire to reduce the sensor size so that the small form-factor sensor array integration becomes possible. Reduction in size allows to reduce the amount of sample needed, along with improved diffusion-limited mixing times. SH-SAW devices have been explored as a high frequency alternative to QCM sensors [120]. SH-SAW technology relies on simple, planar large-scale fabrication methods well-established by the fast-growing RF filter industry, along with the straightforward integration with microfluidic systems. The majority of SH-SAW liquid-phase sensors utilize Love wave [121] and leaky wave (LSAW) propagation modes. In these modes, the waves are strongly confined to the surface resulting in an enhanced sensitivity towards mass deposited over the surface, along with changes in viscosity, viscoelasticity and dielectric permittivity in the vicinity of the latter. Conventionally, SH-SAW sensors are constructed using a delay-line configuration where the time delay and phase shift of a wave propagating through a comparatively long distance are determined [122]. When used for in-liquid sensing, the signal loss resulting from the significant SH-SAW damping prevents the construction of efficient SAW biosensors. A two-port SAW resonator with significantly smaller distance in-between the two transducers can be employed as an alternative to the delay line topology. The frequency of the transmission resonance for such sensor was found to be sensitive to the absorption of proteins on the sensor surface entirely immersed in liquid [123]. The performance of the device in this approach is seriously affected by the liquid conductivity that short-circuits the SAW transducers in addition to large transmission losses. The liquid can be confined in the sensing area by integration with a soft polymer *polydimethylsiloxane* (PDMS) microchannel system at the expense of additional damping losses [92]. In practical measurements, the two-port configuration is not robust enough, compared with one-port QCM and FBAR devices.

This thesis describes a novel microfluidics-integrated high frequency sensor concept for liquid-phase sensing, combining the advantages of the one-port measurement setup with commercially viable fabrication process and materials [**Paper II**]. The reflective gratings of a one-port SAW resonator are used as sensing elements, while the wideband IDT is placed in-

between the reflectors and protected from the liquid, providing low susceptibility to damping, control over the device impedance and simplified measurement setup (*Fig. 24)* [124]. The frequency shifts in the proposed topology are due to the change in SAW propagation characteristics (phase velocity and reflectivity) under the reflective gratings exposed to a mass or electrical load. The chosen piezoelectric substrate is a Y-cut $LiNbO_3$ crystal. This crystal cut produces a *leaky* SAW (**LSAW**), propagating along the X-axis of the substrate with very strong electromechanical coupling of about 25% [32]. As a result, low impedance electro-acoustic sensors sustainable to viscous loadings can be constructed as most of the electric energy is converted into a LSAW. Moreover, a low diffracting Rayleigh SAW exists along the Z-axis of the Y-cut $LiNbO_3$ substrate. It can be used for rapid-mixing of diffusion-limited laminar streams that are present inside the microfluidic system through the integration with RSAW-generating IDTs [125]. Thus, the chosen substrate crystal cut provides a possibility for integrating liquid-phase sensors with microfluidic mixers on the same chip.

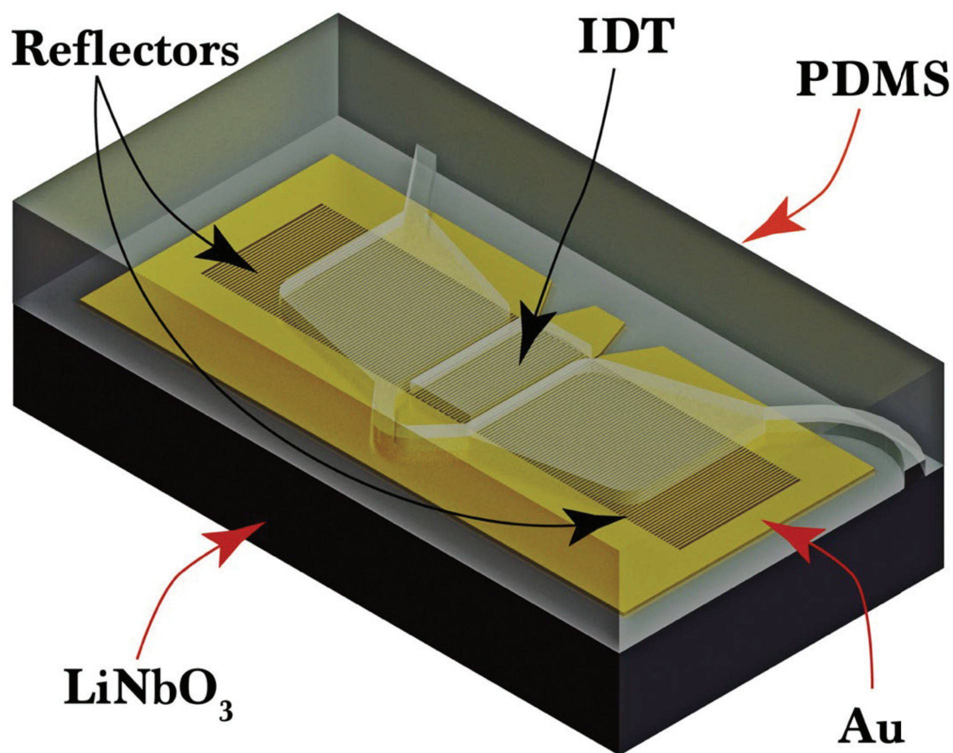

Figure 24. 3D representation of a one-port surface acoustic resonance (SAR) microfluidics-integrated liquid-phase sensor [126].

The LSAW suffers from significant bulk scattering losses, implying that it is not well-guided, and radiates into the crystal bulk. Thus, the acoustic energy at the surface decreases, leading to the reduced sensitivity. This issue can be addressed by utilizing *Au* periodic strip

gratings that, on one hand, slow down the LSAW and convert it in to a surface-guided SH-SAW, while on the other hand efficiently reflect it [34]. To evaluate and optimize the performance of a device before actual prototyping, and to get a better understanding of the fundamental mechanisms that are hard to measure directly *finite element modelling* (FEM) simulations were performed using the COMSOL Multiphysics® software package [**Papers II-III**]. Figure 25 shows eigenfrequency FEM analysis of the primitive SAW cell comprising a Y-cut $LiNbO_3$ substrate with a free surface (**a**) and with a periodic Au grating (**b**), respectively. The primitive SAW cell is a single wavelength (λ) cell with periodic boundary conditions applied to the side walls. A perfectly matched layer at the bottom is introduced for capturing losses, related to bulk wave radiation. The strips have a pitch d = 10 µm, corresponding to an acoustic wavelength λ = 20 µm. The resulting resonance frequency f_r is ~185 MHz. The Au thickness was set to h = 270 nm, and the Au strip width-to-pitch metallization ratio to m = 0.5. The strong waveguiding effect of the Au strip grating is apparent at the resonance frequency of the SH-SAW under the Au grating (*Fig. 25*__b__).

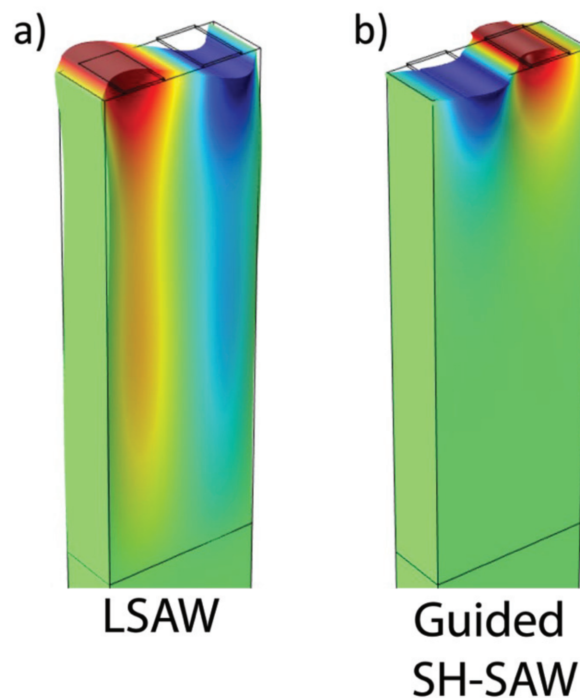

Figure 25. FEM simulations of the shear displacements. **a)** LSAW on a free surface; **b)** SH-SAW on a surface guided by a periodic Au grating. The magnitude of the shear displacement amplitude is color-coded in shades of blue (negative) and red (positive). Dark colors represent larger displacements, bright colors represent smaller displacements [124].

Subsequently, the SH-SAW displacement was simulated in water. Figure 26 shows the SH-SAW confinement near the substrate surface, where it is decaying completely in to the liquid at about 200 nm from the surface. The characteristic decay length δ is about 40 nm.

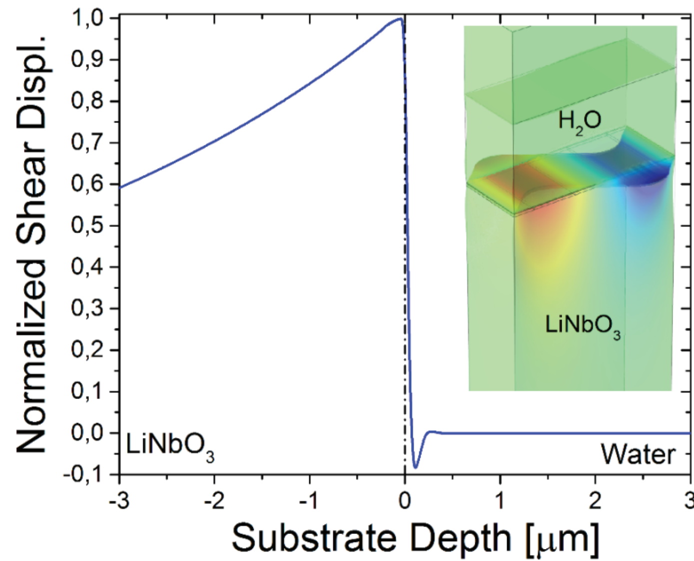

Figure 26. FEM simulations of the SH-SAW displacement in liquid. The displacement profile is plotted together with the 3D representation of the displacement confinement (inset). Values of substrate depth are negative for $LiNbO_3$ and positive for H_2O [124].

The simulated sensitivity of the lower edge of the SH-SAW frequency stopband for typical bias loads in liquids is shown in table I:

SAW velocity shift [ppm]	Bias
-2090	air to water loading
-1030	short circuiting the entire surface
+85	per 10ε_0 down-shift in permittivity
-120	per 10% increase in liquid density
-290	per two-fold increase in liquid viscosity

Table I. SH-SAW sensitivity in water solutions.

Figure 27 shows a sketch view of the SAR sensor concept overlaid with the FEM-simulated displacement amplitudes of the SH-SAW resonator at resonance frequency. The PDMS layer containing microfluidic channels is aligned in such a way that the containers overlap with the reflective gratings, while the IDT is protected by the air cavity. The SH-SAW transducer is a wideband IDT, formed by 21 Au strips. Adjacent to the IDT, two reflector gratings are placed, each having 69 Au strips, from which 49 are overlapping with a microfluidic container, and the device aperture is $40 * d$. In this configuration, the wideband IDT is emitting SH-SAW energy towards the reflectors, where the SH-SAW is gradually reflected back to the IDT. Thus, a mass loading on the reflectors induces a shift in the resonance frequency determined by the change in SAW velocity, as well as in SAW reflectivity from the strips of the periodic gratings. Both the IDT and the reflective gratings consist of a 300 nm thick Au-based metal stack.

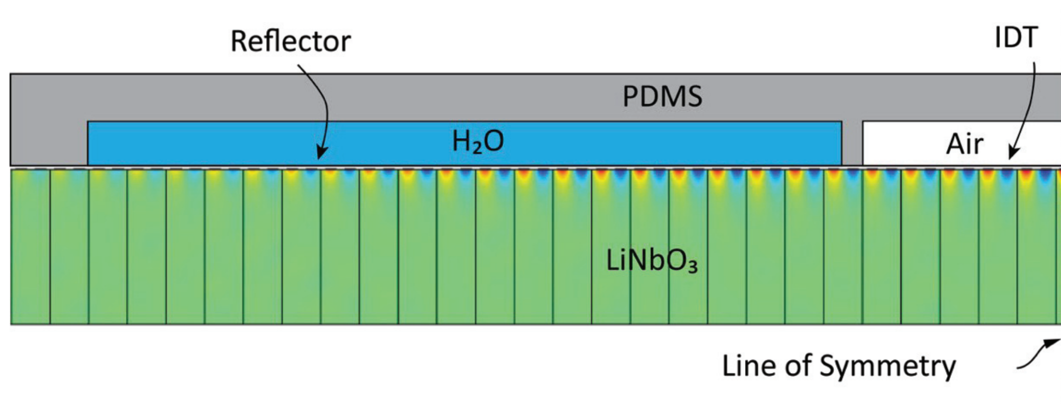

Figure 27. Sketch view of one-half of the SAR sensor cross-section overlaid with the FEM simulated displacement magnitude determined from a frequency response of the SH-SAW resonator at resonance frequency. Color code: amplitude: dark blue (negative) to red (positive) [124].

4.2 Resonator Optimization

To identify resonator designs [127] with minimum spurious responses and clear resonances, four different designs were investigated by integrating the sensor with a PDMS microfluidic system [**Paper I**]. The designs were (*Fig. 28*):

1. **Regular design**. A SAW resonator where the reflective gratings are synchronously placed around the IDT;
2. **Piston-mode design** [128-130]. A synchronous SAW resonator with design suppressing the transverse modes in the structure;

3. A synchronous SAW resonator with IDT **apodization** [131];
4. **Hiccup design** [132, 133]. The center of the IDT has -*d*/10 break in its periodicity.

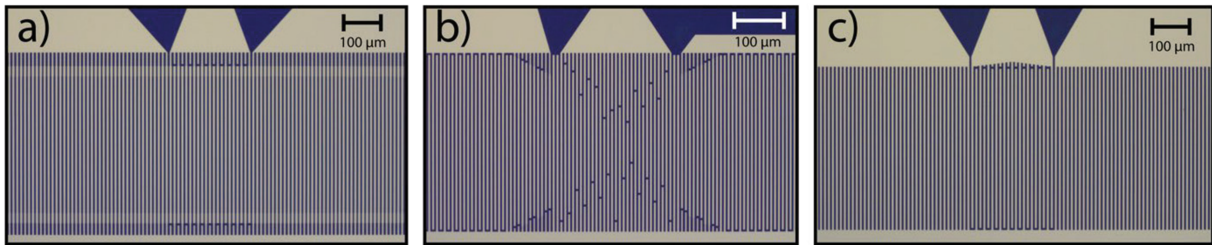

Figure 28. Inspection microscope image of the fabricated **a)** *piston*-mode design SAR device; **b)** SAR device with *apodized* IDT; **c)** *hiccup* design SAR device. The *regular* design resonator looks like the *hiccup* resonator but without break in periodicity of its IDT [126].

Initially, the SAW resonators were characterized in air (*Fig. 29a*). All of them have demonstrated a quality factor *Q* of ~1000. The *regular* design expectedly exhibited few transversal modes near the resonance. The *piston* mode design has led to effective suppression of these transversal modes. The *hiccup* and *apodized* designs show responses with significantly suppressed side-lobes as compared to synchronous designs.

When a thick PDMS layer is placed and bonded over the SAW resonators, all of them have exhibited performance degradation due to damping (*Fig. 29b*). Still, the device performance was retained, since SH-SAWs are sufficiently sustainable in the viscoelastic PDMS material. All devices demonstrated a *Q* of ~60, and 20 – 30 Ω impedance at resonance. All spurious resonances have been sufficiently suppressed by the damping.

When a PDMS layer with microfluidic cavities, but *without* air cavity above the IDT, was bonded over the SAW resonator, unwanted concurrent ripples near the main resonance appeared for both the *regular* and the *piston*-mode designs (*Fig. 29c*).

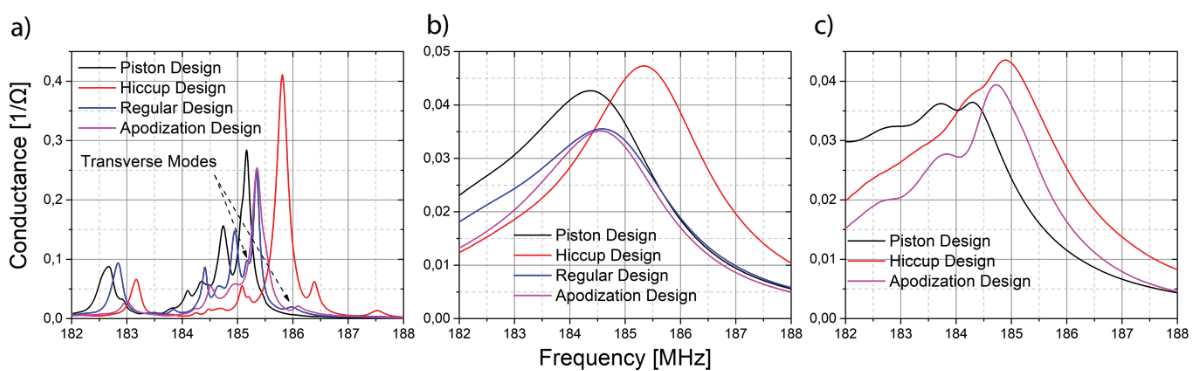

Figure 29. Close-in resonance conductance of the SAW resonators **a)** in air; **b)** bonded with 1 cm thick PDMS

piece; **c)** bonded to the PDMS sample delivery system consisting of two microfluidic containers overlapping with the SAW reflectors [126].

By measuring the scattering parameters of the device with water-loaded microfluidic containers, two designs that can tolerate the spurious content introduced by the microfluidic system and the presence of liquid were identified: with *hiccup* and *apodized* IDTs [**Paper I**]. The presence of liquid in the containers led to a split resonance performance of the *regular* and *piston*-mode resonator designs, which makes these types of suppression approaches unpractical for sensing applications. Additionally, this design iteration pointed out that *hiccup* resonators can tolerate the spurious content introduced by the microfluidic system better than resonators with other designs. Thus, subsequent SAR sensor devices utilize *hiccup* resonators along *with* an air cavity above the IDT (*Fig. 30*).

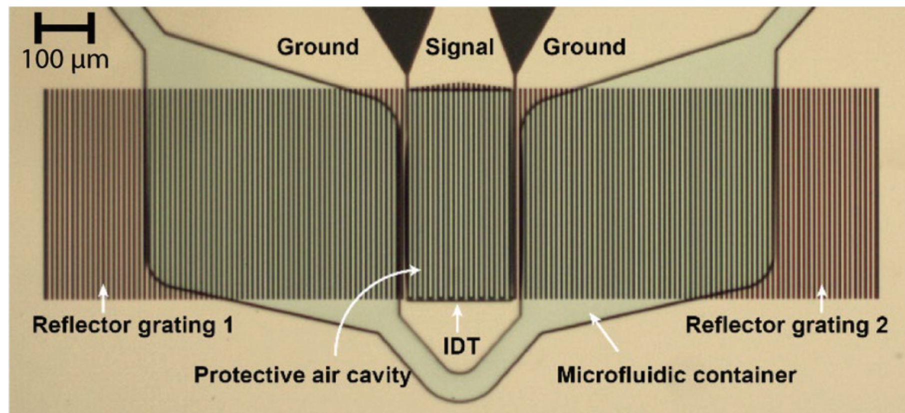

Figure 30. Optical microscopy image (top view) of the assembled microfluidic SAR device. SAR sensor consists of a SAW resonator with *hiccup* design, bonded to a PDMS sample delivery system, consisting of two microfluidic containers and a protective air cavity above the IDT [124].

Frequency shifts of the conductance peak and the zero of the admittance phase of about -915 ppm were observed as a result of water loading into the SAR sensor. Additionally, a -5% decrease of the conductance peak magnitude was measured (*Fig. 31)*. The device quality factor decreased from 300 to 250 under water loading. The phase of admittance demonstrated sufficient linearity in the vicinity of its zero point. The measured conductance is about 0.125 Ω^{-1}, thus determining a low sensor impedance of about 8 Ω at resonance. This allows for a sensor design with a further reduced number of strips in the IDT be used, while keeping the impedance at resonance close to 50 Ω.

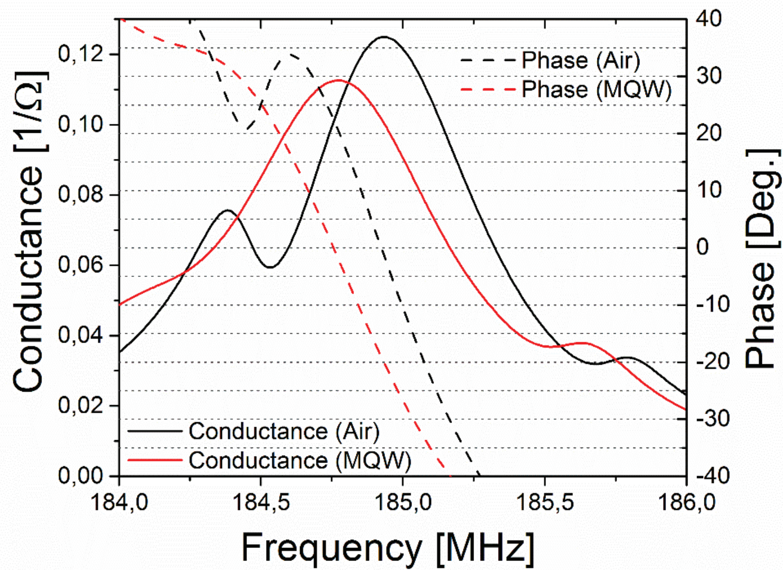

Figure 31. Close-in resonance conductance of the fabricated SAR sensors. The black curve represents the measurement in air-filled, and the red curve in water-filled microfluidic containers. MQW refers to Milli-Q-purified water [126].

For comparison, a two-port SAW resonator (*Fig. 32*), simultaneously fabricated on the same wafer with the same periodic strip gratings, was also characterized in air and water. A frequency shift of the S_{21} phase of −1450 ppm was measured upon water loading. The minimum insertion loss was more than −20 dB. Thus, the SAR sensor reached in this very first iteration about 63% of the sensitivity of the conventional delay line. However, an improvement is feasible through design modifications to promote confinement of a larger portion of the SH-SAW energy in the reflectors.

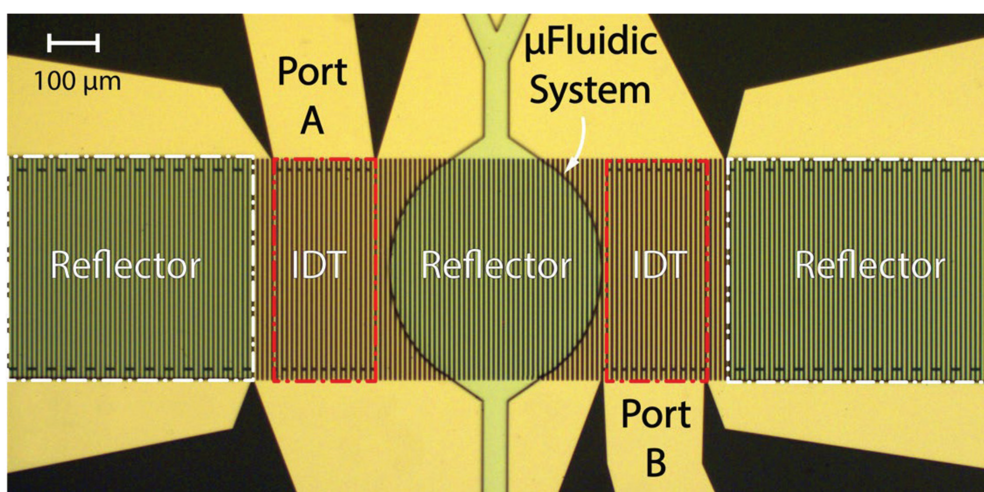

Figure 32. Optical microscopy image (top view) of the assembled microfluidic two-port SAW sensor device. The sensor consists of a two-port SAW resonator with *regular* design, bonded to a PDMS sample delivery system, comprising a microfluidic container located in-between the two IDTs.

In the original SAR sensor design described above [**Paper II**], the SAW energy is being gradually reflected back to the IDT, thus promoting strong SAW energy localization under the IDT, while outside the transducer the SAW displacement is decaying exponentially (*Fig. 33)*. This effect itself is limiting the device sensitivity, since it is determined by the ratio between the kinetic energy at the sensing surface and the total kinetic energy in the system [68]. Typically, an improvement in SAW sensitivity results from better confinement of SAW energy near the surface, achieved through slowing down the wave [32].

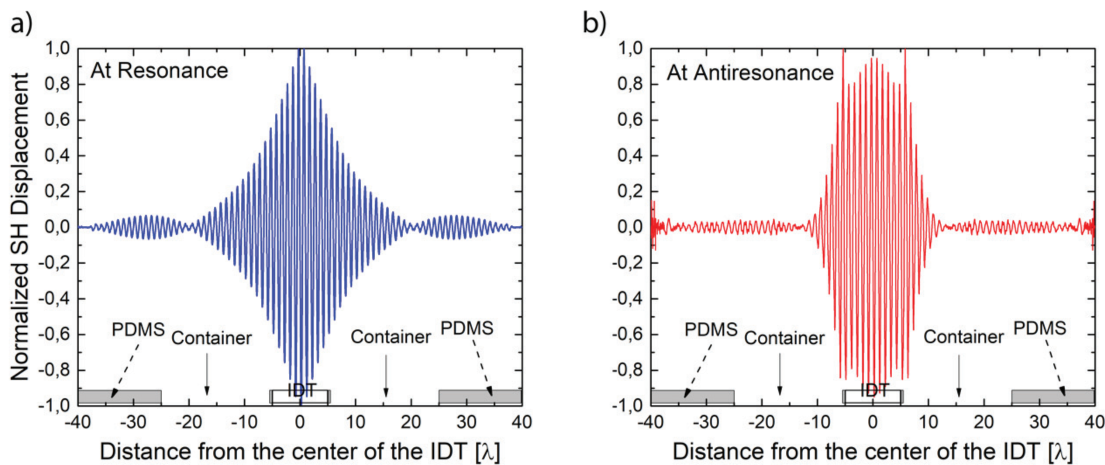

Figure 33*.* Normalized SH-SAW displacement distributions as simulated at **a)** resonance and **b)** antiresonance. The bottom part shows the positions of the microfluidic chip cavities above IDT and reflectors. At m = 0.5, the SAW displacement is decaying exponentially [134].

To address the sensitivity limitation imposed by the decaying nature of the SAW inside the sensing area, i.e. reflectors, a lateral SAW localization through a specially designed SAW energy confinement topology was introduced, enhancing the device sensitivity to approach the theoretical limit of the SH-SAW [**Paper III**]. The concept of the "*lateral energy confinement*" (LEC) design is shown as fabricated in figure 34. It utilizes the same material stack and grating pitch as described before. However, a variation of grating reflectivity is introduced to confine a larger amount of SAW energy in the sensing containers: a domain of reduced reflectivity is established just beside the IDT that enables significant amount of SAW energy to be concentrated in the sensing domain at resonance.

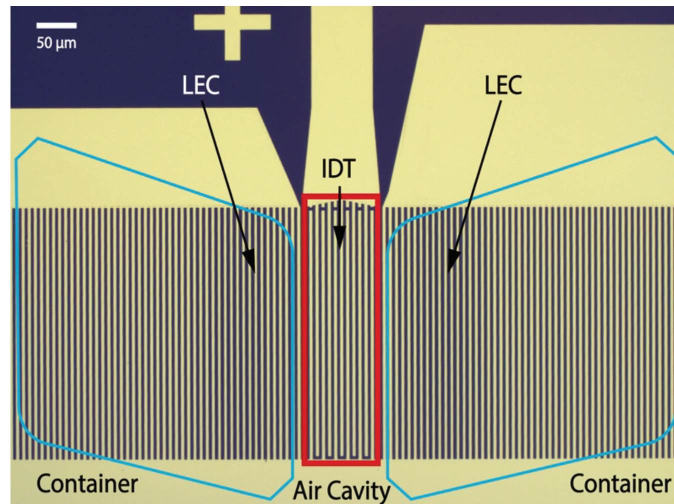

Figure 34. SAR sensor with *lateral energy confinement* (LEC) reflector topology. The outline of the air cavity above the IDT is depicted in red, while containers are indicated by blue outlines. The LEC regions are highlighted [134].

The reduction of grating reflectivity is achieved through an area characterized by narrower grating strips, i.e., strips with a smaller width-to-pitch ratio. In figure 35 the specific variation of the width-to-pitch ratio is shown. In the earlier SAR sensor design, the width-to-pitch ratio was m = 0.5 for all strips in the reflector grating, while here it narrows locally to m = 0.4 forming two energy localization domains centered at about 5 wavelengths from the IDT ends. In the improved design, the IDT consists of 7 pairs of electrodes for wideband operation.

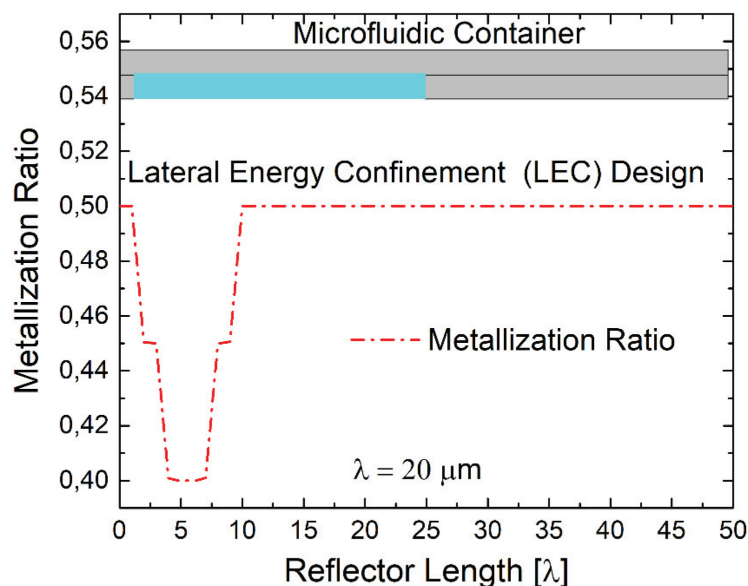

Figure 35. Lateral modulation of the width-to-pitch metallization ratio of the grating strip defining the acoustic wave confinement regions. The top section of the image shows schematically the position of the polymer part of the device, with the light blue part being the liquid- filled container [134].

The design follows the scheme depicted in figure 35 for the minimum metallization ratio inside the LEC zone, while the smooth acoustic impedance transition to it is provided by two pairs of grating strips with their metallization ratios derived as the mean value of the minimum and maximum metallization ratios. A FEM frequency response analysis of the proposed SAR device was performed to verify and reveal the fundamentals of the LEC performance. In figure 36, the transversal shear displacement distributions are shown as simulated at resonance and antiresonance for chosen LEC topology (m = 0.4).

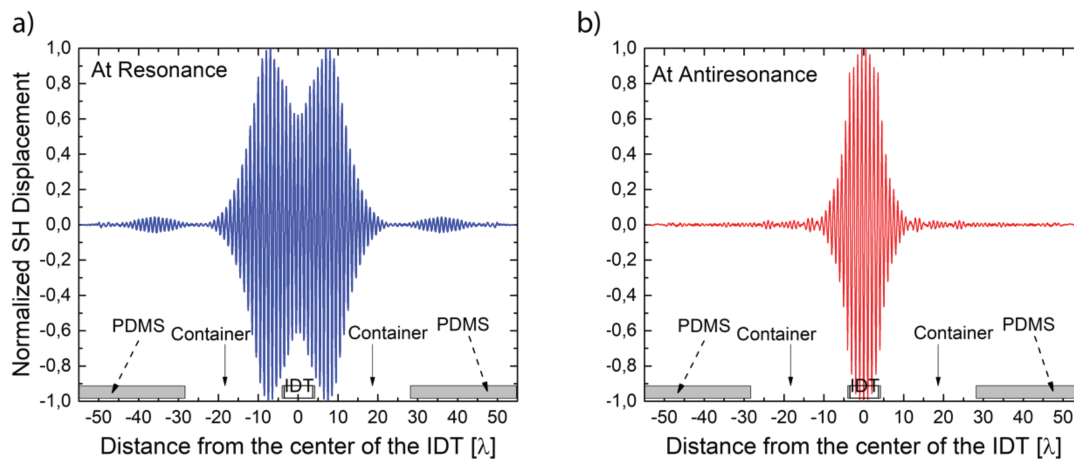

Figure 36. Normalized SH-SAW displacement distributions for LEC topology device (m = 0.4) as simulated at **a)** resonance and **b)** antiresonance. The bottom part shows the positions of the microfluidic chip cavities above IDT and reflectors. The SAW displacement is confined at the sensing surface within the containers [134].

The applied design scheme promotes energy confinement at the sensing surface within the containers. Lower minimum metallization ratios in the LEC domain ensure greater SAW confinement in the sensing area at the expense of coupling between the IDT and the SAW. The SAR sensor concept relies on both the ability of the IDT to probe sensitivity of the reflector gratings and the ability of the IDT to introduce sufficient energy into the sensing domain. In fact, there has to be a fine balance between these two requirements. For example, a SAR sensor with a very long IDT will have most of its energy under the IDT, and will not be able to sense outside of it. On the other hand, if energy confinement in the reflectors is too strong, most of the SAW energy will remain there, and as a result decouple from the IDT. Accordingly, in both extreme cases either the sensitivity or the electrical response of the device becomes poor.

To validate the choice of metallization ratio of m = 0.4 as optimal for the improved design, sensitivity and magnitude of the device response as a function of energy localization in the LEC domain were simulated. The sensor response was studied by applying a mass load over the container region of the resonator. In figure 37, normalized sensitivity and normalized magnitude of conductance are shown in a comparative manner for the LEC domains with a

varying minimum metallization ratio. As expected, the device sensitivity exhibits a maximum determined by the trade-off between the energy confinement in the sensing domain and the IDT coupling to the SAW at resonance.

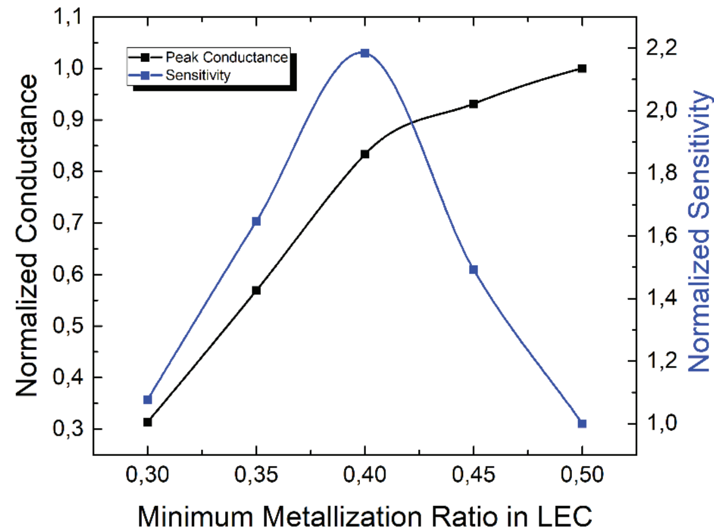

Figure 37. Normalized conductance and sensitivity at different metallization ratios as simulated [134].

Below a metallization ratio of 0.4, the IDT coupling rapidly decreases, which in turn determines its poorer probing abilities and thus reduced device sensitivity (*Fig. 38)*.

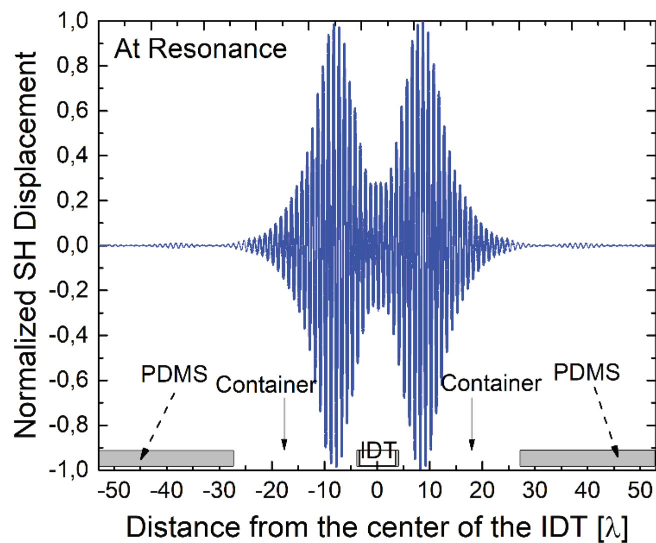

Figure 38. Normalized SH-SAW displacement distribution for LEC topology device (m = 0.3) as simulated at resonance. Here, most of energy is localized in containers, while IDT decouples from the system as can be observed from a low amplitude region next to it [134].

By contrast, at antiresonance the energy is confined predominantly under the IDT in all LEC designs, while the SAW amplitude is decaying along the reflector grating (*Figs. 33**b** and 36**b***).

Both modes of operation were compared experimentally with respect to their sensitivity [**Paper III**]. In figure 39, the conductance around resonance, and the resistance around antiresonance are shown as measured in air and water. The resonance frequency is approximately 188 MHz for the given device. Despite being from the same batch/wafer, each individual chip has tolerances within a few percent of the nominal value due to a technological drift. These drifts usually exist between different devices and are readily compensated by calibration routines. A frequency shift of the conductance peak of about −2200 ppm is observed as a result of water loading, accompanied by a -27% decrease of the conductance peak magnitude. Note that the sensitivities demonstrated at resonance in the original design were −915 ppm and −5%, respectively, while the maximum sensitivity was theoretically estimated to be about −2100 ppm (Table I).

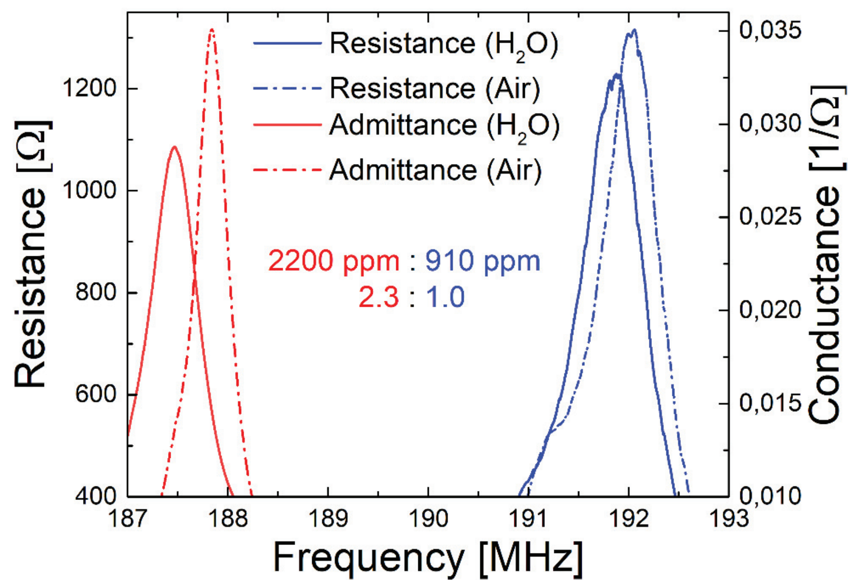

Figure 39. SAR sensor performance under water load. Admittance and resistance are depicted in red and blue, respectively. Dash- dotted lines represent water samples, and solid lines air samples for comparison.

At antiresonance, the observed frequency shift of the resistance peak of about −910 ppm determines a sensitivity which is 2.3 times smaller than the sensitivity of the resonance. This again demonstrates the impact of the energy distribution on the device sensitivity.

4.3 SENSOR CHARACTERIZATION

To further evaluate the performance of the SAR sensor, it has been characterized in an environment with varying (viscosity × density) product **(ρη)** by utilizing sucrose solutions of up to 50% content in *phosphate buffer saline* (PBS) (*Fig. 40*) [**Papers II-III**]. The results are summarized in the table *II*. An overall two-fold increase in sensitivity can be observed. The SAR sensor can tolerate damping induced by the viscous loading well, exhibiting about -17% decrease in conductance peak magnitude for *sucrose-PBS* solutions of up to 50%. The observed attenuation is about three times higher than that of the design without LEC topology, which is related to the increase in sensitivity demonstrated by the new design. At the same time, the attenuation is still within acceptable limits, low impedance at resonance is retained.

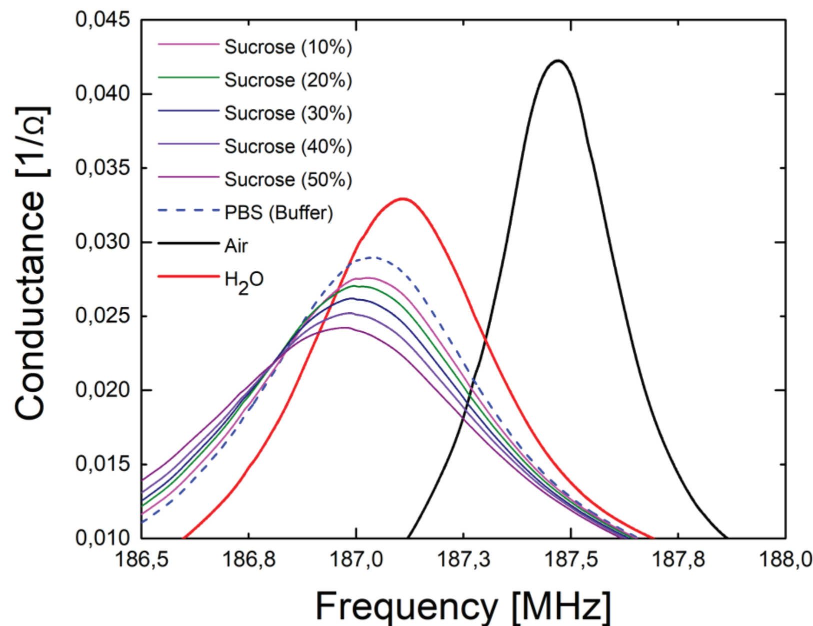

Figure 40. SAR sensor performance under viscous load. The colored graphs represent the signals of different sucrose solution loads, the dashed line belongs to the buffer reference (0% sucrose), and the black line is the signal of the empty containers [134].

Sensor bias	Design **without** LEC **Δf [ppm]**	Design **with LEC** **Δf [ppm]**
air to water	-915	-2200
water to PBS	-160	-315

PBS to 20% sucrose	-160	-220
PBS to 40% sucrose	-260	-600
PBS to 50% sucrose	-450	-960

Table II. SAR sensor sensitivity under varying viscous loads.

In table III, the demonstrated frequency sensitivity is presented in comparison to some of the state-of-the-art sensors. Here the results for the FBAR are scaled down correspondingly to the lower frequency of 185 MHz, taking into account the $f^{0.5}$ dependence of the relative frequency shift [73]. The improved SAR sensor design demonstrates sensitivity comparable to FBAR at an almost 5 times lower frequency even without applying the frequency scaling.

Sensor type:	**SAR (1-port)** [124, 134] **185 MHz**	**FBAR (1-port)** [19] **900 MHz**	**SAW delay line (2-port)** [135] **100 MHz**
Notes:	~~*LEC*~~/**LEC**	***Frequency*** *scaling*/**no scaling**	
Δ (ρ×η)	**Δf [ppm]**	**Δf [ppm]**	**Δf [ppm]**
1 to 2.3	*-260*/**-600** (damping 2%)	*-270*/**-600** (damping 30%)	-
1 to 4.35	*-450*/**-960**	-	*-500*

Table III. Comparison of the obtained results with some of the state-of-the-art sensors [19, 135].

Time-resolved measurements were performed to investigate the sensor recovery and the measurement noise [**Paper III**]. In figure 41, measurement results of different concentrations of glycerol in water are presented. In this set of measurements, water is used to establish the baseline sensor response level after each individual measurement of glycerol solution. The results show that, when water is introduced to the sensor containers, the resonant frequency recovers repeatedly to the initial value, providing a stable baseline. When the sensor is exposed to glycerol solutions, the resonant frequency decreases to a concentration-dependent value, which remains unchanged over the measurement window, indicating sufficient stability of the SAR sensor for practical purposes.

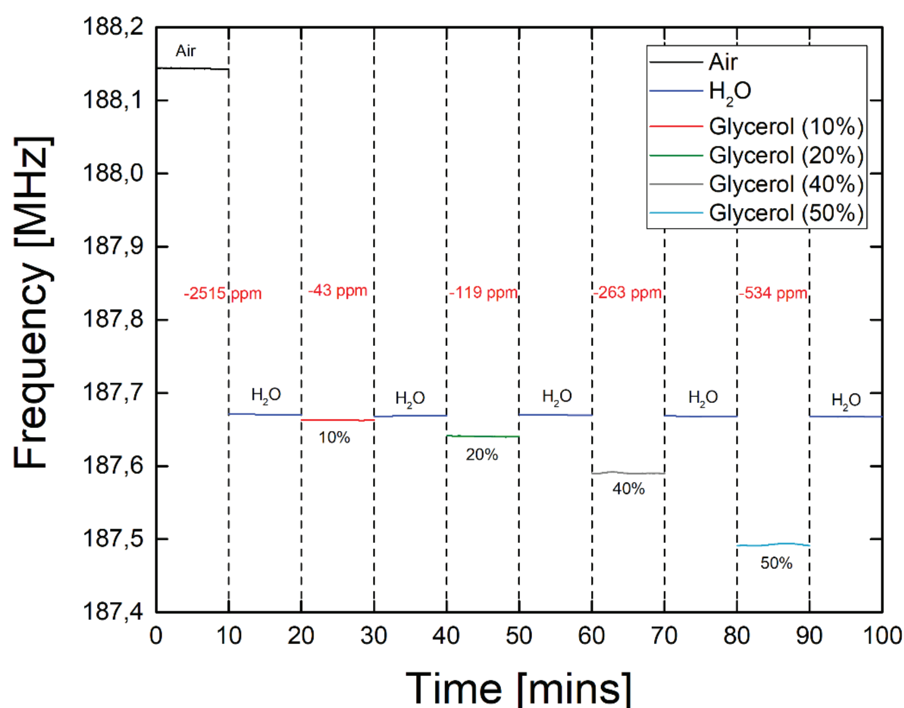

Figure 41. Time-resolved response of the SAR sensor under viscous load. The colors encode the signals for air (grey), water (blue) and glycerol loads of different concentrations. Frequency shifts per time step are indicated in red [134].

The noise level was calculated using averaging of the Allan deviation σ over 10 minutes. Each σ was derived from 200 subsequent measurements at 3 s intervals with the vector network analyzer (VNA) at 3 dBm input power. The measured conductance magnitudes were fitted near resonance to a 5th order polynomial, and the resonance frequencies were subsequently extracted from the polynomial fit of each measurement. Noise levels under load were determined over 10 min to be below 0.5 ppm for resonance frequencies, and below 10 ppm for the conductance peak. This number determines the *limit of frequency detection* ($3\sigma < 1.5$ ppm) and the *limit of conductance magnitude detection* ($3\sigma < 30$ ppm). Further improvement in the limit of frequency detection is possible through an increase of the input power of the VNA used in the measurements, and through ensuring better thermal stability of the physical measurement environment.

4.4 Biochemical Sensing

One of possible applications of liquid sensors is sensing of biomolecule interactions. In this context, supported lipid bilayers (SLBs) are a versatile model system for mimicking biological membranes. They are utilized for membrane protein investigations [136-138], studies of cell adhesion [139-141], membrane fusion and interaction with various molecules

[142]. These nanometer-thick membranes are particularly suitable for evaluating sensor performance, as they provide small mass loadings, ease of deposition on a solid support, and a rich feature set of electrical and mechanical properties that strongly depend on the composition and chemical environment.

A two-step experiment was performed using a microfluidic chamber at 21 °C. A biotin-modified SLB was deposited over the entire resonator area; following by subsequent addition of an extra load of neutravidin-coated nanoparticles through an affinity reaction to biotinylated lipids in the membrane *(Fig. 42)* [**Papers II-III**].

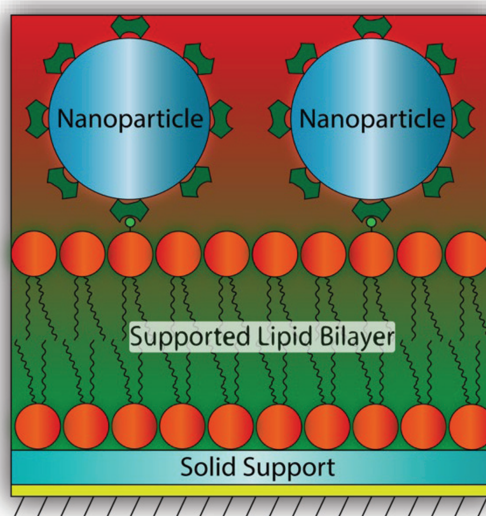

Figure 42. Schematic representation of the affinity assay [134].

The chambers were initially loaded with MQ water (MQW), the water was then exchanged by HEPES, the HEPES by a suspension of multi-lamellar vesicles (MLVs) in HEPES. The excess of the liposomes in the suspension was washed away with HEPES. In the last step, protein-coated nanoparticles (NPs) were added. Time-resolved changes of resonance frequency and conductance magnitude at resonance for each step in the deposition experiment are shown in figure 43. The sensor measurements are summarized in *Table IV.* The formation of the SLB on the chip surface, and particle attachment were verified by fluorescence microscopy imaging (*Fig. 44*).

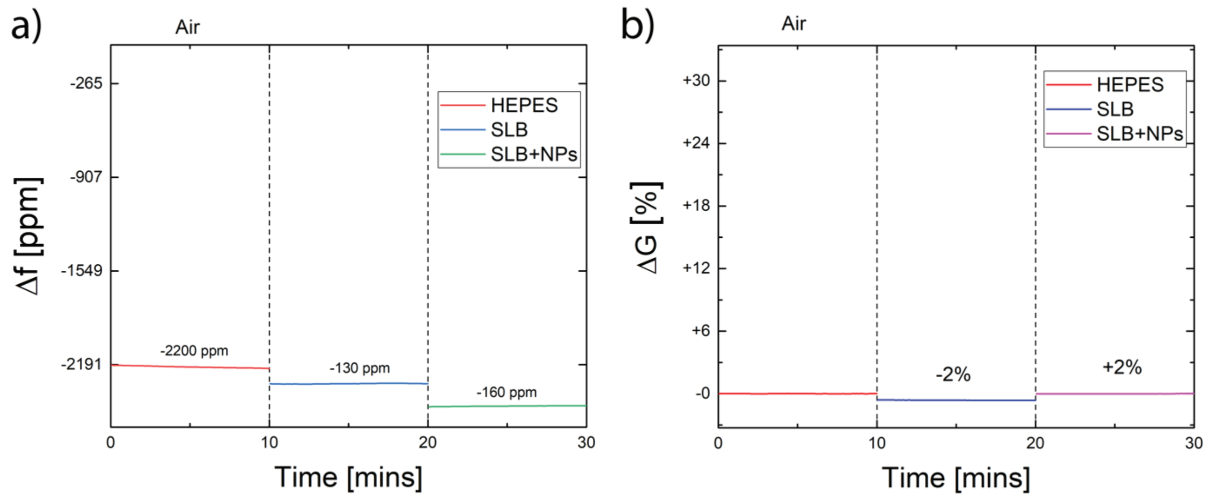

Figure 43. Time-resolved response of the SAR sensor subjected to the SLB deposition/affinity reaction sequence; **a)** frequency shift; **b)** peak conductance magnitude shift [134].

Sensor bias	Design **without** LEC	Design **with LEC**
	Δf [ppm]/ΔG	**Δf [ppm]/ΔG**
HEPES to SLB	-65/0%	-130/-2%
SLB to SLB/NPs	-90/+2%	-160/+2%

Table IV. SAR device sensitivity.

A large frequency downshift was observed upon addition of water. This could be attributed to the loadings emanated from the (***ρη***) product and the dielectric permittivity. PBS is characterized by a very similar (***ρη***) product when compared to water, and the observed frequency downshifts is due to the change in conductivity of about 1 S/m. The deposition of a lipid layer leads to an additional frequency and conductance peak magnitude downshift because of its mass and viscous loading. In the last step, the binding of the nanoparticles results in a further frequency downshift. When compared to other acoustic sensors, the frequency downshift of a SAW resonator is not always correlated with a reduction in the magnitude of the measured conductance. The nanoparticles deposited over the reflectors appear to enhance reflectivity, and in turn increases the conductance magnitude of the SAR device. Accordingly, SLB deposition represents a mass loading with effect on the viscoelastic properties of the sensor surface, while the reaction with NP contributes to increased rigidity of the biolayer, as indicated by the increased magnitude of conductance peak. This specific performance might be very useful for discrimination between different types of surface loadings.

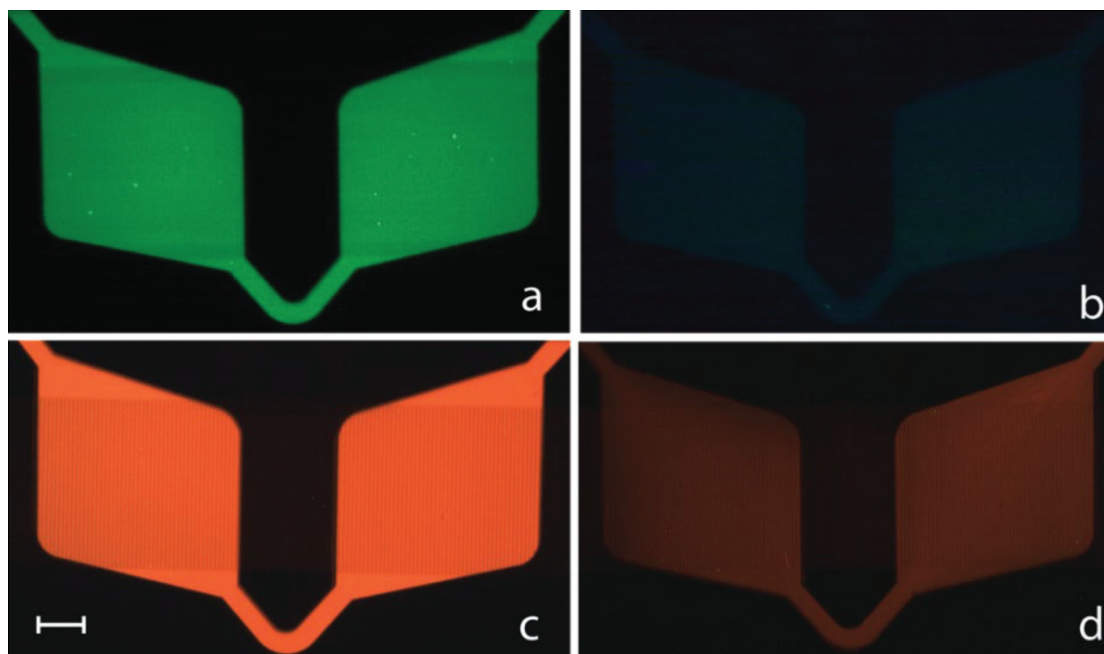

Figure 44. **(a-b)** Fluorescence images (ATTO-488 channel) of the sensor loaded with liposome suspension before and after washing. **(c-d)** Fluorescence images (Nile red channel) of the sensor loaded with nanoparticle suspension before and after washing. The scale bar in **(c)** represents 100 µm and is applicable for all panels **(a-d)** [124].

4.4.1 Sensing of SLB Transformations

Divalent calcium cations (Ca^{2+}) are known to bind to negatively charged phospholipids, such as phosphatidylserine [143], and lead to a tighter packing of molecular lipid films, dehydration of lipids, as well as conformational changes to the lipid headgroups [144]. Generally, the fluidity of the membrane is to some extent reduced. Recent research has also shown that local exposure of lipid membranes in the low-tension regime (excess lipid material) to calcium ion concentrations in the arrange of 1–5 mM leads to a partial transformation of planar membranes to nanotubular structures that extend into the aqueous medium but remain attached to the membrane [145]. This transformation, when it occurs on a surface-supported membrane, would effectively lead to a transfer of lipid material from an adhered surface film into the aqueous space above it, where parts of the lipid material float close to the membrane in a loosely connected regime. This should decrease the effective loading, owing to the 40 nm decaying length of the 185 MHz SH-SAW, resulting in a measurable increase in resonance frequency.

Exposure of the SLB to 5 mM Ca^{2+} is accompanied by a frequency upshift of about +20 ppm, and a simultaneous conductance peak upshift of about 2% (*Fig. 45*) [**Papers III-IV**]. The upshift of both quantities is attributed to the above-mentioned decrease in effective mass loading, but also to increased rigidity of the calcium-rich SLB layer.

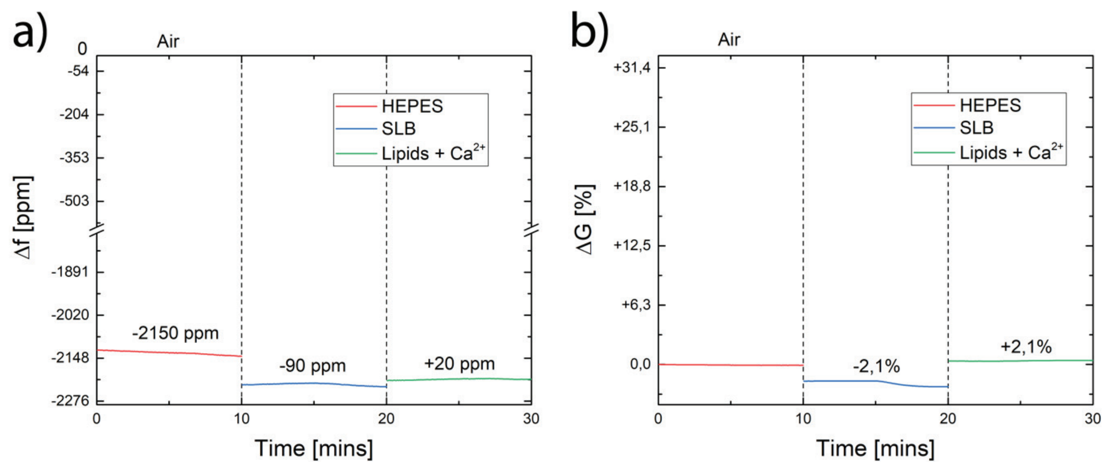

Figure 45. Time-resolved response of the SAR sensor subjected to the SLB reaction with Ca^{2+}; **a)** frequency shift; **b)** peak conductance magnitude shift [134].

For reference, this behavior was captured by laser scanning confocal microscopy, both on the sensor surface (*Fig. 46a*), and on a SiO_2-coated glass surface (*Fig. 46*b-e). In figure 46a a mixed film of lipid layer (lower intensity dark green) and sparse MLVs (the lighter-larger objects having size of about 10 µm and larger) are seen attached to the SiO_2 coated sensor surface. In a separate experiment an MLV on SiO_2 coated transparent glass substrate (*Fig. 46*b), allowing for close proximity observations, was subjected to Ca^{2+} interaction. Calcium ions at concentrations > 0.8 mM initiate tension-driven surface wetting (Marangoni flow) by the lipid deposit, where the lipid layer spreads in a circular fashion as a rolling double bilayer from the MLV, gradually consuming the MLV (*Fig. 46*c) [146]. Excess MLVs are flushed away in a subsequent washing step (*Fig. 46*d), leaving behind a continuous lipid film on the surface. The membranes originating from different spreading patches merge in this process (*Fig. 46*e). Ca^{2+} ions continuously pin the lipid layer to the surface, forming a rigidified solid-supported layer. When the lipid reservoirs are depleted, the continuous adhesion to the surface promoted by Ca^{2+} pinning causes a significant increase in lipid membrane tension, eventually resulting in rupturing. The lipid material released by the rupture process is transferred to the proximal bilayer [147].

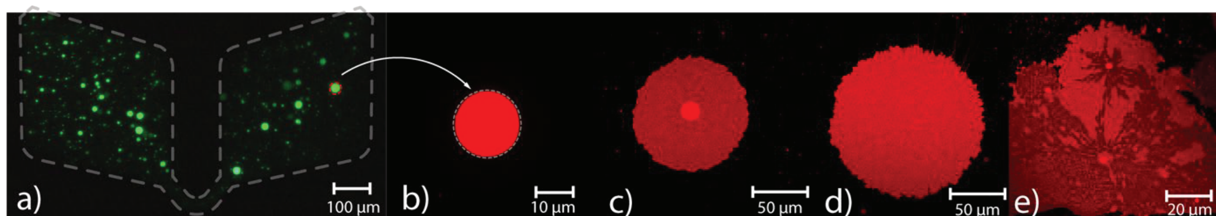

Figure 46. Fluorescent micrographs of **a)** MLVs deposited on the sensor surface – the shape of the two fluidic chambers is outlined with a dashed contour; **b)** Individual spherical lipid reservoir (MLV) containing multiple stacked layers of lipid membranes (onion shell vesicle). The MLV in **(b)** is structurally representative of, but not identical to, the vesicle encircled in **(a)**; **c)** double lipid bilayer membrane formed by self-spreading from the MLV (bright spot at the center) upon addition of Ca^{2+} to the ambient buffer; **d)** lipid membrane after removal of excess lipid reservoirs due to applied hydrodynamic flow; e) Continuing spreading causes an increase in membrane tension, eventually resulting in rupturing of the upper bilayer membrane.

4.5 INTEGRATION OF SAR SENSOR WITH ELECTROCHEMICAL IMPEDANCE SPECTROSCOPY

This sub-chapter describes the integration of SAR gravimetric sensing with *electrochemical impedance spectroscopy* (EIS) in a single device with microfluidic support [**Paper IV**]. *Impedance spectroscopy* (IS) integration with acoustic wave sensing has been earlier successfully demonstrated with the QCM platform [148-151]. The proposed implementations feature an additional reference electrode, which occupies extra space as it is not functional part of the QCM itself. Such integrated sensors can detect mass changes and viscoelastic properties, and provide a response related to the dielectric properties of the analyte at the sensor interface. Simultaneous, complementary measurements of both mechanical and electrical characteristics of the chemical or biochemical system under investigation are foremost a reliable way to evaluate the reproducibility of individual sensor data, and to reveal additional information of system features and behavior [152].

The proposed integration relies on the SAR sensor reflector gratings, which are reconfigured into an *interdigital electrode* (IDE) capacitive configuration [153-156], galvanically isolated from the SAW transducer. In a standard SAR configuration, these gratings are electrically short-circuited. In addition to the galvanic isolation, SAW and impedimetric measurements are performed within non-interfering frequency bands leading to significantly suppressed measurement crosstalk. Impedance spectroscopy is performed at frequencies below 1 MHz, while SAW resonance is monitored at about 185 MHz. Furthermore, QCM sensors integrated with impedance spectroscopy employ relatively close (i.e. eventually interfering) frequency bands due to the fact that the operational frequency of a typical QCM device is in the range of 5 MHz to 10 MHz.

Specifically, the integration of the SAR sensor with impedance spectroscopy is embodied through changes in the electrical connections of the strips in one or both of the SAW reflector gratings. In this configuration one of the grating busbars remains a common ground to the IDT, while the other becomes an EIS signal pad. The grating strips are now connected as interdigitated electrodes. A regular IDE arrangement with periodicity of the polarity resembling that of the IDT (2 strips per λ, where λ is the SAW wavelength at resonance) should be avoided, since such structure will receive the propagating SH-SAWs electrically and causes re-excitation of SAWs because of electrical impedance mismatch at the IDE electrical ports. That will ultimately perturb the SAW sensitivity due to externally induced wave interference effects. Instead, the IDE should be arranged in split electrode configuration with the frequency of SAW excitation being different from the SAW resonance frequency. Thus, effects of SAW re-excitation and SAW related charge accumulation can be readily avoided at the cost of reduced static capacitance of the structure.

A trade-off IDE design was proposed with retained capacitance employing a split configuration of 3 electrodes per λ in the first 10λ next to the IDT, while the rest is in regular IDE configuration with 2 strips per λ. In such configuration the SAW energy is strongly confined near the IDT, while attenuating along the reflectors. This attenuation is further boosted by the damping effects in the presence of liquid in the microfluidic containers. Accordingly, SAW regeneration is not likely to appear in the regular IDE part. SAW regeneration is associated with formation of charge on the strips that are in synchronicity with the SAW at resonance. Thus, the split-electrode section of the IDE ensures cancelling of the SAW induced charge and provides sufficient isolation between the EIS and the IDT ports. Furthermore, the IDE structure was reduced to only one of the reflector gratings, while the other remained electrically grounded. The latter is needed to ensure easy contacting to the SAW and EIS ports. Figure 47 depicts a schematic view of the implemented design along with an image of the SAW-EIS tandem sensor assembly.

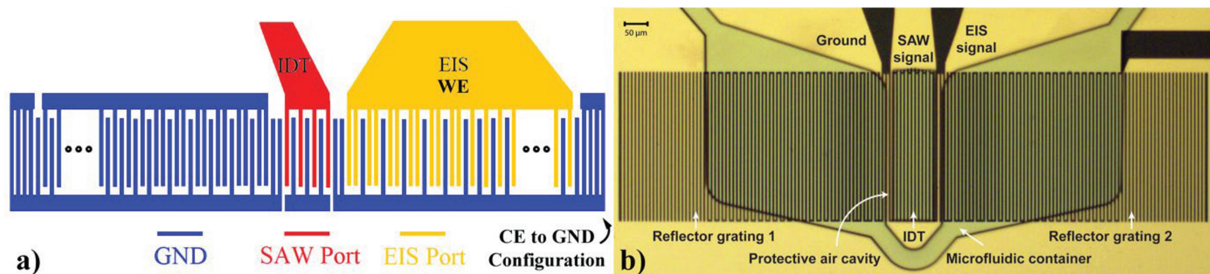

Figure 47. **a)** Schematic view of the implemented design (WE stands for work electrode, CE for counter electrode, GND is a ground) and **b)** Optical microscopy image (top view) of the assembled microfluidic SAR/EIS tandem sensor.

The crosstalk between the sensing ports was initially tested by measuring the transmission insertion loss between the two ports. S_{21} measurement was performed by means of a VNA in the frequency range 300 kHz – 200 MHz, limited by the lowest frequency of the VNA. The transmission loss between the IDT and the EIS port measured near 185 MHz was found to be as low as -60 dB, while in the range from 300 kHz to 1 MHz it was varying from -120 dB to -90 dB. This crosstalk is purely capacitive and is introduced by the contact pads. An improvement through optimized interfacing can be anticipated. The EIS operates at a frequency where acoustic waves are not excited, thus both functionalities, i.e. acoustic sensing and EIS sensing, can be operated independently. Initial tests of the sensor in liquid environment have shown practically no mutual interference and influence on the measurement data. The noise of the resonance frequency measurement remained below 0.5 ppm.

4.5.1 Multiparametric Sensing of SLB Transformations

The integrated SAR-impedance spectroscopy dual-sensing device was tested in an aqueous environment in the presence of lipid reservoir deposits on the sensor surface, which was further subjected to interaction with Ca^{2+} ions as discussed previously [**Paper IV**]. When lipid vesicles attach and spread on the sensor surface, the acoustic wave detects changes in mass and viscoelasticity by detecting shifts in resonant frequency and magnitude of conductance peak of the SAR sensor. On the other hand, the integrated EIS provides information about the electrical properties of the lipid membrane, such as its dielectric permittivity and dielectric loss (resistivity).

The impedance spectra of the sensor were obtained by applying a 7.07 mV RMS AC voltage in the frequency range from 1 Hz to 1 MHz. The measured data had to be further quantified through an *equivalent circuit model* (ECM) to obtain characteristic quantities. Figure 48 shows a schematic representation of the IDE structure in contact with solution and deposited (lipid) film, and its *simplified* ECM that gives the best fit. R_{Sol} represents the intrinsic buffer solution resistance superposed to the parasitic resistance of the IDE structure itself (the latter being the only contribution when measuring in air (R_{Geo})). R_{Leak} is determined by the leakage current going through the electrode interface with the analyte and the biochemical deposits, and C_{Geo} is a geometric (stray) capacitance between two electrodes through the medium (including the $LiNbO_3$ substrate, the liquid dielectric permittivity and the thin SiO_2 coating, as well as any parasitic capacitances in parallel emanating from the connection of the IDEs to the potentiostat). Capacitance of the lipid layer C_{Lipids}, that is in series with the double layer capacitance C_{Dl}, appears between IDEs and the analyte. In reality, the double-layer capacitor often deviates from an ideal capacitor due to roughness, porosity and inhomogeneities on the IDE surfaces. For that reason, an empirically modelled *constant phase element* (CPE) is used instead of an ideal capacitor to represent C_{Dl}. The electrical double layer capacitance mainly depends on the ion type and concentration, while changes in CPE_{Dl} are also attributed to the formation of an additional layer on the electrode surface which in the given case is a lipid layer. In air this equivalent circuit is further simplified, featuring only the upper branch of capacitance and parasitic resistance in parallel (R_{Geo}). When the lipids are not present on the sensing surface, the CPE_{Dl} complementary C_{Lipids} component is also omitted from the in-liquid ECM.

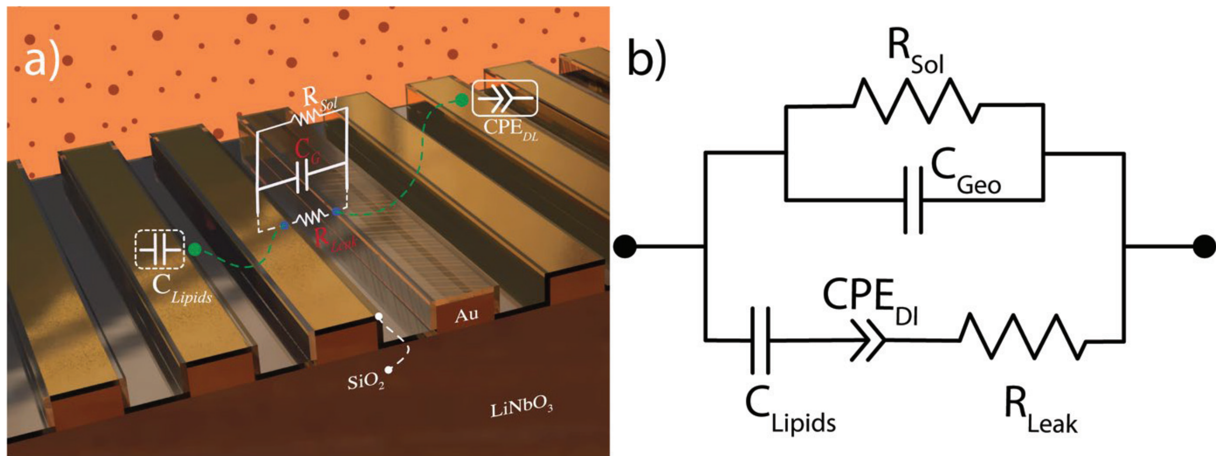

Figure 48. The IDE equivalent circuit model **a)** sketch view; **b)** schematic view.

In real experiments that involve EIS sensing, the sensitivity is considered with regard to the change of the lumped elements. Most sensitive elements are identified and selected as sensing quantities. Although the lumped elements have physical meaning, their behavior is typically not determined independently because of the inherent complexity of the sample composition. CPE_{Dl} and R_{Leak} components are often good identifiers of the interface phenomena resulted from biochemical reactions, while C_{Geo} and R_{Sol} provide information about the bulk environment.

The performance of the EIS-SAR sensor was initially assessed through measurements in air and *deionized water*. Upon exposure to water, a strong response of the SAW resonance frequency of about -2000 ppm and the magnitude of conductance peak of about -32% were observed. EIS measurement in air and water reveals the distinct performances of the IDE in both environments. As seen from the Nyquist plot in figure 49a, the IDE performance in air is well represented by the semi-circle determined by the stray capacitance C_{Geo} and the parasitic resistance. At frequencies below 10 Hz the measurement instability is dominating, which is a known issue in EIS at very high impedances, because of very small currents that are being measured. Upon contact with water the CPE_{Dl} becomes evident at the Nyquist plot (*Fig. 49*b) through the constant slope of the curve especially in the frequency range bellow 1 kHz. In frequency range from 1 kHz to 1 MHz a semicircle can be seen, the diameter of which depends on the conductance of the media R_{Sol} and the stray capacitance C_{Geo} in parallel with each other. At frequencies below 1 kHz, the impedance is dominated by CPE_{Dl}, which is caused by the electrical double-layer at the IDE/water interface.

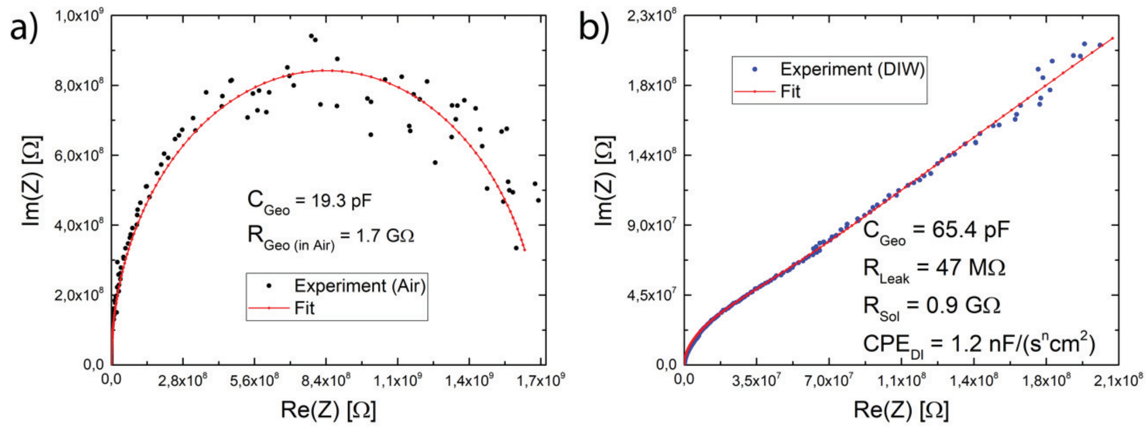

Figure 49. Nyquist plot of EIS response for data obtained experimentally vs. their fit, along with extracted values for each equivalent circuit model component are shown for **a)** air and **b)** water.

Considering the noise-related signal instability at frequencies below 10 Hz, the impedance curve recorded at 10 - 100 Hz appears to be appropriate for monitoring the change of CPE_{Dl}. At higher frequencies up to 1 MHz, the dielectric behavior (i.e. C_{Geo}) of the solution dominates the signal. The integrated EIS-SAR sensor demonstrates physically meaningful responses: the IDE capacitance shifted to C_{Geo} = 65.4 pF, which accounts well for the twice larger dielectric permittivity of water as compared to $LiNbO_3$. R_{Sol} has shifted down to 0.9 GΩ due to the finite resistivity of the water. The appearance of double-layer is indicated by the CPE_{Dl} = 1.2 nF/(s^n cm^2) and interface leakage current determined by the R_{Leak} = 47 MΩ. Although the EIS response is dominated by the latter, in the higher frequency range the stray capacitance becomes a current flow path concurrent to the water/IDE interface.

When water was replaced with HEPES buffer needed for the subsequent lipid deposition, an additional SAW resonance frequency shift of about −118 ppm, along with a -2.1% decrease of the conductance peak magnitude were observed. The impedimetric measurement shows an overall decrease of impedance as seen on the Bode plot in figure 50. The decrease can be observed in both low and high frequency regions suggesting changes near the IDE surface and in the liquid volume. This observation is further quantified in table V, where CPE_{Dl} increases by 30% from 1.2 nF/(s^n cm^2) to 1.6 nF/(s^n cm^2).

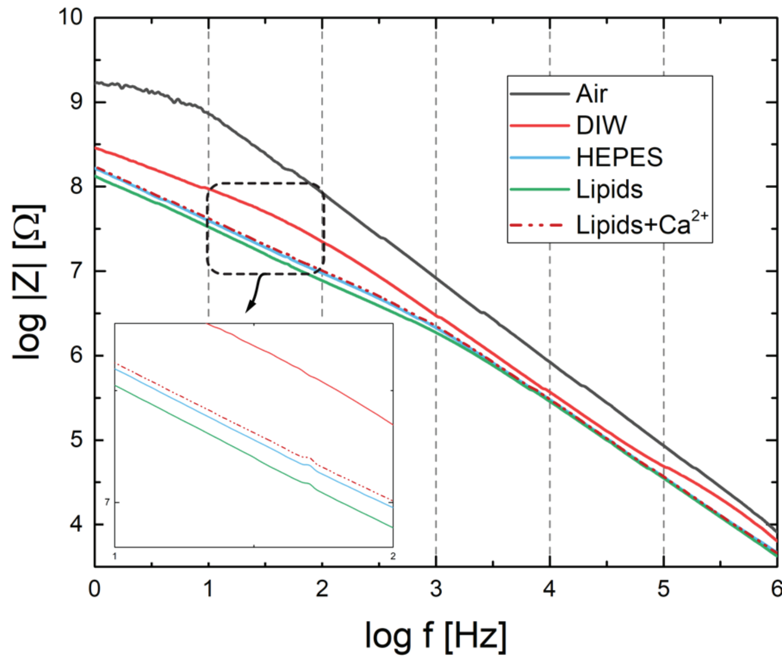

Figure 50. Bode plot of impedance spectra for different analytes. An inset in the bottom left corner is a zoomed-in region of 10 Hz – 100 Hz response from the same plot.

The lipid membrane was formed in the following step by exposing the SiO_2-coated surface to a multilamellar vesicle (MLV) suspension in HEPES buffer. The SAW resonance (table V) underwent a strong downshift of -86 ppm due to the viscoelastic mass loading at the surface, while the magnitude of peak conductance decreased by -2.3%, caused by acoustic wave damping in the lipid layer. The EIS response for the deposition of lipid bilayer on the sensor surface adds a new charged layer as a leaky capacitor in series with the double layer *(C_{Lipids})* that is also causing improved conduction through the double layer, i.e., a change in the fundamental double-layer properties. These effects can be seen below 1 kHz, where the impedance is lower as compared to that of HEPES. For frequencies above 1 kHz the changes are insignificant since the response is dominated by the electrical properties of HEPES. These observations are further confirmed by extracting the elements of the ECM through fitting process (table V). The combination of obtained SAW and EIS quantities suggests that a layer with distinct viscoelastic properties and leaky capacitance behavior has been formed on the sensing surface.

Upon addition of Ca^{2+} ions, a strong upshift of both SAW resonance frequency and magnitude of peak conductance of about +19 ppm and +2.1%, respectively, was observed. This shift brought the response to levels of the magnitude of peak conductance very close to the HEPES level, while the resonant frequency remained closer to the lipid levels. The measurement was performed after the transformation was complete, which was confirmed by the stabilized sensor response. This response to Ca^{2+}-induced lipid spreading is in good

agreement with the data obtained previously. Relatively strong upshift of the magnitude of peak conductance of about +2% and upshift in the frequency around +20 ppm were observed.

Parameter:	**Δf [ppm]**	**ΔG [%]**	**C_{Geo} [pF]**	**R_{Leak} [MΩ]**	**CPE_{Dl} [nF/(s^n cm^2)]**
DIW to HEPES	-118	-2.1%	65.4	47 to 4.2 (-91%)	1.2 to 1.6 (+30%)
HEPES to SLB	-86	-2.3%	65.8	4.2 to 2.9 (-31%)	1.6 to 2.9 (+45%)
Addition of Ca^{2+}	+19	+2.1%	65.7	2.9 to 3.3 (+14%)	2.9 to 1.8 (-38%)

Table V. Extracted EIS-SAW sensing quantities: SAW resonance frequency shifts [Δf], SAW conductance peak magnitude shifts [ΔG], EIS stray capacitance C_{Geo}, EIS interface leak resistor R_{Leak}, EIS double layer constant phase element CPE_{Dl}.

The Bode plot in figure 50 shows that the magnitude of impedance has recovered slightly above the HEPES level. This is associated with a significantly decreased conductivity at the interface layer and suggests an interface structure with reduced CPE_{Dl} and/or increased R_{Leak}. This behavior appears to result from the formation of an extensively ruptured rigid layer, which on one hand reduces the capacitance of the layer, while on the other reduces the surface leakage conductivity by neutralization of charge carriers through the Ca^{2+} reaction. As can be seen in table V, CPE_{Dl} has decreased by -38%, R_{Leak} increased by +14%, while C_{Lipids} practically vanished. Both the acoustic and the EIS responses underwent extensive signal recovery towards the base HEPES levels. The SAW resonance frequency and R_{Leak} have shown a moderate recovery, which is due to the partial, but not complete removal of weakly adhered reservoir vesicles. The remaining MLVs are transformed into the double bilayer during the spreading process. The magnitude of peak conductance and CPE_{Dl} recovered almost to the levels of HEPES, which is attributed to the loss of a homogeneous lipid layer in the rupturing process. Corresponding Nyquist plots can be seen in figure 51.

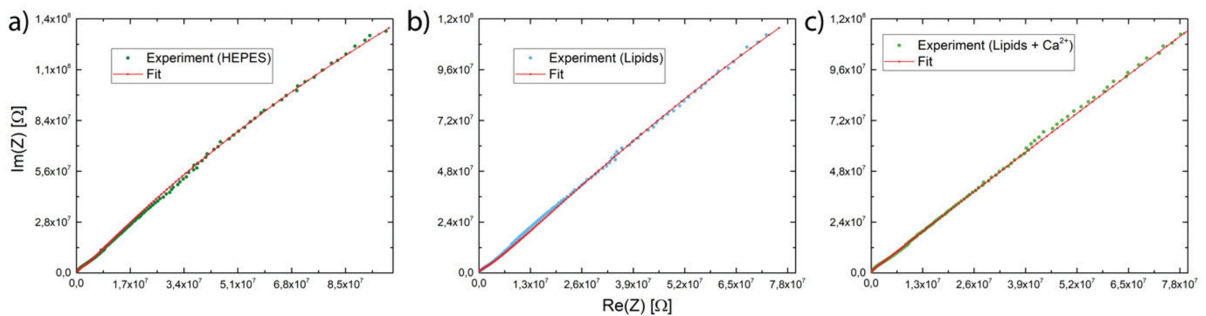

Figure 51. Nyquist plot of EIS response for data obtained experimentally vs. their fit for **a)** HEPES; **b)** SLB and **b)** SLB+Ca^{2+}.

5 DEVICE FABRICATION

5.1 PATTERN TRANSFER, THIN FILM DEPOSITION, ETCHING AND BONDING PROCESSES

Fabrication of the SAR liquid-phase sensors [**Paper II**] relies on microfabrication - a class of processing technologies that deals with fabrication of structures with at least one dimension being in the micrometer range [157]. Generally, microfabrication can be divided in to two categories:

- Top-down techniques;
- Bottom-up techniques.

The first method involves the creation of structures from a bulk material by means of selective removal or addition. This includes various patterning techniques such as lithography and printing. *Bottom-up* methods rely on physical and chemical properties of individual ingredients (e.g. molecules) in order to self-assemble them into the object of interest.

The fabrication processes in microtechnology are usually categorized by the construction method used- commonly referred to as a *bulk* and surface *micromachining* based on additive techniques. The first method is a removal or wet/dry etching of a crystalline or non-crystalline material in order to achieve 3D features, while surface micromachining builds up, layer by layer, on the surface of a substrate. Some examples include hard masking used during various etching processes, sacrificial layers used for fabrication of suspended structures, contacts and electrodes. Basic schematics of these processes are shown in the figure 52.

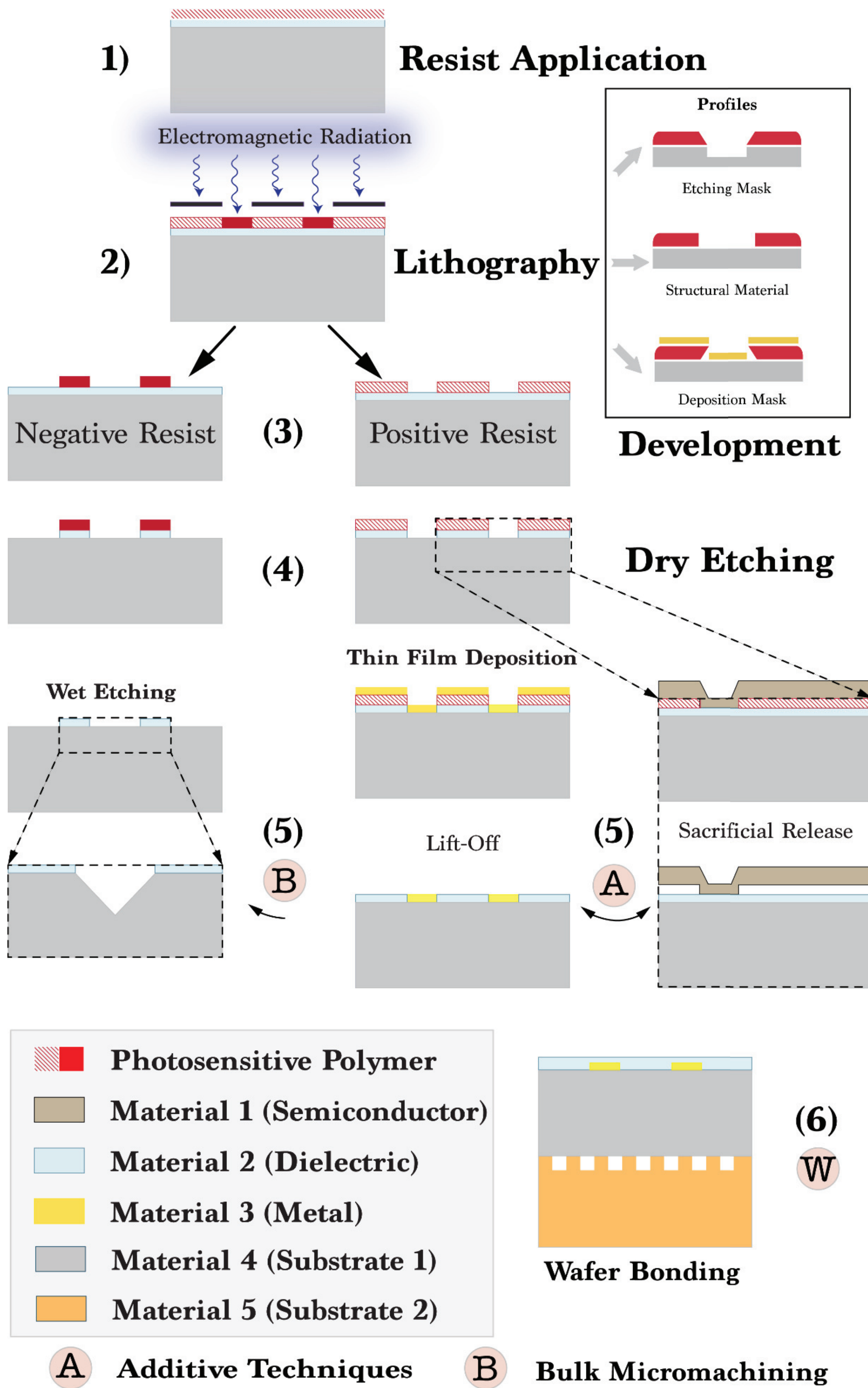

Figure 52. Schematic representation of some basic techniques used in micro- and nanofabrication processes.

Both surface and bulk micromachining methods heavily rely on thin films. Thin film processes allow for fabrication of various functional components and devices. Some examples include membranes, beams, plates, mirrors, electrodes and contacts, along with an entire range of *microsystems* (MST) and microelectronic devices. Thin films are also widely used for protection against mechanical and chemical damage, and as decorative coatings. In microtechnology, apart for being key functional components of the majority of fabricated devices, they are used repeatedly during the processing as protective and sacrificial layers, etch and diffusion masks.

Many properties of thin films such as resistivity, conductivity, coefficient of thermal expansion and refractive index are thickness-dependent. The chosen deposition method has a very profound effect on the resulting film. Depositions made with the same method, but within a different tool, can have a different result.

Sputtering or *evaporation* can be used to deposit different kinds of thin films (metals, alloys, ceramics, inorganic compounds and even polymers) on a variety of substrates of different sizes. Both of these methods are examples of *Physical Vapor Deposition* (PVD). However, they mostly find their use in the deposition of metallic and dielectric films.

The PVD processes are distinguished by the method of material ejection/charge of the ejected particle and can be grouped into the following categories:

- Thermal evaporation where the target material is being heated resistively or by electron beam;
- Sputtering where the ions are generated in plasma with an inert gas (Ar, Xe) and accelerated towards the target to physically remove the material. Here properties of plasma are controlled by means of power source operation modes (DC, RF or pulsed-DC, etc.), gas compositions and their flow rates; base pressure. When sputtering is carried out in the presence of a reactive gas, one can modify properties of the deposited film. This process is referred to as the *reactive sputtering*. For example, dielectric materials such as SiO_2 and Si_3N_4, piezoelectric ZnO and AlN can be deposited by sputtering Si, Zn and Al targets in the presence of O_2 and N_2 gasses, respectively;
- Laser ablation; high power pulsed magnetron sputtering (HPPMS) and some other *ionized* PVD methods (*ionized* indicates that the flux of charged particles is higher than that of neutrals).

Each method has its own advantages and disadvantages, and the resulting films will differ in density, crystalline quality and orientation (if applicable), stress, roughness, adhesion, step coverage, etc.

Another way to deposit a thin film is by *Chemical Vapor Deposition* (CVD). Here material precursors are supplied in a gas phase usually diluted with a gas carrier, decomposed in close vicinity to the surface of a substrate, where they react to form a thin film. The by-products are usually pumped away. Based on the decomposition method CVD can be grouped into:

- Thermal CVD (temperature induced decomposition);
- Plasma CVD or PECVD (plasma-enhanced decomposition).

Examples of CVD processes include APCVD (atmospheric pressure), LPCVD (low pressure), MOCVD (metalorganic CVD), ALD (atomic layer deposition) etc.

There are some other deposition technologies such as electroplating that is commonly used for thick metallization of high aspect ratio, electro-less deposition, sol-gel and spin-coating. Spin-coating is a widely-used method for applying photoresists on a substrate. Control over resist thickness relies on four different parameters: viscosity, solvent evaporation rate, spin speed and time [158]. Dispensing can be done in static or slow rotation mode. A drop of resist dissolved in a solvent is applied to the center of the wafer and spun with specified acceleration resulting in liquid spreading towards the edges. Rapid acceleration is important since solvent evaporation changes the viscosity of the resist. Thus, a radially non-uniform thickness will be obtained. Turbulence and ambient humidity, both being results of cleanroom environment and the spinner itself, affect evaporation rate and therefore film thickness. Pinhole defects caused by particles present on the wafer or in the resist can also appear during spin-coating. The definition of films at the edge of the wafer is often poor. Viscosity of the resist at the edge increases due to drying, and material accumulation on the rim of the wafer occurs (edge beads). In order to remove them, a directed solvent jet can be used. Films applied by spin-coating are good for filling and smoothing gaps. However, if a uniform thickness is required, the method is not ideal.

Lithography steps precede many subtractive and additive processes in order to define the geometry of a desired feature. Following that, materials are either removed or added to the device in a specific order. There are many methods that allow to remove the material by gaseous or wet species. In *dry etching*, the removal process is performed without wet chemicals or rinsing. It covers several techniques where the material is etched in the gas or vapor phase physically by ion bombardment, chemically by a chemical reaction through a reactive species present at the surface, or by combination of both mechanisms (physical and chemical) that is referred to as *reactive ion etching* (RIE). Plasma generation is an essential component of the dry etching. According to the way the plasma was generated, one can distinguish between the *glow discharge* (a broad plasma is generated in the same part of the

vacuum chamber where the substrate is located) and *ion-beam* (plasma is generated in a separate chamber or in another part of the same vacuum system from which the ions are extracted and transferred in a beam to the substrate by a number of electrode grids) etching. Additionally, it is common to differentiate between the **a)** *physical sputter/ion etching* (*ion-beam milling)*; **b)** *chemical plasma etching*, and **c)** *synergetic reactive ion etching*. In **a)**, etching is a consequence of momentum transfer between energetic Ar^+ ions and the material surface. This is a purely physical effect, while other methods rely on a of chemical reaction. In **b)**, neutral chemical species (Cl, F) generated in the plasma diffuse to the substrate, react with it and form volatile products with the layer to be removed. Here the plasma is used to supply gaseous, reactive etchant species. In **c)**, ions impact damage to the surface in line-of-sight, additionally inducing highly anisotropic chemical reactions with plasma neutrals.

5.2 LITHOGRAPHY

Photolithography is the most commonly used technique for pattern transfer due to its relative simplicity and good spatial resolution. It uses light passing through a mask to transfer a geometric pattern to photosensitive polymer (resist). Exposed with UV radiation, photoresist changes solubility, which allows to remove it selectively during the development. Photolithography consist of the following major steps:

- Substrate preparation;
- Resist application and treatment;
- Exposure;
- Post exposure resist treatment;
- Pattern development.

Generally, a photoresist is made of three components. These are:

- Base resin, which is responsible for mechanical and thermal properties of the resist;
- Photoactive compound (PAC) that determines the sensitivity to radiation;
- Solvent that controls viscosity and allows resist to be applied on the surface of a solid material for the following patterning.

Positive and negative resists can be distinguished, depending on how they behave once exposed (*Fig. 52*). Positive resists consist of a base that is soluble in alkaline developers and a photoactive compound that acts as an inhibitor, making unexposed resist insoluble. Upon exposure, PAC decomposes and therefore resist becomes soluble. Negative resists become insoluble when exposed due to a chemical reaction, such as acid-catalyzed cross-linking, that increases the molecular weight. Alternatively, photoproducts generated due to the chemical reactions in the resist cause solubility differences. Depending on the application or geometry that has to be transferred into the resist, one can choose either positive or negative resist based on the following criteria: the first is known to have a higher contrast and better thermal stability, while the latter has a better chemical resistance, mechanical stability and adhesion to substrate [157].

The quality of the photolithographic process depends on three different elements [158]:

- *Optics*: radiation generation, propagation, focusing, diffraction and interference;
- *Chemistry*: photochemical reactions in the resist, development;
- *Mechanics*: mask-to-wafer alignment.

Some examples of other options available for lithography include e-beam, nanoimprinting, laser, x-ray, thermal scanning probe, and some other techniques.

Resist contrast

Photoresist resolution and profile depend on contrast. It describes the change of solubility as a function of the absorbed light dose. High contrast resists have better resolution than those with a low contrast. To achieve good patternability, a sigmoid (non-linear step) response function is needed due to the fact that optical wavefronts passing through a photomask are not ideal square waves, but rather attenuated sine waves due to diffraction.

Resist profiles

A photoresist on its own is an optical system. The optical path of photons entering the resist is subject to constructive and destructive interference. This leads to intensity variations

in the vertical direction through the resist. Depending on resist thickness, choice of substrate and exposure system, a number of different profiles can be obtained after development. These are shown in *figure 52.* Positive photoresists usually suffer from overcut profiles, however using multiple resists or specifically optimized post-exposure processing allows to obtain undercut profiles. Vertical or undercut profiles are characteristic for negative resists and depend mostly on the exposure dose. Based on the application and processing requirements, all these profiles find their individual uses. For example, the undercut profile is widely used in lift-off processes, while vertical profile resists are used where precise geometry is needed.

SUBSTRATE PREPARATION

Before starting a process, wafers have to be cleaned from organic and ionic contaminants. This is done by soaking wafers in different solutions or by exposing them to oxygen plasma. One common solution widely used to remove organic contaminants and photoresist residues, in particular, is Piranha, a freshly prepared hot mixture of concentrated sulphuric acid and hydrogen peroxide (3:1), which is a strong oxidizing agent that is very effective for removing organic matter from the surface of a substrate.

SOFT BAKING

Soft baking is performed in order to remove solvents from the resist after spin-coating. Moreover, adhesion to the substrate is improved. Temperatures above T_g (glass transition temperature) are used so that the polymer can flow and relax, creating a proper environment for easy solvent removal. Baking the resist at lower initial temperatures gives more control over solvent evaporation rate, reduces edge bead and improves adhesion.

EXPOSURE

Once the photoresist pre-treatment is done, coated wafers are transferred to the optical exposure system. Such a system is expected to produce UV light of a defined intensity, directionality and uniformity throughout the whole area of the wafer. A photomask is placed between the substrate and the UV light source that allows to selectively expose the

photoresist. It is made of an optically even material which is transparent to UV light, and a metal pattern (chromium in most cases) that acts as an absorber. Depending on the application and mainly the resist used, photomasks can have either *bright field* or *dark field* polarities. The first has a transparent background with opaque features, while the latter has transparent features and an opaque background. The mask pattern itself can be written in a number of ways: depending on feature size and precision requirements, one can choose between electron-beam and laser writing. Similarly, during the prototyping stage, device geometry can be transferred into the resist without any masks by means of direct writing to save time and materials.

Post-exposure resist treatment

Once exposed, some resists have to be baked again in order to finalize the reactions initiated by UV light by a *post-exposure bake* (*PEB) process*. Subsequently, *development* has to be performed. Its purpose is to selectively remove exposed or unexposed resist parts from positive or negative resists, respectively. This will lead to an embossed image of the pattern used for the exposure. During wet development, swelling of the resist can occur along with loss of adhesion between the structures and the substrate.

Hard baking

Following the development, hard baking is often performed in order to remove the traces of solvent left in the resist and to anneal it. As a result, film hardness and substrate adhesion are improved. This is advantageous when the resist is to be used as an etch mask or serves as a functional part of a device itself. Hard baking is performed at higher temperatures and longer times as compared to pre-baking and post-baking.

5.3 Bonding

Two substrates can be bonded together to create cavities and seal channels, enabling 3D structures. Bonding can be performed in a number of ways [158]. However, they are mainly divided in two categories:

- Direct bonding;
- Indirect bonding by layer deposition ("gluing").

Direct bonding is based on strong chemical bonds that appear when two substrates are brought together. Indirect bonding relies on a number of materials (metals, glass, polymers) that can be used as a "glue" layer to keep wafers together. The main difference between the bonding methods comes from the various chemical and physical interactions that occur between the substrates, and on the strength and permanency. Some examples of available techniques are listed below:

- Fusion bonding;
- Anodic bonding;
- Thermo-compression bonding;
- Adhesive bonding.

Anodic bonding is the oldest method available. It was originally developed to bond glass and silicon wafers. At elevated temperatures glass decomposes and ions are produced. An electric field is then applied across the two wafers. As a result, ions move towards the glass and silicon wafer surfaces, away from the interface. This creates a depletion layer that electrostatically pulls two wafers together, establishing a strong bond. Due to the fact that this process relies on elevated temperatures, the *coefficients of thermal expansion* (CTE) of the two different materials have to be taken into account to avoid microcracking and to ensure a well-defined contact area. Generally, this applies to all bonding techniques that involve different materials and high temperature processing.

Thermo-compression bonding (TCB) uses heat and pressure applied simultaneously on the samples. Wafer-level bonding performed with this method relies on the deposition of thin films, the thickness of which corresponds to the eutectic composition, i.e., 97% gold and 3% silicon. The glass-frit is another example of a TCB product. It uses high temperatures and pressure to melt the material at the bonding interface and presses the components towards each other to create hermetic bonds.

Adhesive bonding utilizes polymers as an intermediate layer for joining two wafers together. The main advantages of this method are low processing temperatures and tolerance to particle contamination. Structured wafers can be also bonded together with low cost and simplicity using this process. Among the disadvantages is short-term stability of the bond.

Parylene is a common polymer used as an adhesive layer. It is an inert and tough material that is easy to deposit. When heated, the plastic melts and joins two wafers together.

Fusion bonding is a common technique used for joining structures made of materials with similar chemical composition. Functional groups present at the material surface will form a bond when contact is established. In case of Si these are silanol (–OH) groups. An O_2 plasma-activated condensation reaction allows for formation of covalent bonds between two PDMS slabs, or PDMS and glass. In general, plasma-activation is a common technique used in wafer bonding in order to improve the reactivity of a surface by replacing some of its dangling bonds present on the surface with more suitable ones.

Bonding plays an important role in many MEMS processes: it allows constructing permanent functional 3D assemblies, device packaging, temporal assemblies for extra mechanical stability during the intermediate processing steps (e.g. dicing, lapping etc.), and some others. Currently, a new generation of *incredible high-performance* (IHP) SAW devices is being developed and commercialized, to be used in the next generation (5G) communication standards. The key component of this new technology is bonding of two high acoustic performance piezoelectric materials to form a hetero acoustic layer (HAL) substrate [10]. For example, it is important to avoid the frequency fluctuation due to the heat generation and to increase the speed of SAW propagation in order to boost the performance of the device. $LiTaO_3$ and $LiNbO_3$ are known to have high acoustic velocity and electromechanical coupling, while suffering from temperature related parasitic effects. On the other hand, ST-Quartz has a high temperature stability and good piezoelectricity. By bonding any of these two substrates together, one can eliminate most of the performance-deteriorating effects present in each individual material.

5.4 Materials

Polydimethylsiloxane

Polydimethylsiloxane or PDMS is a polymeric compound comprised of a silicon backbone (-Si-O-) and organic side groups ($-CH_3$). It finds use in a wide range of applications such as medical device construction, lubrication, sealing and others. PDMS is a transparent and elastic material stable over a wide range of temperatures. Its non-toxic and inert nature makes it a perfect material for fabrication of biomedical devices [159]. *Figure 53* depicts the Pt-catalyzed hydrosilylation reaction, leading to cross-linking of the silicone pre-polymers, and the molecular structures of the molecules involved.

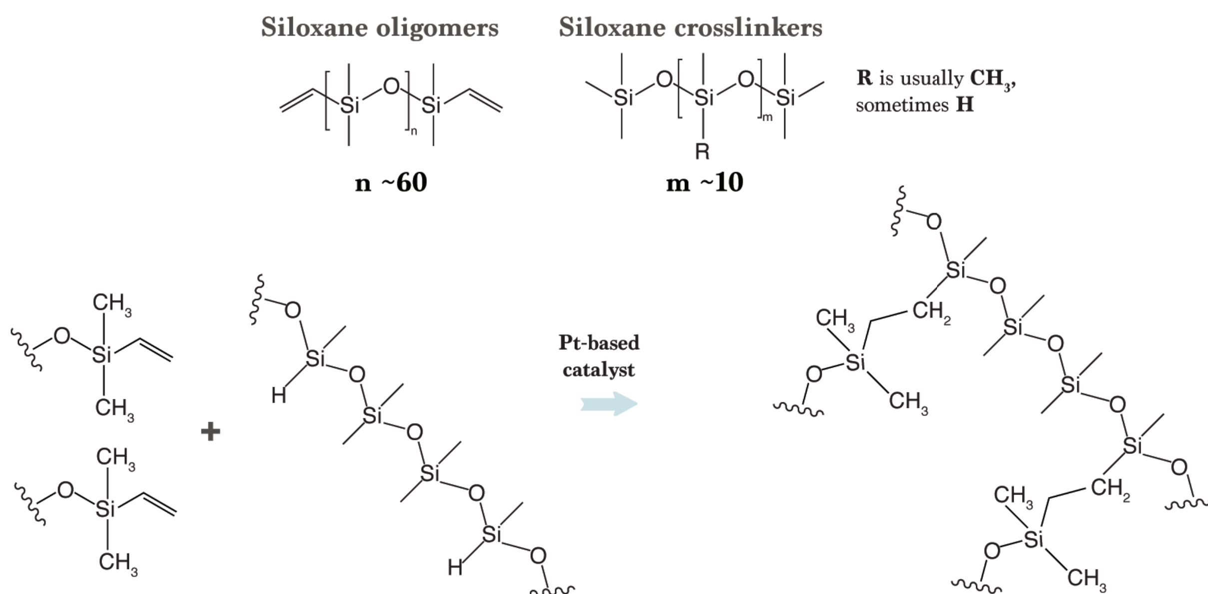

Figure 53. Formation of PDMS from silicone pre-polymers.

PDMS is a hydrophobic material. The most common approach to create a hydrophilic PDMS is to expose it to oxygen plasma. Oxygen radicals attack methyl groups ($-CH_3$) and replace them with hydroxide groups (-OH) rendering the surface hydrophilic. However, over time the hydrophilicity declines due to the fact that silanol groups (Si-OH) start to move into the bulk of the material in order to minimize the surface energy. In a similar manner two oxygen plasma-exposed PDMS slabs, or glass and PDMS, can be bonded together: hydroxide groups undergo a condensation reaction resulting in formation of Si-O-Si (*Fig. 54)*.

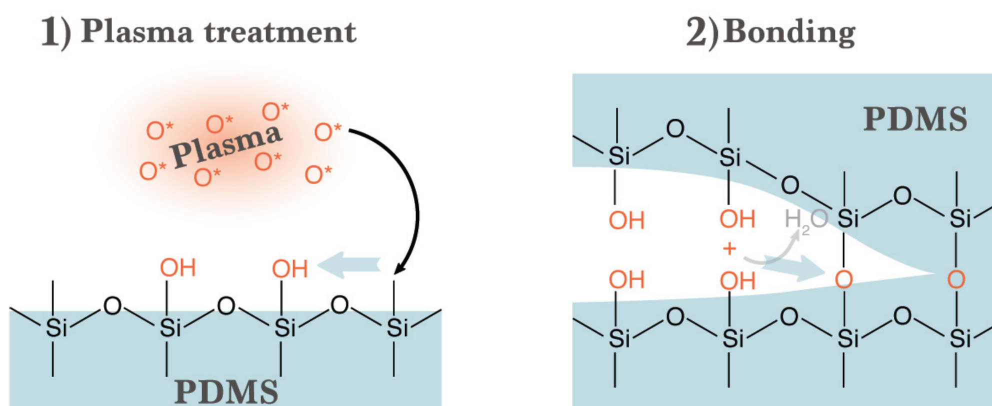

Figure 54. Schematic diagram of a chemical reaction that undergoes during the bonding of two PDMS slabs.

The preparation of PDMS is a simple process. It involves mixing of a base and a curing agent, typically, with a ratio of 10:1. The Pt catalyst required for the hydrosilylation reaction is present in the curing agent formulation. Such a reaction mixture can, after degassing, be applied onto a patterned substrate (master) and cured to form a negative replica of the pattern. In order to ease the release of PDMS, the master is usually passivated in order to avoid PDMS bonding to it. In case of Si wafers, dichlorodimethyl silane is commonly used for surface passivation. An example of the molding process (often referred to as "*soft lithography*" [160]) is shown in *figure 55*.

When designing a master mold, it is important to account for the PDMS shrinking that is due to the curing step necessary to improve the speed of cast preparation. *Table VI* lists some shrinking ratios for the 10:1 base/catalyst PDMS pre-polymer mixture [161]:

Curing temperature [˚C]	Shrinking ratio [%]
60	1.67 ± 0.06
70	1.73 ± 0.04
80	1.92 ± 0.03
100	2.28 ± 0.04

Table VI. Shrinking ratios for 10:1 PDMS mixtures cured at various temperatures.

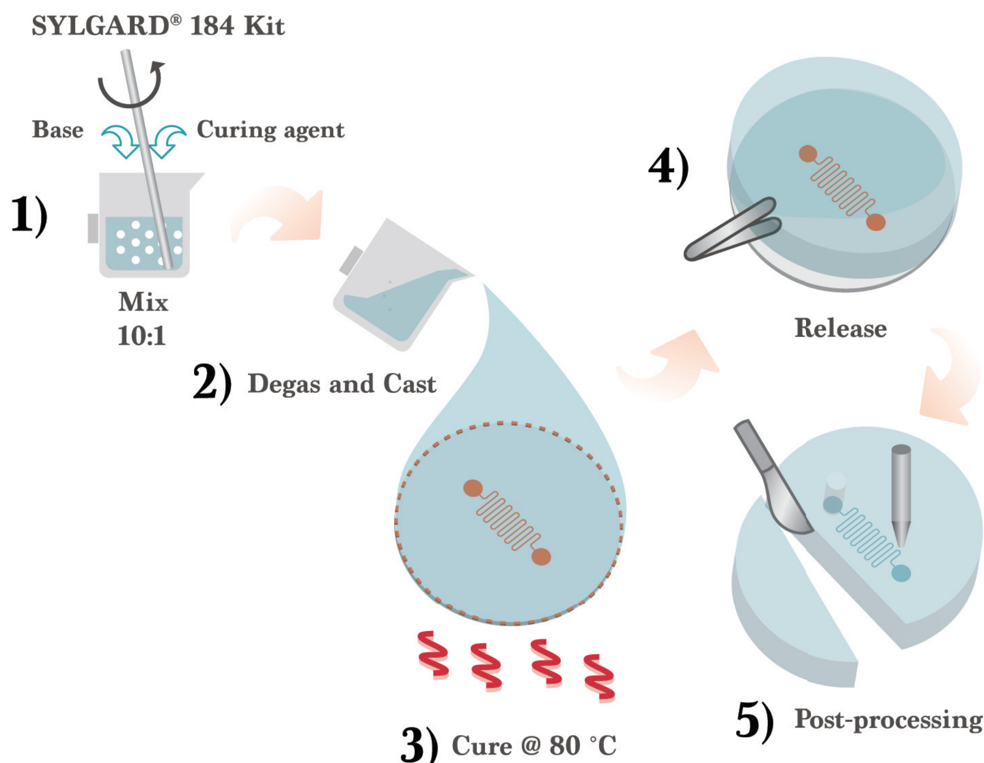

Figure 55. Schematic diagram of a PDMS casting process.

SU-8

SU-8 is a negative epoxy-based photoresist that is often used for the preparation of a master mold used in soft lithography process. Its main advantage is the low absorption coefficient for light with wavelengths above 300 nm (transparency) [162]. This allows to pattern films with a millimeter range thickness and to achieve aspect ratios of up to 20 from a single photolithographic exposure. Among other advantages is high chemical resistance, mechanical stability and biocompatibility. Its main components are SU-8 monomers (each having 8 active sites), organic solvent and a photo-acid generator (PAG). The amount of solvent controls the available film thickness. During the UV exposure, the triarylsulfonium hexafluoroantimonate salt acting as a PAG in the SU-8 resist formulation, decomposes and produces a strong acid. The produced acid is the catalyst for epoxy ring opening and cationic polymerization of SU-8 polymer. As a result, the initially low molecular weight SU-8 epoxy resin becomes densely cross-linked.

Y-cut $LiNbO_3$

A $LiNbO_3$ bulk crystal is ferroelectric and grown by means of the Czochralski process. It possesses large pyroelectricity, and shows electro-optic effects, along with a very large dielectric constant and piezoelectricity. This highly piezoelectric material shows low viscous losses and high acoustic velocities. It is a very popular material in many photonics and electro-acoustic applications, so that a big selection of various $LiNbO_3$ cuts with well-studied properties is commercially available. Due to the large piezoelectricity, these properties are very sensitive towards variations at the surface electrical boundary condition. When the rotation angle is 0˚, a very large K^2 of about 25% can be obtained at the expense of a large propagation loss from bulk diffraction. Propagation velocity of leaky SAW on this cut is about 4200 m/s, while *temperature coefficient of velocity* (TCV) is about -75 ppm/°C [32, 163].

5.5 Fabrication of SAR-integrated microfluidic devices

Fabrication of the SAW sensor component is based on *lift-off* lithography [**Paper II**]. It consists of a resist application step on a Y-cut X-propagation $LiNbO_3$ substrate and its consequent lithographic exposure to define the geometry of the resonator. 300 nm thick Ti/Au/Ti metal film stack is then e-beam evaporated into the openings of the resist forming the IDT, reflectors and contact pads. Following that, the substrate is immersed into a solvent

that dissolves the photoresist under the deposited metal, starting at the edge of the unexposed part of the film, lifting off the metal. It is important to note that the chosen deposition technique should utilize line-of-sight configuration, where a vertical material transfer occurs. This is needed to ensure the presence of a gap between the metal and a polymer, so that the solvent can access the resist wall.

To protect the IDT from corrosive and short-circuiting effects of the liquid that is being sensed, a 100 nm SiO_2 passivation layer is deposited by reactive magnetron sputtering process. Good adhesion of this film is achieved by utilizing the top Ti layer of the metallization- it forms a native Ti-TiO_2-SiO_2 interface. At the same time, the bottom Ti layer acts as an adhesion layer for the Au. Openings in the SiO_2 passivation are dry etched in a subsequent step, so that the measurement probes can be used to contact the device.

The PDMS microfluidic delivery system is fabricated using soft lithography on a SU-8 structured master mold (*Fig. 56*).

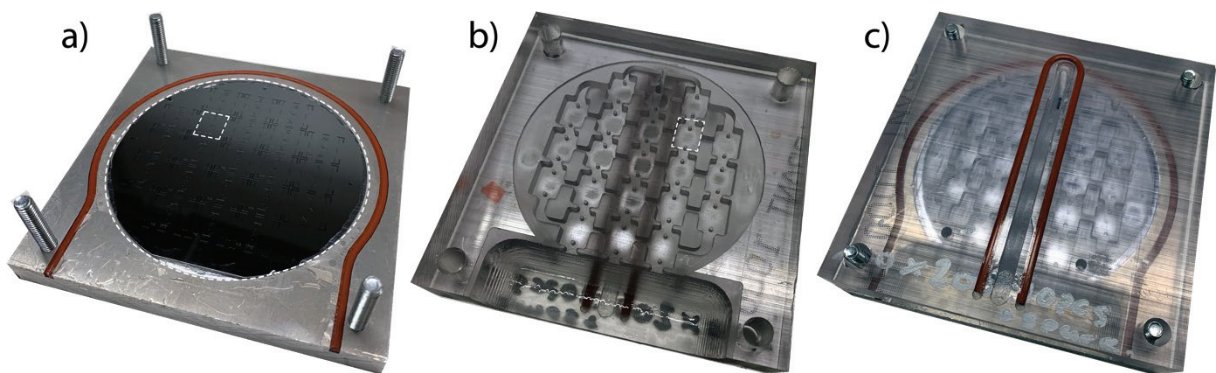

Figure 56. Photographs of the mold used for fabrication of the microfluidic system. **a)** Bottom part of the mold. Contour of the 4'master wafer is outlined with the white circle, while contour of the individual SAR chip is outlined with the white square; **b)** top part of the mold with white square outlining the PDMS microfluidic system; **c)** assembled mold.

The final step involves alignment and bonding of the fabricated components. O_2 plasma activation is performed in order to render the surfaces hydrophilic. Additionally, the bonding strength is increased through the SiO_2 passivation layer. The general outline of the fabrication process is shown schematically in *figure 57.*

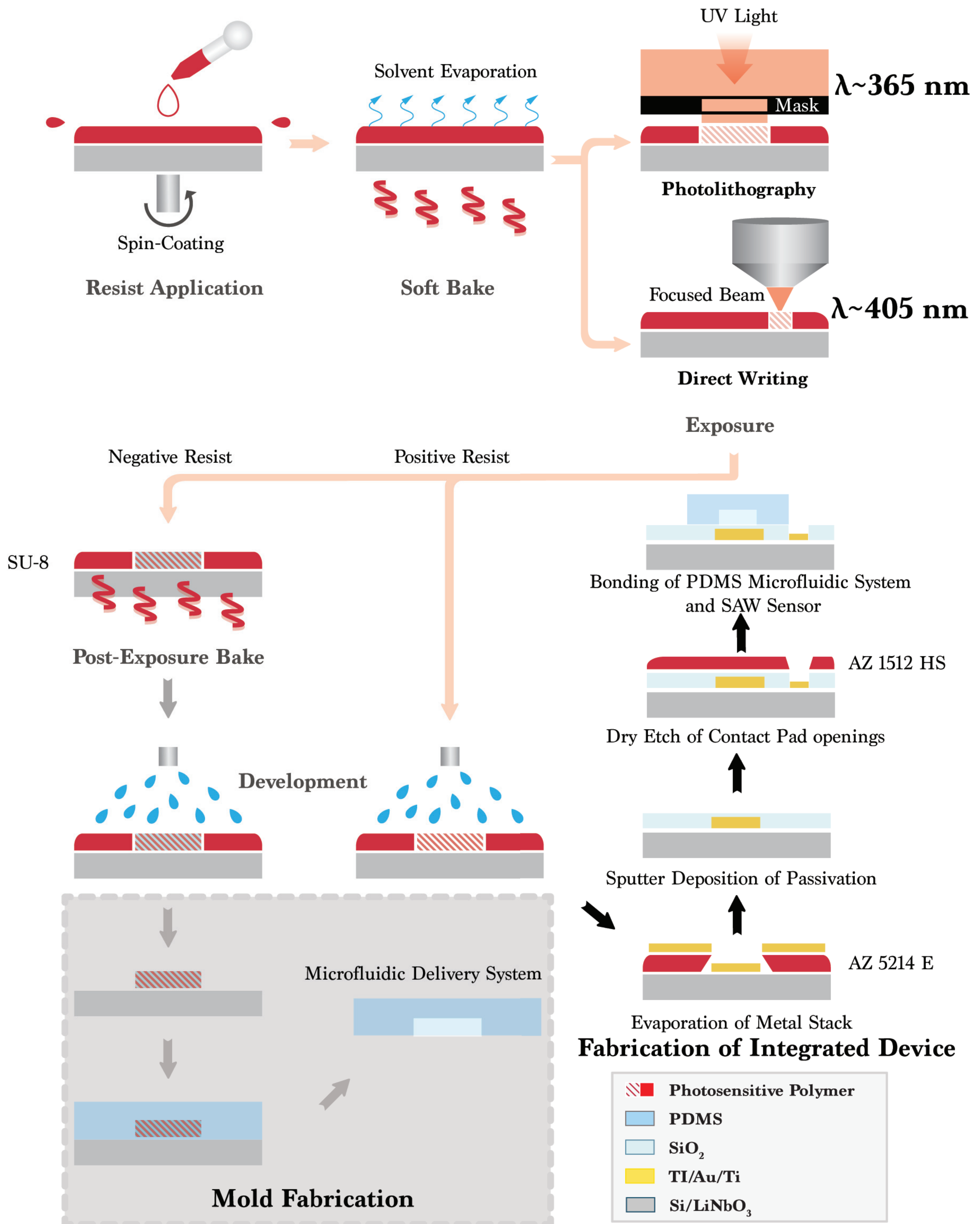

Figure 57. Fabrication process flow for the integrated microfluidic SAW resonant in-liquid sensor.

The integrated SAR-EIS sensor occupies a small area in the range of 2 mm^2 (*Fig. 58*) while the microfluidic inlets and assembly procedures required chip dimensions in the range of 1 cm^2. Accordingly, a minimal integration of about 5 SAR-EIS sensors within the same microfluidic chip with additional inlets is feasible, thus enabling the design of sensor array system within an area comparable to the space occupied by a single QCM sensor. Parallelization of sensors enables simultaneous measurement of several analytes in the same sample, or parallel measurements of the same analyte for improved reliability.

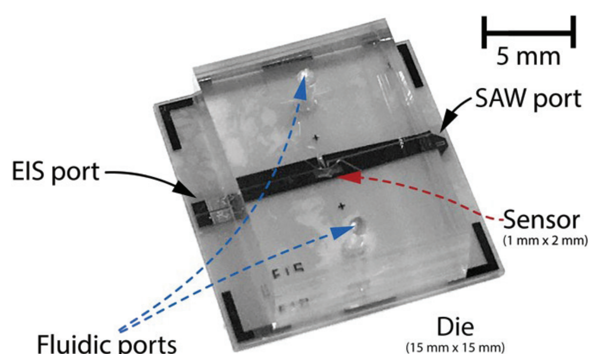

Figure 58. Photograph of the SAR-EIS tandem sensor integrated with microfluidic device. The sensor contact pads (left and right sides) are appropriately sized for interfacing with contact measurement probes.

5.6 Interfacing Considerations

It is important for a functional integrated device to have a reliable interface, both fluidic and electric, with the peripherals such as pumps, valves, tubing, and external electronic components. Sometimes these interfaces are referred as “world-to-chip”, “macro-to-micro” or “fluidic interconnect”. There is no currently existing common standard of how these interfaces should be implemented for microfabricated devices, and a variety of options exists. Among them reversible insertion of tubes or needles into inlet ports of a chip, direct contact with the surface of a device to achieve a compression seal, adhesives and monolithic integration.

An efficient fluidic interconnect has:

- Low dead volume;
- No cross-contamination of samples;
- Ability to plug and remove easily, to be reused;
- High pressure compatibility;
- Chemical inertness;

- Low cost;
- Compatibility with existing (commercially) available peripherals.

SAW-based sensors require power to operate, supplied though electrical connections. The sensing elements are patterned inside the microfluidic structures, so connection pads had to be designed to reside outside the PDMS top structure. Some examples of possible connection choices, common in many areas of *Lab-on-a-Chip* (LoC) devices, are edge connectors and sockets, pogo pins and spring-loaded contacts along with some examples of more advanced integration methods based on MEMS and microelectronics platforms.

In figure 59, the measurement setup, including a VNA measurement probe for interfacing the SAR, and a modified spring-loaded IC test clamp for interfacing the EIS connection pads, is shown. The sensor is mounted onto a temperature control stage. The setup allows for simultaneous measurement of the SAW and the EIS response. For that purpose, the IDT is probed by a VNA with a set of measurement probes. The resonance frequency and magnitude of conductance peak are determined from the device conductance obtained from the measured S_{11} parameter. The EIS port is connected to the potentiostat.

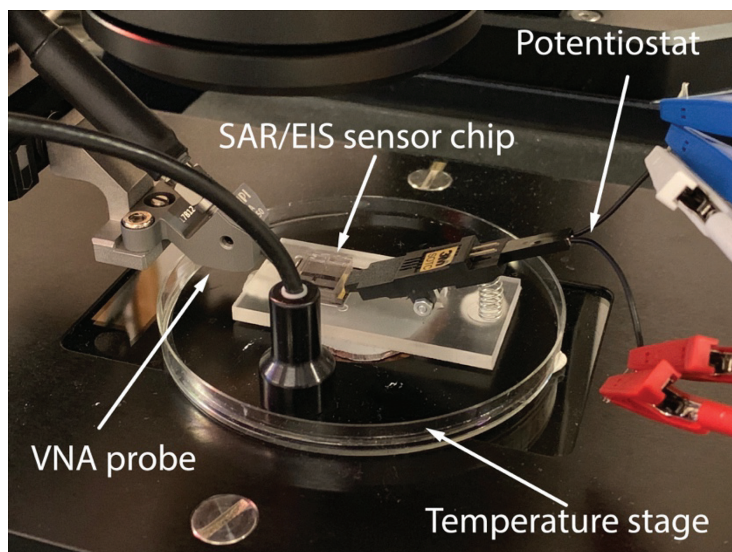

Figure 59. A photograph of measurement setup used for the sensor characterization. The sensor chip is placed under the fluorescence stereo microscope on a temperature-controlled stage in a holder that hosts necessary EIS wiring and spring-loaded contacts. On the left side, the chip is contacted with VNA probe for SAR response detection.

A much more robust test fixture is currently being developed (*Fig. 60*). It enables chip size reduction and automated measurements employing spring-loaded contacts applied

directly to the SAW and EIS ports. Nanoports are attached to the fixture, which are aligned to the microfluidic outlets of the PDMS-bonded sensor chip, in order to provide the connection to the sample delivery setup.

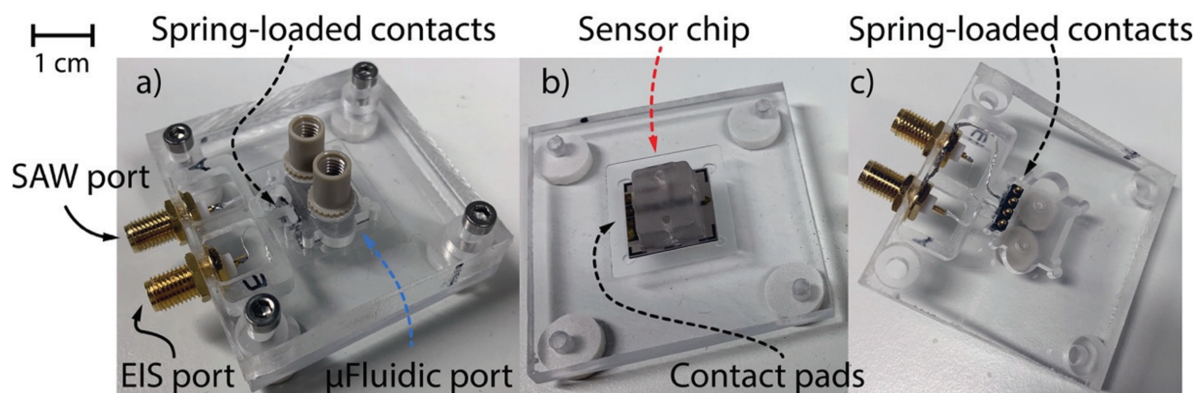

Figure 60. A photograph of the device test fixture prototype.

Additionally, some unconventional techniques for liquid interfacing can be used. For example, certain temperature compensation methods used in SAW resonators also allow to electrically decouple sensor electrodes from the liquid to prevent their short-circuiting (see section *Conclusions and Future Outlook*). As a result, complete removal of the microfluidic system becomes possible. This uniquely enables the utilization of previously developed *hydrodynamic flow confinement* (HFC) devices, referred to as *Multifunctional Pipette* or $\mu F\pi$ (original device in PDMS [164]) (*Fig. 62, 63a,c)*, and its scaled down version fabricated in the hard polymer SU-8 (*Fig. 61a,b)* [**Paper V**], for sample delivery. In HFC devices, liquids are injected and aspired simultaneously by applying positive and negative pressures to a number of channels with exits located at the tip of a probe, resulting in a recirculation, or flow confinement zone in between the device and the surface (*Fig. 61c, 63d)*. This recirculation zone is self-sustaining and can be repositioned together with the HFC device. Thus, analytes of interest can be delivered to, and collected from, the sensor surface in a selective and contact-free manner (*Fig. 63c,d)*.

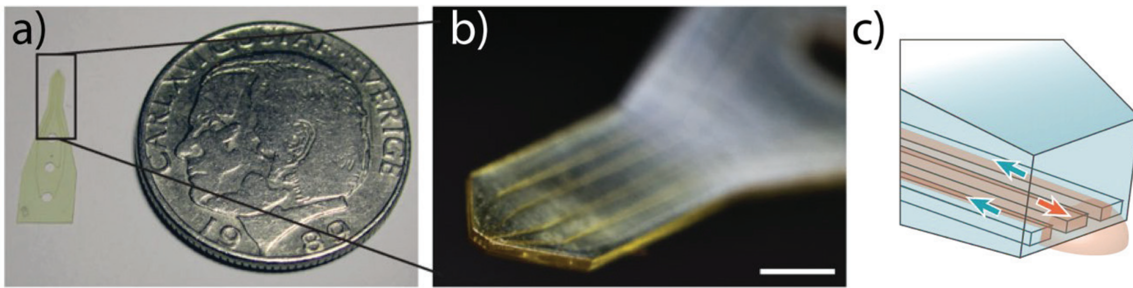

Figure 61. Photographs of SU-8 microfluidic HFC probes. **a)** A single SU-8 microfluidic device next to a coin (Ø25 mm); **b)** a close-up of the SU-8 microfluidic probe tip (scale bar represents 1 mm); c) hydrodynamically confined flow (arrows indicate the direction of liquid flow, while orange color represents positive pressure, and blue negative pressure [165].

Microfluidic HFC probes fabricated in SU-8 have a range of advantages over conventional $\mu F\pi$ made of PDMS. For instance, the switching speed of the original device was constrained because of the elastic PDMS walls. Along with that the fabrication limits of the pipette tip geometry, the manufacturing scalability of the PDMS replica molding process, the relatively large size that poses some issues in optical microscope setups, and the difficulty of integrating additional functional components, such as electrodes, were among the driving forces behind investigating the SU-8 process [165]. The proposed fabrication scheme allows for production of microfluidic open-volume superfusion devices with well-defined tip-geometry that are smaller, have better switching times, the possibility to integrate electrodes, and most importantly, and rely on standard scalable microfabrication techniques [**Paper V**]. The relative size scale of each device along with the SAR sensor is shown in *figure 62*.

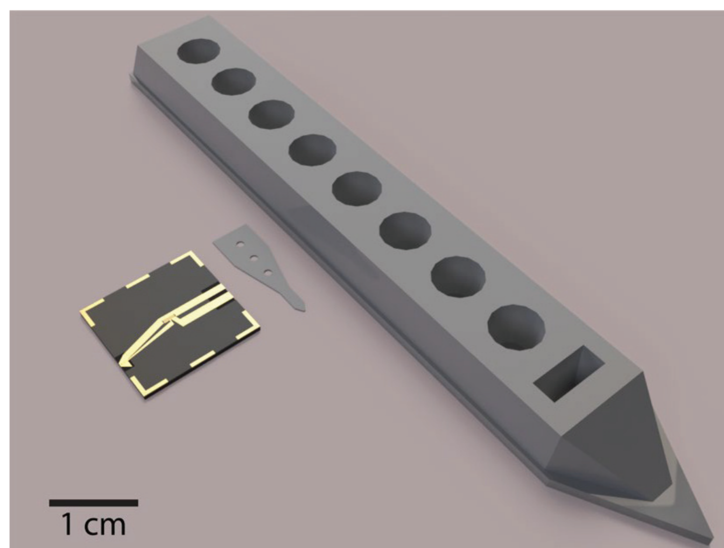

Figure 62. 3D visualization demonstrating the relative size of the devices. From left to right: SAR sensor, SU-8 microfluidic probe, and PDMS microfluidic device with integrated sample wells.

6 CONCLUSIONS AND FUTURE OUTLOOK

A new concept for lab-on-a-chip in-liquid sensing, employing integration of surface acoustic wave resonance (SAR) in a one-port configuration with a soft polymer microfluidic sample delivery system, has been developed, practically demonstrated, and discussed. The sensor has a small footprint of < 2 mm^2, operates at a frequency of 185 MHz and has shown a comparable sensitivity to other SAW liquid-phase sensors, while offering a *quality factor* (Q) value in water of about 250, low impedance, and fairly low susceptibility to viscous damping.

The device has potential for analytical assays of microorganisms, biomacromolecules, particles and supramolecular structures. The initial proof-of-principle study evaluated the sensor response to the deposition of a lipid bilayer in the sensing cavity, and subsequent binding of functionalized nanoparticles to the layer or addition of transformations-inducing Ca^{2+} ions. Future work includes the development of bioassays for proteins, DNA and other analytes relevant to human health.

The chosen substrate crystal cut provides a possibility to integrate microfluidic mixers based on Rayleigh SAW that propagates towards the Z-axis of the substrate. These can be employed in rapid mixing of diffusion-limited laminar flows inside microfluidic channels of the same chip, facilitating the assay chemistry, or for particle sorting and focusing.

The low impedance at resonance allowed for a sensor design with a reduced number of strips in the IDT to be implemented, effectively confining more acoustic energy in the reflectors area. The *LEC* design concept for a SAR in-liquid sensor has been demonstrated and its performance experimentally characterized. The acoustic wave confinement led to a sensitivity increase of >100%, which was determined by loading the sensor with a series of solutions of different $\rho\eta$. Time-resolved measurements of the sensor response confirmed stable operation with a limit of frequency detection of $3\sigma < 1.5$ ppm, and the limit of conductance magnitude detection to be below 30 ppm. At anti-resonance, the SAW is strongly localized under the IDT, and exhibits a 2.3 times smaller mass-sensitivity as compared to resonance, while exhibiting similar thermal drift. This can be utilized for further improvement of the noise characteristics by canceling out thermal fluctuations in the measurement. The measured temperature coefficient of the resonance frequency was found to be −83 ppm K^{-1}, while the antiresonance frequency demonstrated a temperature dependence of about −72 ppm K^{-1}. These numbers are typical for the $LiNbO_3$ substrate and need to be reduced to improve upon the limit of quantification/detection. It is expected that reducing the *temperature coefficient of frequency* (TCF) will lead to a further significant reduction in measurement uncertainties. One simple way to achieve this would potentially be the subtraction of resonance from antiresonance frequencies. They exhibit close similarities in thermal response, while the difference in mass-sensitivity is remarkably large. Signal

subtraction reduces the thermal sensitivity to −11 ppm K^{-1}, while retaining a significant mass sensitivity. In a measurement environment with 0.1K temperature tolerance, this translates in to a maximum of −1.1 ppm frequency shift, which is comparable to the noise level. More elaborate frequency subtraction techniques can readily eliminate the first order TCF in the sensor response.

Alternatively, the compensation of the thermal drift can be achieved by adding a SiO_2 layer of about 0.3λ thickness [166]. This technique has the additional advantage to electrically decouple the electrodes from the liquid and thus enable a robust SAR sensor design, where the IDT does not need to be separated from the liquid environment by a cavity. Theoretical estimations show that the effect of electrical short-circuiting on the surface of the SAR grating is a frequency downshift of about –1000 ppm, while short-circuiting of the surface of the 0.3λ thick SiO_2/Au strips/$LiNbO_3$ composite is expected to induce a change of less than $\pm$0.3 ppm. Accordingly, SAR sensors with either an electrically screened or open-circuit top surface can be produced without any sacrifice in device performance, while enabling efficient compensation of the SAR thermal drift, and simplifying the microfluidic circuitry.

The proposed sensor design uniquely enables integration with low frequency impedance spectroscopy by placing the reflective gratings in an interdigitated fashion, thus enabling electrical measurement of the complex electrical impedance near the sensing surface, which is independent from the acoustic resonance. Operation of a combined surface acoustic resonance and impedimetric sensor within the confines of a single sensor die was successfully demonstrated. The sensor was designed in a tandem arrangement, in which both sensing circuits physically share surface printed components but are operated in different frequency ranges through two electrical interface ports. The proposed integration SAR-EIS scheme demonstrates crosstalk below -60 dB and enhanced sensitivities towards particle and molecular film deposits at the sensing surface. The obtained multiparametric sensor response provides a first impression of the rich information that can be acquired by a tandem sensor. The SAW and the EIS responses are not only complementary in view of detecting the nature of the molecular layer structures and their properties, but also provided insights into possibilities for further improvement of the sensor figures of merit. Additional optimization of the microfluidic system design and IDT itself is feasible in order to obtain better resonance characteristics.

Figure 63 demonstrates conceptual drawings of some possible applications of the sensor to the $\mu F\pi$ concept. On a side note, the same solutions multiplexing mechanism as presented in [164] can be used to implement *on-chip sample switching* when applied to the SAR device.

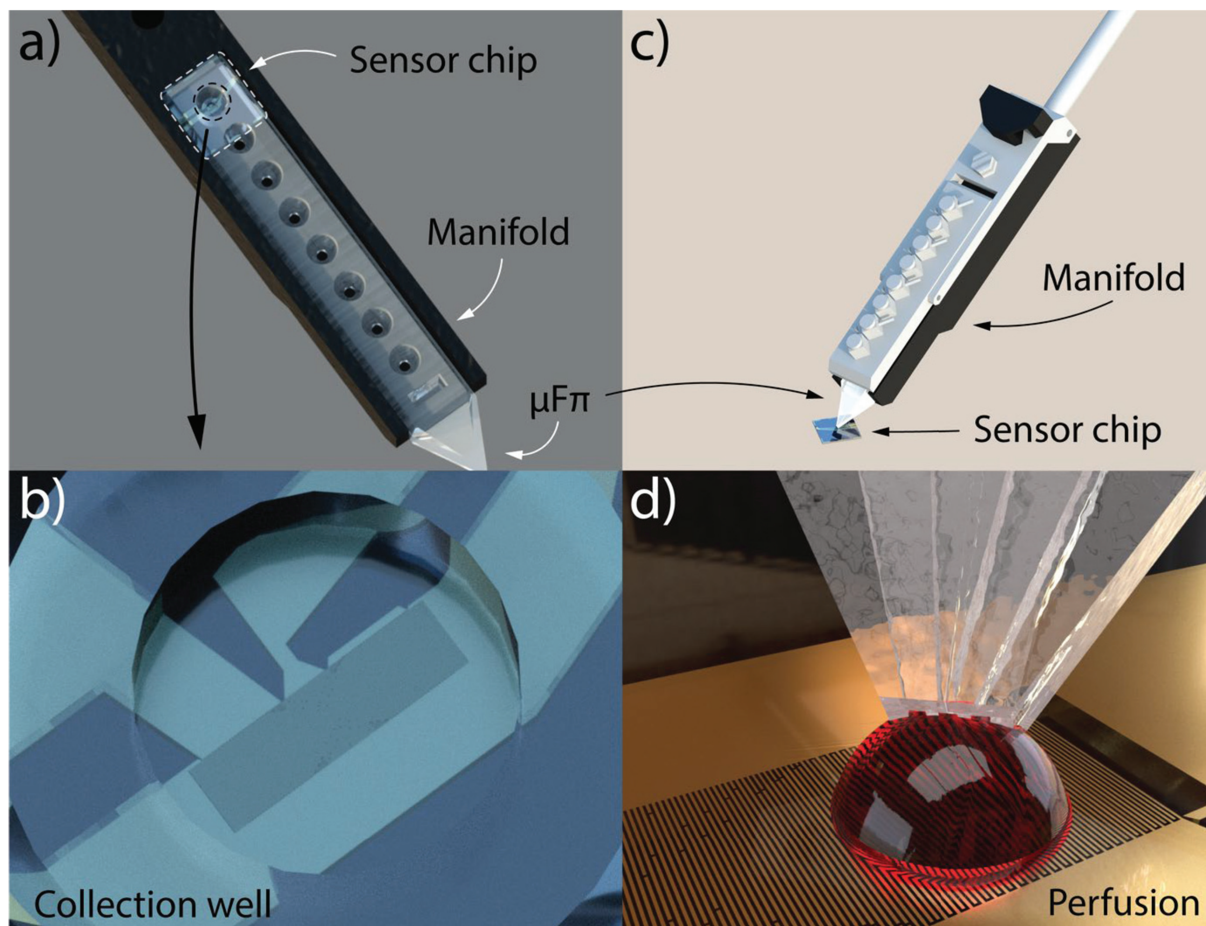

Figure 63*.* Image of the SAR-EIS sensor used along with the *µFπ* system*.* Figures **(a-b)** demonstrate the sensor being installed under one of the *collection wells* for subsequent analysis of an analyte. Figures **(c-d)** demonstrate the sensor being used as a functional surface for *sample perfusion*, utilizing the miniaturized hard polymer probe developed in paper V.

To conclude, the SAR approach demonstrates high potential in view of the possibility to develop a truly versatile lab-on-a-chip sensing platform technology by integrating the functionalities of other SAW techniques, impedance spectroscopy and optical microscopy.

7 SUMMARY OF APPENDED PAPERS

[Paper I]

Design and Characterization of Surface Acoustic Wave Resonance (SAR) System for In-liquid Sensing

In this paper, sensor designs with clearly pronounced resonances and minimum spurious responses were identified. This study pointed out that resonators with the hiccup IDT topology can tolerate the spurious content introduced by the microfluidic system. Initial studies in liquids have shown that the device sensitivity is comparable to other electro-acoustic technologies, with further improvements made possible through the refined design.

[Paper II]

A High-performance Lab-on-a-chip Liquid Sensor Employing Surface Acoustic Wave Resonance

In this paper, a new concept for lab-on-a-chip liquid-phase sensing is demonstrated by integration of surface acoustic wave resonator in a one-port configuration with a soft polymer microfluidic delivery system. Sensor design, fabrication, implementation, and characterization using liquid medium and affinity assay were demonstrated. The SAR sensing platform has low impedance at resonance, a retained Q when immersed in liquid, the ability to work under highly viscous load with minimum performance degradation, and reduced dimensions as compared to conventional high frequency sensors.

[Paper III]

A High-performance Lab-on-a-chip Liquid Sensor Employing Surface Acoustic Wave Resonance: Part II

In this paper, a novel 'lateral energy confinement' (LEC) reflector design was introduced to the SAR sensor. An improvement in mass-sensitivity greater than 100% at resonance was achieved. The paper presents the thorough characterisation of the sensing capabilities that

were not discussed in part I of the work, including: the noise characteristics of the sensor, the time resolved measurements, the ability of the senor to recover back to the baseline. Two complementary sensing parameters were studied, the shift of resonance frequency and the shift of conductance magnitude at resonance, by means of a biomembrane-nanoparticle assay and 2D-fluidic molecular films.

[Paper IV]

A Microfluidics-integrated Impedance/Surface Acoustic Resonance Tandem Sensor

In this paper, we demonstrate further improvements in sensor capabilities by integrating electrochemical impedance spectroscopy into the existing SAR platform. The two-port sensor design was demonstrated and subsequently characterized. The SAR-EIS tandem sensor features low cross-talk between SAR and EIS ports, enabling non-interfering gravimetric and impedimetric measurements. The SAW and the EIS responses are not only complementary in view of detecting the nature of the molecular layer structures and their properties, but also provided a unique and detailed description of physicochemical surface phenomena as compared to a single-mode sensing routine.

[Paper V]

SU-8 free-standing microfluidic probes

In this paper, we demonstrate a process for fabricating free-standing microfluidic probes in SU-8. These probes allow for direct and localized delivery of sample to the sensor surface. The described process allows for facile production of batches of microfluidic open-volume superfusion devices with well-defined tip-geometry that compares favourably to PDMS processes and devices in terms of effort and required fabrication time, and particularly in applications variety.

ACKNOWLEDGMENT

This thesis would never be possible without the people I have worked with during the course of my PhD studies. I would like to express my sincere gratitude to the following people:

First and foremost, I would like to thank my supervisor Professor **Aldo Jesorka** for his endless enthusiasm, great discussions and advice. Thank you for believing in me and giving me this opportunity!

My co-supervisor, Dr. **Ventsislav Yantchev**. Ventsi, without your help none of these activities would be possible. Thank you for taking your time to share your extensive knowledge with me, awesome conversations and the sense of humor.

My examiner, Professor **Dag Winkler** for the support and the input on my work.

Professors **Nina Kann** and **Per Lincoln** for their invaluable support!

My co-authors, for great collaborations and contributions: **Alar**, **Gavin, Anna**, **Vladimir**, **Tanya**, **Mehrnaz**, **Sobhan** and **Alexei**.

Irep for her contributions and support.

My friends at Chalmers: **Evgenii**, **Bella**, **Silver**, **Emanuele** and **Emelie**.

All staff at the Nanofabrication laboratory for their assistance and helpful advice, and especially **Henrik Frederiksen** for the help and time spent on the new sputtering equipment.

I would like to say a special thank you to **Aleksandra Małko**, **Alex Shchupak, Maciej Kaniecki** and **Andreas Tag** for their support!

Last, but not least, I would like to thank my **family** for their support, understanding and love.

This work was financially supported by the European Research Council (ERC) (Horizon 2020 FET Open research grant, Project ID: 664786), and the Swedish Strategic Research Foundation (SSF).

Bibliography

1. Ding, X., et al., *Surface acoustic wave microfluidics.* Lab on a Chip, 2013. **13**(18): p. 3626-3649.
2. Ruppel, C.C.W., L. Reindl, and R. Weigel, *SAW devices and their wireless communications applications.* Ieee Microwave Magazine, 2002. **3**(2): p. 65-71.
3. Tanski, W.J., *SURFACE ACOUSTIC-WAVE RESONATORS ON QUARTZ.* Ieee Transactions on Sonics and Ultrasonics, 1979. **26**(2): p. 93-104.
4. Tonami, S., A. Nishikata, and Y. Shimizu, *CHARACTERISTICS OF LEAKY SURFACE ACOUSTIC-WAVES PROPAGATING ON LINBO3 AND LITAO3 SUBSTRATES.* Japanese Journal of Applied Physics Part 1-Regular Papers Short Notes & Review Papers, 1995. **34**(5B): p. 2664-2667.
5. Kawachi, O., et al., *Optimal cut for leaky SAW on LiTaO3 for high performance resonators and filters.* Ieee Transactions on Ultrasonics Ferroelectrics and Frequency Control, 2001. **48**(5): p. 1442-1448.
6. Kadota, M. and S. Tanaka, *HAL SAW Resonators Using 42°YX-LiTaO3 Thin Plate on Quartz Substrate.* 2017 European Frequency and Time Forum (Eftf), 2017.
7. Gomi, M., et al., *High-coupling leaky surface acoustic waves on LiNbO3 or LiTaO3 thin plate bonded to high-velocity substrate.* Japanese Journal of Applied Physics, 2017. **56**(7): p. 7.
8. Gomi, M., et al., *High-coupling leaky surface acoustic waves on LiNbO3 or LiTaO3 thin plate bonded to high-velocity substrate.* Japanese Journal of Applied Physics, 2017. **56**(7).
9. Takai, T., et al., *Incredible High Performance SAW resonator on Novel Multi-layerd Substrate*, in *2016 Ieee International Ultrasonics Symposium*. 2016, Ieee: New York.
10. Suzaki, H., et al., *ST-quartz/LiTaO3 Direct Bonding Using SiO2 Amorphous Layers with VUV/O-3 Pre-treatment for a Novel 5G Surface Acoustic Wave Device.* 2016 International Conference on Electronics Packaging (ICEP), 2016: p. 443-446.
11. Kadota, M., et al., *Suprious-Free, Near-Zero-TCF Hetero Acoustic Layer (HAL) SAW Resonators Using LiTaO3 Thin Plate on Quartz*, in *2018 Ieee International Ultrasonics Symposium*. 2018, Ieee: New York.
12. Kadota, M. and S. Tanaka, *Wideband acoustic wave resonators composed of hetero acoustic layer structure.* Japanese Journal of Applied Physics, 2018. **57**(7).
13. Mahon, S., *The 5G Effect on RF Filter Technologies.* Ieee Transactions on Semiconductor Manufacturing, 2017. **30**(4): p. 494-499.
14. Katardjiev, I. and V. Yantchev, *Recent developments in thin film electro-acoustic technology for biosensor applications.* Vacuum, 2012. **86**(5): p. 520-531.
15. DeMiguel-Ramos, M., et al., *Gravimetric biosensor based on a 1.3 GHz AlN shear-mode solidly mounted resonator.* Sensors and Actuators B-Chemical, 2017. **239**: p. 1282-1288.
16. Wingqvist, G., et al., *Shear mode AlN thin film electro-acoustic resonant sensor operation in viscous media.* Sensors and Actuators B-Chemical, 2007. **123**(1): p. 466-473.

17. Nirschl, M., et al., *CMOS-Integrated Film Bulk Acoustic Resonators for Label-Free Biosensing.* Sensors, 2010. **10**(5): p. 4180-4193.
18. Hoffmann, R., M. Schreiter, and J. Heitmann, *The concept of thin film bulk acoustic resonators as selective CO2 gas sensors.* Journal of Sensors and Sensor Systems, 2017. **6**(1): p. 87-96.
19. Mirea, T., E. Iborra, and V. Yantchev, *S-0 Lamb wave resonators for in-liquid sensing: promising alternative to shear bulk acoustic wave devices.* 2016 European Frequency and Time Forum (Eftf), 2016.
20. Mirea, T. and V. Yantchev, *Influence of liquid properties on the performance of S-0-mode Lamb wave sensors: A theoretical analysis.* Sensors and Actuators B-Chemical, 2015. **208**: p. 212-219.
21. Mirea, T., et al., *Influence of liquid properties on the performance of S-0-mode Lamb wave sensors II: Experimental validation.* Sensors and Actuators B-Chemical, 2016. **229**: p. 331-337.
22. Luka, G., et al., *Microfluidics Integrated Biosensors: A Leading Technology towards Lab-on-a-Chip and Sensing Applications.* Sensors (Basel), 2015. **15**(12): p. 30011-31.
23. Go, D.B., et al., *Surface acoustic wave devices for chemical sensing and microfluidics: a review and perspective.* Analytical Methods, 2017. **9**(28): p. 4112-4134.
24. Fu, Y.Q., et al., *Recent developments on ZnO films for acoustic wave based bio-sensing and microfluidic applications: a review.* Sensors and Actuators B-Chemical, 2010. **143**(2): p. 606-619.
25. Fu, Y.Q., et al., *Advances in piezoelectric thin films for acoustic biosensors, acoustofluidics and lab-on-chip applications.* Progress in Materials Science, 2017. **89**: p. 31-91.
26. Jeffries, G.D.M., et al., *Open Volume Microfluidic Probes*, in *Compendium Of In Vivo Monitoring In Real-time Molecular Neuroscience - Volume 2: Microdialysis And Sensing Of Neural Tissues*. 2017, World Scientific Publishing Company. p. 291-320.
27. Teh, S.Y., et al., *Droplet microfluidics.* Lab on a Chip, 2008. **8**(2): p. 198-220.
28. Tiller, B., et al., *Frequency dependence of microflows upon acoustic interactions with fluids.* Physics of Fluids, 2017. **29**(12): p. 122008.
29. Winkler, A., et al., *Towards efficient surface acoustic wave (SAW)-based microfluidic actuators.* Sensors and Actuators a-Physical, 2016. **247**: p. 259-268.
30. Rayleigh, L., *On Waves Propagated along the Plane Surface of an Elastic Solid.* Proceedings of the London Mathematical Society, 1885. **s1-17**(1): p. 4-11.
31. Auld, B.A., *Acoustic fields and waves in solids*. 1973: Wiley.
32. Hashimoto, K.Y., *Surface Acoustic Wave Devices in Telecommunications: Modelling and Simulation*. 2013: Springer Berlin Heidelberg.
33. Rosenbaum, J., *Bulk Acoustic Wave Theory and Devices*. 1988: Artech House.
34. Morgan, D., *Surface Acoustic Wave Filters: With Applications to Electronic Communications and Signal Processing*. 2010: Elsevier Science.
35. Curie, J. and P. Curie, *Development, via compression, of electric polarization in hemihedral crystals with inclined faces.* Bulletin de la Societe de Minerologique de France, 1880(3): p. 90-93.
36. Heywang, W., K. Lubitz, and W. Wersing, *Piezoelectricity: Evolution and Future of a Technology*. 2008: Springer Berlin Heidelberg.
37. Cady, W., Guyton., *The piezoelectric resonator.* Physical Review A, 1921(17): p. 531-3.

38. Gautschi, G., *Piezoelectric Sensorics: Force Strain Pressure Acceleration and Acoustic Emission Sensors Materials and Amplifiers*. 2013: Springer Berlin Heidelberg.
39. Green, G., *On the propagation of light in crystallized media.* Transactions of the Cambridge philosophical society, 1839.
40. Christoffel, E., B., *Sur une classe particuliere de fonctions entieres et de fractions continues.* Annali di Matematica Pura ed Applicata, 1877. **8**(2): p. 1-10.
41. Kino, G.S., *Acoustic waves: devices, imaging, and analog signal processing*. 1987: Prentice Hall PTR.
42. Lewis, M., *Surface Skimming Bulk Waves - Ssbw.* Ieee Transactions on Sonics and Ultrasonics, 1978. **25**(4): p. 256-256.
43. Bleustein, J.L., *A New Surface Wave in Piezoelectric Materials.* Applied Physics Letters, 1968. **13**(12): p. 412.
44. Gulyaev, Y.V., *Electroacoustic Surface Waves in Solids.* Jetp Letters-Ussr, 1969. **9**(1): p. 37-&.
45. Love, A.E.H., *Some Problems of Geodynamics: Being an Essay to which the Adams Prize in the University of Cambridge was Adjudged in 1911*. 1911: University Press.
46. Rocha, M.I.G., et al., *Love Wave Biosensors: A Review*, in *State of the Art in Biosensors - General Aspects*. 2013.
47. Sinha, B.K. and H.F. Tiersten, *An Analysis of Transverse-Modes in Acoustic Surface-Wave Resonators.* Journal of Applied Physics, 1980. **51**(6): p. 3099-3112.
48. Hashimoto, K., et al., *Optimum leaky-SAW cut of LiTaO3 for minimised insertion loss devices*. 1997 Ieee Ultrasonics Symposium Proceedings, Vols 1 & 2, ed. S.C. Schneider, M. Levy, and B.R. McAvoy. 1997. 245-254.
49. Shimizu, H., Y. Suzuki, and T. Kanda, *LOVE-TYPE-SAW RESONATOR OF SMALL SIZE WITH VERY LOW CAPACITANCE RATIO AND ITS APPLICATION TO VCO*. Ieee 1990 Ultrasonics Symposium : Proceedings, Vols 1-3, ed. B.R. McAvoy. 1990. 103-108.
50. Lamb, H., *On waves in an elastic plate.* Proceedings of the Royal Society of London Series a-Containing Papers of a Mathematical and Physical Character, 1917. **93**(648): p. 114-128.
51. Caliendo, C. and M. Hamidullah, *Guided acoustic wave sensors for liquid environments.* Journal of Physics D-Applied Physics, 2019. **52**(15).
52. Stoneley, R., *Elastic waves at the surface of separation of two solids.* Proceedings of the Royal Society of London Series a-Containing Papers of a Mathematical and Physical Character, 1924. **106**(738): p. 416-428.
53. White, R.M. and F.W. Voltmer, *Direct Piezoelectric Coupling to Surface Elastic Waves.* Applied Physics Letters, 1965. **7**(12): p. 314-&.
54. Madou, M.J., *From MEMS to Bio-MEMS and Bio-NEMS: Manufacturing Techniques and Applications*. 2011: CRC Press.
55. Crisp, J.J. and J.S. Heeks, *Code Generation with Saw Tapped Delay-Lines.* Electronics Letters, 1973. **9**(10): p. 239-240.
56. Mason, W.P., *Physical Acoustics: Principles and Methods*. 1964: Academic Press.
57. Hoang, T., *SAW Parameters Analysis and Equivalent Circuit of SAW Device*, in *Acoustic Waves - From Microdevices to Helioseismology*, M.G. Beghi, Editor. 2011, IntechOpen.
58. ROYER, D., S.N. Lyle, and E. Dieulesaint, *Elastic Waves in Solids II: Generation, Acousto-optic Interaction, Applications*. 1999: Springer Berlin Heidelberg.

59. Feld, D.A., et al., *After 60 Years: A New Formula for Computing Quality Factor is Warranted*, in *2008 Ieee Ultrasonics Symposium, Vols 1-4 and Appendix*. 2008. p. 431-+.
60. Lakin, K.M., *Thin film resonator technology.* Ieee Transactions on Ultrasonics Ferroelectrics and Frequency Control, 2005. **52**(5): p. 707-716.
61. Bode, H.W., *Network Analysis and Feedback Amplifier Design*. 1945: Van Nostrand.
62. Ruby, R., et al., *Method of Extracting Unloaded Q Applied Across Different Resonator Technologies*, in *2008 Ieee Ultrasonics Symposium, Vols 1-4 and Appendix*. 2008. p. 1815-1818.
63. Pozar, D.M., *Microwave Engineering*. 2012: Wiley.
64. Koskela, J., et al., *Acoustic loss mechanisms in leaky SAW resonators on lithium tantalate.* Ieee Transactions on Ultrasonics Ferroelectrics and Frequency Control, 2001. **48**(6): p. 1517-1526.
65. Whitesides, G.M., *The origins and the future of microfluidics.* Nature, 2006. **442**(7101): p. 368-373.
66. Bruus, H., *Theoretical Microfluidics*. 2008: OUP Oxford.
67. Stone, H.A., A.D. Stroock, and A. Ajdari, *Engineering flows in small devices: Microfluidics toward a lab-on-a-chip.* Annual Review of Fluid Mechanics, 2004. **36**: p. 381-411.
68. Ballantine, D.S., et al., *Acoustic Wave Sensors: Theory, Design and Physico-Chemical Applications*. 1996: Elsevier Science.
69. Grate, J.W. and M.H. Abraham, *SOLUBILITY INTERACTIONS AND THE DESIGN OF CHEMICALLY SELECTIVE SORBENT COATINGS FOR CHEMICAL SENSORS AND ARRAYS.* Sensors and Actuators B-Chemical, 1991. **3**(2): p. 85-111.
70. Benes, E., et al., *SENSORS BASED ON PIEZOELECTRIC RESONATORS.* Sensors and Actuators a-Physical, 1995. **48**(1): p. 1-21.
71. Pang, W., et al., *Piezoelectric microelectromechanical resonant sensors for chemical and biological detection.* Lab on a Chip, 2012. **12**(1): p. 29-44.
72. Rodahl, M., F. Hook, and B. Kasemo, *QCM operation in liquids: An explanation of measured variations in frequency and Q factor with liquid conductivity.* Analytical Chemistry, 1996. **68**(13): p. 2219-2227.
73. Kanazawa, K.K. and J.G. Gordon, *Frequency of a Quartz Microbalance in Contact with Liquid.* Analytical Chemistry, 1985. **57**(8): p. 1770-1771.
74. Martin, S.J., V.E. Granstaff, and G.C. Frye, *CHARACTERIZATION OF A QUARTZ CRYSTAL MICROBALANCE WITH SIMULTANEOUS MASS AND LIQUID LOADING.* Analytical Chemistry, 1991. **63**(20): p. 2272-2281.
75. Rodahl, M., et al., *QUARTZ-CRYSTAL MICROBALANCE SETUP FOR FREQUENCY AND Q-FACTOR MEASUREMENTS IN GASEOUS AND LIQUID ENVIRONMENTS.* Review of Scientific Instruments, 1995. **66**(7): p. 3924-3930.
76. Sauerbrey, G., *VERWENDUNG VON SCHWINGQUARZEN ZUR WAGUNG DUNNER SCHICHTEN UND ZUR MIKROWAGUNG.* Zeitschrift Fur Physik, 1959. **155**(2): p. 206-222.
77. Vig, J.R., *ON ACOUSTIC SENSOR SENSITIVITY.* Ieee Transactions on Ultrasonics Ferroelectrics and Frequency Control, 1991. **38**(3): p. 311-311.
78. Yantchev, V., et al., *Thin-film zero-group-velocity Lamb wave resonator.* Applied Physics Letters, 2011. **99**(3).

79. Caliendo, C. and M. Hamidullah, *Zero-group-velocity acoustic waveguides for high-frequency resonators.* Journal of Physics D-Applied Physics, 2017. **50**(47).
80. Sato, T., et al., *SHEAR HORIZONTAL ACOUSTIC PLATE MODE VISCOSITY SENSOR.* Japanese Journal of Applied Physics Part 1-Regular Papers Brief Communications & Review Papers, 1993. **32**(5B): p. 2392-2395.
81. Dejous, C., et al., *A SHEAR-HORIZONTAL ACOUSTIC PLATE MODE (SH-APM) SENSOR FOR BIOLOGICAL MEDIA.* Sensors and Actuators B-Chemical, 1995. **27**(1-3): p. 452-456.
82. Josse, F., et al., *On the mass sensitivity of acoustic-plate-mode sensors.* Sensors and Actuators a-Physical, 1996. **53**(1-3): p. 243-248.
83. McHale, G., *Generalized concept of shear horizontal acoustic plate mode and Love wave sensors.* Measurement Science and Technology, 2003. **14**(11): p. 1847-1853.
84. Martin, S.J., et al., *CHARACTERIZATION OF SH ACOUSTIC PLATE MODE LIQUID SENSORS.* Sensors and Actuators, 1989. **20**(3): p. 253-268.
85. Zhang, H. and E.S. Kim, *Micromachined acoustic resonant mass sensor.* Journal of Microelectromechanical Systems, 2005. **14**(4): p. 699-706.
86. Weber, J., et al., *Shear mode FBARs as highly sensitive liquid biosensors.* Sensors and Actuators a-Physical, 2006. **128**(1): p. 84-88.
87. Wohltjen, H. and R. Dessy, *Surface Acoustic-Wave Probes for Chemical-Analysis .2. Gas-Chromatography Detector.* Analytical Chemistry, 1979. **51**(9): p. 1465-1470.
88. Mujahid, A. and F.L. Dickert, *Surface Acoustic Wave (SAW) for Chemical Sensing Applications of Recognition Layers.* Sensors (Basel), 2017. **17**(12).
89. Rocha-Gaso, M.I., et al., *Surface Generated Acoustic Wave Biosensors for the Detection of Pathogens: A Review.* Sensors, 2009. **9**(7): p. 5740-5769.
90. Agostini, M., G. Greco, and M. Cecchini, *A Rayleigh surface acoustic wave (R-SAW) resonator biosensor based on positive and negative reflectors with sub-nanomolar limit of detection.* Sensors and Actuators B-Chemical, 2018. **254**: p. 1-7.
91. Harding, G.L., et al., *Love wave acoustic immunosensor operating in liquid.* Sensors and Actuators a-Physical, 1997. **61**(1-3): p. 279-286.
92. Assouar, M.B., P. Kirsch, and P. Alnot, *New Love wave liquid sensor operating at 2 GHz using an integrated micro-flow channel.* Measurement Science and Technology, 2009. **20**(9).
93. Gizeli, E., et al., *A NOVEL LOVE-PLATE ACOUSTIC SENSOR UTILIZING POLYMER OVERLAYERS.* Ieee Transactions on Ultrasonics Ferroelectrics and Frequency Control, 1992. **39**(5): p. 657-659.
94. Du, J., et al., *A study of love-wave acoustic sensors.* Sensors and Actuators a-Physical, 1996. **56**(3): p. 211-219.
95. Nomura, T., T. Yasuda, and S. Furukawa, *LIQUID SENSOR USING 2-PORT SURFACE ACOUSTIC-WAVE RESONATOR.* Japanese Journal of Applied Physics Part 1-Regular Papers Short Notes & Review Papers, 1992. **31**: p. 78-81.
96. Nomura, T. and T. Yasuda, *SURFACE-ACOUSTIC-WAVE LIQUID SENSORS BASED ON ONE-PORT RESONATOR.* Japanese Journal of Applied Physics Part 1-Regular Papers Short Notes & Review Papers, 1993. **32**(5B): p. 2372-2375.
97. Nguyen, V.H., et al., *Single Interdigital Transducer Approach for Gravimetrical SAW Sensor Applications in Liquid Environments.* Sensors, 2017. **17**(12): p. 13.
98. Hohmann, S., et al., *Surface Acoustic Wave (SAW) Resonators for Monitoring Conditioning Film Formation.* Sensors (Basel), 2015. **15**(5): p. 11873-88.

99. Yantchev, V.M., et al., *Theoretical and Experimental Mass-Sensitivity Analysis of Polymer-Coated SAW and STW Resonators for Gas Sensing Applications.* Ieee Sensors Journal, 2002. **2**(4): p. 307-313.
100. Soluch, W., *Design of SAW delay lines for sensors.* Sensors and Actuators a-Physical, 1998. **67**(1-3): p. 60-64.
101. Vig, J.R. and Y. Kim, *Noise in microelectromechanical system resonators.* Ieee Transactions on Ultrasonics Ferroelectrics and Frequency Control, 1999. **46**(6): p. 1558-1565.
102. *IEEE Standard Definitions of Physical Quantities for Fundamental Frequency and Time Metrology - Random Instabilities.* IEEE Std 1139-1999, 1999: p. 0_1.
103. Rhea, R.W., *Oscillator Design and Computer Simulation*. 1997: McGraw-Hill.
104. Leeson, D.B., *A SIMPLE MODEL OF FEEDBACK OSCILLATOR NOISE SPECTRUM.* Proceedings of the Institute of Electrical and Electronics Engineers, 1966. **54**(2): p. 329-&.
105. Allan, D.W., *STATISTICS OF ATOMIC FREQUENCY STANDARDS.* Proceedings of the Institute of Electrical and Electronics Engineers, 1966. **54**(2): p. 221-&.
106. Howe, D.A., D.U. Allan, and J.A. Barnes. *Properties of Signal Sources and Measurement Methods*. in *Thirty Fifth Annual Frequency Control Symposium*. 1981.
107. Vig, J.R., et al., *A review of sensor sensitivity and stability*, in *Proceedings of the 2000 Ieee/Eia International Frequency Control Symposium & Exhibition*. 2000. p. 30-33.
108. Wohltjen, H., *MECHANISM OF OPERATION AND DESIGN CONSIDERATIONS FOR SURFACE ACOUSTIC-WAVE DEVICE VAPOR SENSORS.* Sensors and Actuators, 1984. **5**(4): p. 307-325.
109. Kuypers, J.H., et al. *Intrinsic temperature compensation of aluminum nitride Lamb wave resonators for multiple-frequency references*. in *2008 IEEE International Frequency Control Symposium*. 2008.
110. Hashimoto, K., et al. *Recent development of temperature compensated SAW Devices*. in *2011 IEEE International Ultrasonics Symposium*. 2011.
111. Mansfeld, F., S. Lin, and H. Shih, *DETECTION AND MONITORING OF LOCALIZED CORROSION OF ALUMINUM-ALLOYS WITH ELECTROCHEMICAL IMPEDANCE SPECTROSCOPY*. New Methods for Corrosion Testing of Aluminum Alloys, ed. V.S. Agarwala and G.M. Ugiansky. Vol. 1134. 1992. 141-152.
112. Roberge, P.R. and V.S. Sastri, *ONLINE CORROSION MONITORING WITH ELECTROCHEMICAL IMPEDANCE SPECTROSCOPY.* Corrosion, 1994. **50**(10): p. 744-754.
113. Niya, S.M.R. and M. Hoorfar, *Study of proton exchange membrane fuel cells using electrochemical impedance spectroscopy technique - A review.* Journal of Power Sources, 2013. **240**: p. 281-293.
114. Cheng, S.A., et al., *Electrochemical impedance spectroscopy study of Ni/MH batteries.* Journal of Alloys and Compounds, 1999. **293**: p. 814-820.
115. Zhu, J.G., et al., *A new lithium-ion battery internal temperature on-line estimate method based on electrochemical impedance spectroscopy measurement.* Journal of Power Sources, 2015. **274**: p. 990-1004.
116. Lisdat, F. and D. Schafer, *The use of electrochemical impedance spectroscopy for biosensing.* Analytical and Bioanalytical Chemistry, 2008. **391**(5): p. 1555-1567.
117. Grieshaber, D., et al., *Electrochemical biosensors - Sensor principles and architectures.* Sensors, 2008. **8**(3): p. 1400-1458.

118. Daza, P., et al., *Monitoring living cell assays with bio-impedance sensors.* Sensors and Actuators B-Chemical, 2013. **176**: p. 605-610.
119. Madou, M.J., *Solid-State Physics, Fluidics, and Analytical Techniques in Micro- and Nanotechnology*. 2011: CRC Press.
120. Lange, K., B.E. Rapp, and M. Rapp, *Surface acoustic wave biosensors: a review.* Analytical and Bioanalytical Chemistry, 2008. **391**(5): p. 1509-1519.
121. Xu, Z. and Y.J. Yuan, *Implementation of guiding layers of surface acoustic wave devices: A review.* Biosensors & Bioelectronics, 2018. **99**: p. 500-512.
122. Kondoh, J., Y. Matsui, and S. Shiokawa, *New Biosensor Using Shear Horizontal Surface-Acoustic-Wave Device.* Japanese Journal of Applied Physics Part 1-Regular Papers Short Notes & Review Papers, 1993. **32**(5b): p. 2376-2379.
123. Hohmann, S., et al., *Surface Acoustic Wave (SAW) Resonators for Monitoring Conditioning Film Formation.* Sensors, 2015. **15**(5): p. 11873-11888.
124. Kustanovich, K., et al., *A high-performance lab-on-a-chip liquid sensor employing surface acoustic wave resonance.* Journal of Micromechanics and Microengineering, 2017. **27**(11): p. 9.
125. Tseng, W.K., et al., *Active micro-mixers using surface acoustic waves on Y-cut 128 degrees LiNbO3.* Journal of Micromechanics and Microengineering, 2006. **16**(3): p. 539-548.
126. Kustanovich, K., et al., *Design and Characterization of Surface Acoustic Wave Resonance (SAR) System for In-liquid Sensing*, in *2017 Joint Conference of the European Frequency and Time Forum and Ieee International Frequency Control Symposium*. 2017. p. 652-655.
127. Wright, P.V., *A REVIEW OF SAW RESONATOR FILTER TECHNOLOGY*, in *Ieee 1992 Ultrasonics Symposium : Proceedings, Vols 1 and 2*, B.R. McAvoy, Editor. 1992. p. 29-38.
128. Abbott, B., K. Kokkonen, and Ieee, *CALCULATING TRANSVERSE MODE PROFILES OF TCSAW PISTON MODE RESONATORS*, in *2016 Ieee International Ultrasonics Symposium*. 2016.
129. Yantchev, V., et al., *Parametric Study of resonant TC-SAW Piston-mode Configurations*, in *2017 Ieee International Ultrasonics Symposium*. 2017.
130. Zhang, B.F., et al., *Impact of Coupling Between Multiple SAW Modes on Piston Mode Operation of SAW Resonators.* Ieee Transactions on Ultrasonics Ferroelectrics and Frequency Control, 2018. **65**(6): p. 1062-1068.
131. Matsuda, S., et al., *Experimental Studies of Quality Factor Deterioration in Shear-Horizontal-Type Surface Acoustic Wave Resonators Caused by Apodization of Interdigital Transducer.* Japanese Journal of Applied Physics, 2011. **50**(7).
132. Gulyaev, Y.V., V.I. Grigorievski, and V.P. Plessky, *Comparative analysis of synchronous "hiccup" and nonsynchronous saw resonators on quartz*. Mep 2006: Proceedings of Multiconference on Electronics and Photonics, ed. I.A. Sukhoivanov, et al. 2006. 83-+.
133. Plessky, V., et al., *Revisiting "Hiccup" SAW Resonators on Strong Piezoelectric Substrates*, in *2018 Ieee International Frequency Control Symposium*. 2018. p. 349-353.
134. Kustanovich, K., et al., *A high-performance lab-on-a-chip liquid sensor employing surface acoustic wave resonance: part II.* Journal of Micromechanics and Microengineering, 2019. **29**(2): p. 8.

135. Morita, T., M. Sugimoto, and J. Kondoh, *Measurements of Standard-Viscosity Liquids Using Shear Horizontal Surface Acoustic Wave Sensors.* Japanese Journal of Applied Physics, 2009. **48**(7).
136. Gil, T., et al., *Theoretical analysis of protein organization in lipid membranes.* Biochimica Et Biophysica Acta-Reviews on Biomembranes, 1998. **1376**(3): p. 245-266.
137. Hunte, C., *Specific protein-lipid interactions in membrane proteins.* Biochemical Society Transactions, 2005. **33**: p. 938-942.
138. Lee, A.G., *Lipid-protein interactions.* Biochemical Society Transactions, 2011. **39**: p. 761-766.
139. Groves, J.T., L.K. Mahal, and C.R. Bertozzi, *Control of cell adhesion and growth with micropatterned supported lipid membranes.* Langmuir, 2001. **17**(17): p. 5129-5133.
140. Marquez, M.G., et al., *Changes in membrane lipid composition cause alterations in epithelial cell-cell adhesion structures in renal papillary collecting duct cells.* Biochimica Et Biophysica Acta-Biomembranes, 2012. **1818**(3): p. 491-501.
141. Marquez, M.G., et al., *Membrane lipid composition plays a central role in the maintenance of epithelial cell adhesion to the extracellular matrix.* Lipids, 2008. **43**(4): p. 343-352.
142. Gozen, I., et al., *Fractal avalanche ruptures in biological membranes.* Nature Materials, 2010. **9**(11): p. 908-912.
143. Sinn, C.G., M. Antonietti, and R. Dimova, *Binding of calcium to phosphatidylcholine-phosphatidylserine membranes.* Colloids and Surfaces a-Physicochemical and Engineering Aspects, 2006. **282**: p. 410-419.
144. Melcrova, A., et al., *The complex nature of calcium cation interactions with phospholipid bilayers.* Scientific Reports, 2016. **6**.
145. Doosti, B.A., et al., *Membrane Tubulation in Lipid Vesicles Triggered by the Local Application of Calcium Ions.* Langmuir, 2017. **33**(41): p. 11010-11017.
146. Ainla, A., et al., *A Microfluidic Diluter Based on Pulse Width Flow Modulation.* Analytical Chemistry, 2009. **81**(13): p. 5549-5556.
147. Gozen, I., et al., *Calcium-ion-controlled nanoparticle-induced tubulation in supported flat phospholipid vesicles.* Soft Matter, 2011. **7**(20): p. 9706-9713.
148. Briand, E., et al., *Combined QCM-D and EIS study of supported lipid bilayer formation and interaction with pore-forming peptides.* Analyst, 2010. **135**(2): p. 343-50.
149. He, H., et al., *A simultaneous electrochemical impedance and quartz crystal microbalance study on antihuman immunoglobulin G adsorption and human immunogloulin G reaction.* Journal of Biochemical and Biophysical Methods, 2005. **62**(3): p. 191-205.
150. Sabot, A. and S. Krause, *Simultaneous quartz crystal microbalance impedance and electrochemical impedance measurements. Investigation into the degradation of thin polymer films.* Analytical Chemistry, 2002. **74**(14): p. 3304-3311.
151. Xie, Q.J., et al., *Simultaneous impedance measurements of two one-face sealed resonating piezoelectric quartz crystals for in situ monitoring of electrochemical processes and solution properties.* Analytica Chimica Acta, 2005. **533**(2): p. 213-224.
152. Liu, F., et al., *A lab-on-chip cell-based biosensor for label-free sensing of water toxicants.* Lab on a Chip, 2014. **14**(7): p. 1270-1280.

153. Rana, S., R.H. Page, and C.J. McNeil, *Impedance spectra analysis to characterize interdigitated electrodes as electrochemical sensors.* Electrochimica Acta, 2011. **56**(24): p. 8559-8563.
154. Valera, E., et al., *Impedimetric immunosensor for atrazine detection using interdigitated mu-electrodes (ID mu E's).* Sensors and Actuators B-Chemical, 2007. **125**(2): p. 526-537.
155. Wang, L., et al., *A sensitive DNA capacitive biosensor using interdigitated electrodes.* Biosensors & Bioelectronics, 2017. **87**: p. 646-653.
156. Zou, Z.W., et al., *Functionalized nano interdigitated electrodes arrays on polymer with integrated microfluidics for direct bio-affinity sensing using impedimetric measurement.* Sensors and Actuators a-Physical, 2007. **136**(2): p. 518-526.
157. Madou, M.J., *Manufacturing Techniques for Microfabrication and Nanotechnology*. 2011: CRC Press.
158. Franssila, S., *Introduction to Microfabrication*. 2010: Wiley.
159. McDonald, J.C. and G.M. Whitesides, *Poly(dimethylsiloxane) as a material for fabricating microfluidic devices.* Accounts of Chemical Research, 2002. **35**(7): p. 491-499.
160. Whitesides, G.M., et al., *Soft lithography in biology and biochemistry.* Annual Review of Biomedical Engineering, 2001. **3**: p. 335-373.
161. Madsen, M.H., et al., *Accounting for PDMS shrinkage when replicating structures.* Journal of Micromechanics and Microengineering, 2014. **24**(12).
162. del Campo, A. and C. Greiner, *SU-8: a photoresist for high-aspect-ratio and 3D submicron lithography.* Journal of Micromechanics and Microengineering, 2007. **17**(6): p. R81-R95.
163. Kovacs, G., et al., *Improved Material Constants for Linbo3 and Litao3.* Ieee 1990 Ultrasonics Symposium : Proceedings, Vols 1-3, 1990: p. 435-438.
164. Ainla, A., et al., *A multifunctional pipette.* Lab on a Chip, 2012. **12**(7): p. 1255-1261.
165. Kim, A.A., et al., *SU-8 free-standing microfluidic probes.* Biomicrofluidics, 2017. **11**(1): p. 014112.
166. Matsuda, S., et al. *Investigation of SiO2film properties for zero temperature coefficient of frequency SAW devices*. in *2010 IEEE International Ultrasonics Symposium*. 2010.

The Selection Committee of the European Frequency and Time Forum
has decree to award

Kiryl Kustanovich

the conference prize for the best student paper in the area: Sensors & Transducers.

The Award is conferred at the plenary session of 32nd European Frequency and Time Forum in Torino, April the 11th 2018.

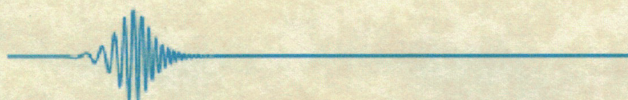

Dr. Filippo Levi
Chair of the Local Organizing Committee